



HAL
open science

Numerical investigations of some mathematical models of the diffusion MRI signal

Hang Tuan Nguyen

► **To cite this version:**

Hang Tuan Nguyen. Numerical investigations of some mathematical models of the diffusion MRI signal. Other [cond-mat.other]. Université Paris Sud - Paris XI, 2014. English. NNT : 2014PA112016 . tel-01124248

HAL Id: tel-01124248

<https://theses.hal.science/tel-01124248>

Submitted on 6 Mar 2015

HAL is a multi-disciplinary open access archive for the deposit and dissemination of scientific research documents, whether they are published or not. The documents may come from teaching and research institutions in France or abroad, or from public or private research centers.

L'archive ouverte pluridisciplinaire **HAL**, est destinée au dépôt et à la diffusion de documents scientifiques de niveau recherche, publiés ou non, émanant des établissements d'enseignement et de recherche français ou étrangers, des laboratoires publics ou privés.



UNIVERSITÉ PARIS-SUD

ECOLE DOCTORALE: STITS
LABORATOIRE: NEUROSPIN - CEA SACLAY

DISCIPLINE: PHYSIQUE

THÈSE DE DOCTORAT

Soutenu le 29 janvier 2014 par

Hang Tuan NGUYEN

**Numerical investigations of some
mathematical models of the diffusion
MRI signal**

Directeur de thèse : M. Cyril POUPON
Co-directeurs de thèse : Mme. Jing-Rebecca LI
M. Denis S. GREBENKOV

Composition du jury :

Rapporteurs : M. Valerij G. KISELEV
M. Antoine LEJAY
Examineurs : M. Rachid DERICHE
M. Ludovic DE ROCHEFORT

Acknowledgment

First, I would like to deeply thank Dr. Jing-Rebecca Li and Prof. Denis S. Grebenkov, for their offering of my PhD position and beyond, for their kindheartedly advising: thank you for all of your help, your patience and instructions. It was really lucky for me to work with you.

I would like to especially thank Dr. Cyril Poupon, my PhD director, for all of his generous support during my PhD time: thank you very much. I also really appreciate Dr. Denis Le Bihan, director of Neurospin, for his kindly instructions and equipment supports.

I am very grateful to Dr. Haddar Housseem, for his support during the time I have worked at CMAP. I would like to thank Prof. Jean-Christophe Ginefri for his guiding from STITS.

I would like to thank Prof. Valerij G. Kiselev and Dr. Antoine Lejay, for reviewing and correcting my thesis, even in Christmas holiday. I am also grateful to Dr. Rachid Deriche and Dr. Ludovic De Rochefort for examining my thesis. Thank you so much for joining the Jury of my defense!

I also appreciate Mrs. Elisabeth, Mrs. Wallis, Mrs. Berthou, Ms. Gameiro, ... for their help.

A huge thank to my colleague Dang Van Nguyen, for his kindly help and instructions: thanks a lot. Many thanks to Veronique and Benoît for all of your help from beginning. My special thanks to Gabrielle, Simona and Shunrou.

A lot of thanks to all of my friends living in Vietnam and France for their supports and sharing in my daily life. I wish you all the best!

Finally, I would like to say 'thank you' to my parents who always wish me complete a PhD, to my brother and sister who help me whenever I need them, to my wife for everything we have together in many years, to her parents for sympathetic supports. Many respectful thanks to my grandparents, my uncles and aunts, ..., and all of my family.

Contents

1	Diffusion magnetic resonance imaging in biological tissues	9
1.1	Motivation	9
1.2	Equations of MRI	10
1.3	Equations of dMRI	11
1.3.1	Diffusion-encoding sequences	11
1.3.2	Derivation of b-value	13
1.4	Simple Gaussian signal model not adequate	15
1.5	Theoretical approaches in dMRI	16
1.6	Numerical methods	18
1.7	Moments of the dMRI signal	18
1.8	Biological tissue dMRI	19
2	Voxel-level signal models accounting for heterogeneous domains	21
2.1	Diffusion models for brain tissue	21
2.2	Some mathematical models	22
2.3	The voxel	24
2.3.1	Periodic extension of the voxel	24
2.3.2	(Periodic) representative volume of the voxel	24
2.4	Microscopic multiple compartments Bloch-Torrey PDE	25
2.5	Compartment magnetizations	26
2.6	Kärger model	27
2.7	Macroscopic ODE model	28
2.8	Limiting cases	33
3	Numerical study of two macroscopic dMRI signal models	35
3.1	Method	35
3.2	Numerical study	36
3.2.1	Periodic lattice of spheres	37
3.2.1.1	Residence time	37
3.2.1.2	Compartment magnetization	38
3.2.1.3	Diffusion time	42

3.2.1.4	Membrane permeability	43
3.2.1.5	Cell size	44
3.2.2	Simulation on complex geometries	45
3.2.2.1	Domain containing spheres of various sizes	45
3.2.2.2	Domain containing parallel cylinders	46
3.2.2.3	Domain containing cylinders with thick membrane layer	48
3.2.2.4	Domain containing cylinders of different orientations and spheres	49
3.3	Discussion	51
3.4	Conclusions	51
4	Parameters estimation using macroscopic dMRI signal models	53
4.1	The least squares problem	55
4.2	Domain containing periodic lattice of spheres of the same size	57
4.2.1	Least squares problem on a 3-parameters set	57
4.2.2	Contour plots of 2-parameters sets	58
4.2.3	Effect of permeability	60
4.2.4	Effect of diffusion time	62
4.2.5	Effects of b -values	65
4.2.6	Effects of cell size	69
4.3	Periodic lattice of spherical cells of different sizes	73
4.3.1	Least squares problem on 3-parameters set	73
4.3.2	Contour plots of 2-parameters sets	75
4.3.3	Effect of noisy signal	76
4.4	Domain containing parallel cylinders with thick membrane layer	79
4.4.1	Least squares problem on 4-parameters set	79
4.4.2	Contour plots on 2-parameters sets	80
4.5	Domain containing slanted parallel cylinders	82
4.6	Domain containing spheres and deformed cylinders	86
4.7	Conclusions and further improvements	89
	Bibliography	105

Summary

Diffusion magnetic resonance imaging (dMRI) has been used widely in biological and medical applications to detect a large range of physiological and pathological conditions. The image contrast in dMRI of biological tissues comes from the differing water diffusion characteristics in the imaged tissue at different spatial positions. The resolution of dMRI is on the order of a millimeter, meaning the dMRI signal provides averaged information on a volume, called a voxel, whose size is much larger than cell features, that vary, for example in brain, on the scale of a micrometer.

To understand the relationship between the tissue microstructure inside a voxel and the dMRI signal, macroscopic models of the dMRI signal have been formulated to relate the signal to model parameters that represent averaged quantities over the voxel. In this thesis, we investigated two such macroscopic models. The first is the Kärger model that assumes a certain form of (macroscopic) multiple compartmental diffusion and inter-compartment exchange, but is subject to the narrow pulse restriction on the diffusion-encoding magnetic field gradient pulses. The second is an ODE model of the multiple compartment magnetizations obtained from mathematical homogenization of the Bloch-Torrey equation, that is not subject to the narrow pulse restriction.

First, we investigated the validity of the two aforementioned macroscopic models by comparing the dMRI signal given by the Kärger and the ODE models with the dMRI signal simulated on some relatively complex tissue geometries by solving the microscopic Bloch-Torrey equation in the presence of permeable biological cell membranes. We note that the Kärger model is a limit case of the ODE model where the duration of the diffusion-encoding magnetic field gradient pulses goes to zero. We concluded that the validity of both macroscopic models is limited to the case where diffusion in each compartment is effectively Gaussian and where the inter-compartmental exchange can be accounted for by standard linear kinetic terms.

Next, assuming that the above conditions on the compartmental diffusion and inter-compartment exchange are satisfied, we solve the least squares problem associated with fitting the Kärger and the ODE model parameters to the simulated dMRI signal obtained by solving the microscopic Bloch-Torrey equation. Among various effective parameters, we considered the volume fractions of the intra-cellular and extra-cellular compartments (which may change during cell swelling), membrane permeability (which may characterize, to some extent, normal or abnormal functioning of cells), average size of cells, inter-cellular distance, as well as apparent diffusion coefficients. We started by studying the feasibility of the least squares solution for two groups of relatively simple tissue geometries. For the first group, in which domains consist of variably sized spherical cells embedded in the extra-cellular space, we concluded that parameters estimation problem can be robustly solved, even in the presence of noise. In the second group, we considered parallel cylindrical cells, which may be covered by a thick membrane layer, and embedded

in the extra-cellular space. When the diffusion gradient is applied perpendicularly to the cylinder axis, the parameter estimation problem can be robustly solved, just as for spherical cells. In the opposite case of the diffusion gradient parallel to the axis cylinder, one simply probes unrestricted diffusion which contains no information about the restricting domain and water exchange between compartments. As a consequence, the parameter estimation fails in this situation. For an intermediate gradient direction, the quality of parameter estimation strongly depends on how much the cellular structure is elongated in the gradient direction. In practice, the orientation of elongated cells is not known a priori; moreover, biological tissues may contain elongated structures randomly oriented and also mixed with other (compact) elements (e.g., axons and glial cells). This situation has been numerically investigated on our most complicated domain in which layers of cylindrical cells in various directions are mixed with layers of spherical cells. We checked that certain parameters can still be estimated rather accurately while the other remain inaccessible. In future works, the quality of the estimation may be improved by acquiring signals in various directions and then fitting all these signals to the appropriate ODE models. In all considered cases, the ODE model provided more accurate estimates than the Kärger model.

Diffusion magnetic resonance imaging in biological tissues

1.1 Motivation

Diffusion magnetic resonance imaging (dMRI) is a widespread experimental technique in which the random trajectories of diffusing nuclei are encoded by magnetic field gradient pulses [1–3]. When the nuclei diffuse inside a heterogeneous medium, the statistics of the random trajectories is affected by the presence of (possibly semi-permeable) walls or obstacles. Although these microscopic hindrances are not visible at the spatial resolution of dMRI, all these geometrical features are statistically aggregated into the macroscopic dMRI signal. Measuring the signal at different diffusion times, gradient intensities and directions, one aims to infer the morphological structure of a sample and to characterize the dynamics of a system. This is a formidable inverse problem which until now has no complete solution [3].

In spite of this fundamental gap, the non-invasive character of dMRI made this technique a gold standard in material sciences, neurosciences and medicine, with numerous applications to mineral samples (e.g., sedimentary rocks in oil industry, concrete, cements and gypsum in building industry) and biological samples (e.g., brain, lungs, bones). For instance, diffusion-weighted brain imaging is daily performed in research and clinical MR scanners, both for detecting pathological regions and monitoring functional properties of the brain [4–12].

The image contrast in dMRI of biological tissues comes from the differing water diffusion characteristics in the imaged tissue at different spatial positions. The resolution of dMRI is on the order of a millimeter, meaning the dMRI signal provides averaged information on a volume, called a voxel, whose size is much larger than cell features, that vary, for example in brain, on the scale of a micrometer.

An important medical application of dMRI is the detection of cerebral ischemia (cell swelling in the brain) a few minutes after stroke [13, 14]. In the brain, dMRI has been used to detect a wide range of physiological and pathological conditions, including tumors [15–18], myelination abnormalities [19], connectivity [20], as well as in functional imaging where recent work has suggested that water dMRI could also be used to visualize changes in tissue microstructure that might arise during neuronal activation [21]. Based on the known sensitivity of dMRI to cell size in tissues [22, 23] and on optical imaging studies that have revealed changes in the shape (in particular swelling) of neurons and glial cells during brain activation

[12, 24], the observed findings have been tentatively ascribed to a transient swelling of cortical cells. For a recent survey, see [6].

1.2 Equations of MRI

The principle of spatial encoding in (water proton) magnetic resonance imaging (MRI) is the following. Suppose r_1, r_2, r_3 are the axes of a 3D coordinate system. Water protons have a property called spin, and under the influence of an applied magnetic field in the r_3 -direction, will precess about the r_3 -axis at a frequency that is proportional to the strength of the applied magnetic field. The constant of proportionality is called the gyromagnetic ratio and it is $\gamma = 2.675 \cdot 10^8$ rad/s/Tesla for the water proton. When the applied magnetic field varies linearly in space, it is called a magnetic field *gradient*. If we denote the direction and amplitude of the gradient by $\mathbf{q} = (q_1, q_2, q_3)$ and its time profile by $h(t)$, then the complex transverse magnetization on the $r_1 - r_2$ plane, $M(\mathbf{r}, t) := M_{r_1}(\mathbf{r}, t) + iM_{r_2}(\mathbf{r}, t)$, i is the imaginary unit, obeys the Bloch Equation [25]:

$$\frac{\partial M(\mathbf{r}, t)}{\partial t} = -i\gamma \mathbf{r} \cdot \mathbf{q} h(t)M(\mathbf{r}, t) - \frac{M(\mathbf{r}, t)}{T_2(\mathbf{r})},$$

in the rotating frame at the Larmor frequency, where $T_2(\mathbf{r})$ is the local spin-spin relaxation rate. The solution of the above equation is:

$$M(\mathbf{r}, t) = \rho(\mathbf{r}) e^{-t/T_2(\mathbf{r})} e^{-i\mathbf{r} \cdot \left(\gamma \mathbf{q} \int_0^t h(s) ds \right)},$$

where $\rho(\mathbf{r})$ is the spin density.

Even though 3D imaging is possible, most often the MRI signal is acquired in 2D, slice by slice. Suppose $r_3 \in [(l - \frac{1}{2})\Delta r_3, (l + \frac{1}{2})\Delta r_3]$ are the limits of the slice of interest, then the MRI signal acquired is the integral of the magnetization in that slice:

$$\hat{\mu}_l \left(\gamma (q_1, q_2) \int_0^t h(s) ds \right) = \int_{r_1, r_2} \mu_l(r_1, r_2) e^{-i(r_1, r_2) \cdot \left(\gamma (q_1, q_2) \int_0^t h(s) ds \right)} dr_1 dr_2, \quad (1.1)$$

where

$$\mu_l(r_1, r_2) = \left(\int_{(l-\frac{1}{2})\Delta r_3}^{(l+\frac{1}{2})\Delta r_3} \rho(r_1, r_2, r_3) e^{-t/T_2(r_1, r_2, r_3)} dr_3 \right). \quad (1.2)$$

For simplicity we have chosen $q_3 = 0$. It is clear from Eq. (1.1) that the MRI signal is a 2D Fourier transform of $\mu_l(r_1, r_2)$. By choosing the appropriate set of q_1, q_2 and $h(s)$ (not discussed here), the Fourier transform can be acquired at a set of 2D Fourier points. Then the inverse Fourier transform can be performed and sampled at physical space points to obtain in each voxel $V_{i,j,l}$ an average value of $\mu_l(r_1, r_2)$:

$$\bar{\mu}_l(i, j) \approx \frac{1}{\Delta r_1 \Delta r_2} \int_{V_{i,j,l}} \mu_l(r_1, r_2) dr_1 dr_2,$$

1.3. Equations of dMRI

that gives the contrast in a MRI image in slice l , where

$$V_{i,j,l} := \left[\left(i - \frac{1}{2} \right) \Delta r_1, \left(i + \frac{1}{2} \right) \Delta r_1 \right] \times \left[\left(j - \frac{1}{2} \right) \Delta r_2, \left(j + \frac{1}{2} \right) \Delta r_2 \right] \times \left[\left(l - \frac{1}{2} \right) \Delta r_3, \left(l + \frac{1}{2} \right) \Delta r_3 \right].$$

In Eq. (1.2) we can see two widely used contrast mechanisms in MRI, the proton density and the T_2 relaxation.

1.3 Equations of dMRI

Now, in addition to the imaging gradient \mathbf{q} and its time profile $h(t)$ described above, another set of magnetic field gradients can be applied to encode the random displacement of water molecules. Combining a series of gradient pulses, one can investigate the self-diffusion properties of the sample even for a uniform initial distribution. This is the basis of the imaging modality called *diffusion MRI*.

In detail, we denote the “diffusion-encoding” gradient by $\mathbf{g} = (g_1, g_2, g_3)$ and its time profile $f(t)$. Then we get the Bloch-Torrey equation [26]:

$$\frac{\partial M(\mathbf{r}, t)}{\partial t} = -i\gamma \mathbf{r} \cdot \mathbf{q} h(t) M(\mathbf{r}, t) - \frac{M(\mathbf{r}, t)}{T_2(\mathbf{r})} - i\gamma \mathbf{r} \cdot \mathbf{g} f(t) M(\mathbf{r}, t) + \nabla \cdot (D(\mathbf{r}) \nabla M(\mathbf{r}, t)),$$

where we included the effects of both the imaging gradient \mathbf{q} and the diffusion gradient \mathbf{g} . The last term in the above equation describes diffusion (random movement) of water molecules.

1.3.1 Diffusion-encoding sequences

The diffusion-encoding happens via the application of a series of magnetic field gradient “pulses”. The term “pulse” means that the magnetic field gradient is turned on only for a short duration. For example, the standard Pulsed-Gradient Spin Echo (PGSE) [27] sequence is made of two rectangular pulses of duration δ , separated by a time interval $\Delta - \delta$, and the associated profile $f(t)$ is:

$$f(t) = \begin{cases} 1, & t_0 \leq t \leq t_0 + \delta, \\ -1, & t_0 + \Delta < t \leq t_0 + \Delta + \delta, \\ 0, & \text{elsewhere,} \end{cases} \quad (1.3)$$

where t_0 is the start of the first pulse with $t_0 + \Delta > TE/2$, TE is the echo time when the signal is measured. See Fig. 1.1. Note that the opposite sign of the second gradient pulse effectively accounts for the intermediate 180° rf pulse [1, 2].

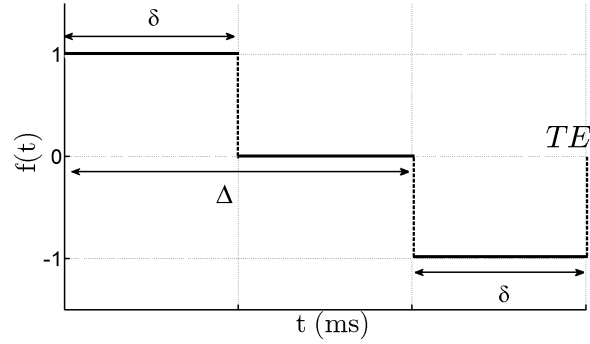


Figure 1.1: PGSE rectangle shaped profile, with $t_0 = 0$.

If the rise time of the pulse is not instantaneous then $f(t)$ has a trapezoidal profile:

$$f(t) = \begin{cases} \frac{t-t_0}{\tau}, & t_0 \leq t \leq t_0 + \tau, \\ 1, & t_0 + \tau < t \leq t_0 + \delta - \tau, \\ -\frac{t-t_0-\delta}{\tau}, & t_0 + \delta - \tau < t \leq t_0 + \delta, \\ -\frac{t-t_0-\Delta}{\tau}, & t_0 + \Delta < t \leq t_0 + \Delta + \tau, \\ -1, & t_0 + \Delta + \tau < t \leq t_0 + \Delta + \delta - \tau, \\ \frac{t-t_0-(\Delta+\delta)}{\tau}, & t_0 + \Delta + \delta - \tau < t \leq t_0 + \Delta + \delta, \\ 0, & \text{otherwise,} \end{cases} \quad (1.4)$$

where the rise time is τ . See Fig. 1.2.

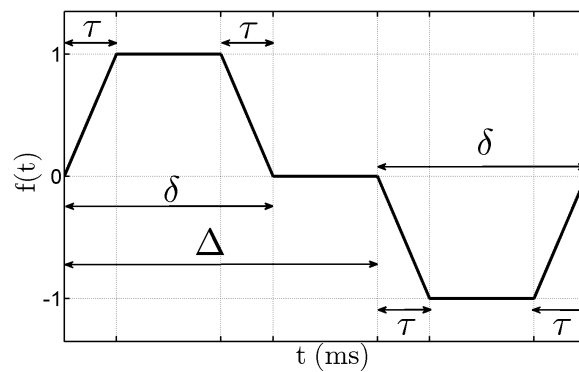


Figure 1.2: PGSE trapezoidal shaped profile, with $t_0 = 0$.

The oscillating gradient spin echo [28] (OGSE) sine sequence consists of two oscillating sine pulses of duration σ , each containing n periods (hence the frequency is

1.3. Equations of dMRI

$\omega = n \frac{2\pi}{\sigma}$), separated by a time interval $\tau - \sigma$, and the associated profile $f(t)$ is:

$$f(t) = \begin{cases} \sin(\omega(t - t_0)), & t_0 < t \leq t_0 + \sigma, \\ -\sin(\omega(t - t_0 - \tau)), & \tau + t_0 < t \leq t_0 + \tau + \sigma, \\ 0, & \text{otherwise,} \end{cases} \quad (1.5)$$

where $\tau = TE/2$. See Fig. 1.3 for an example with $n = 2$.

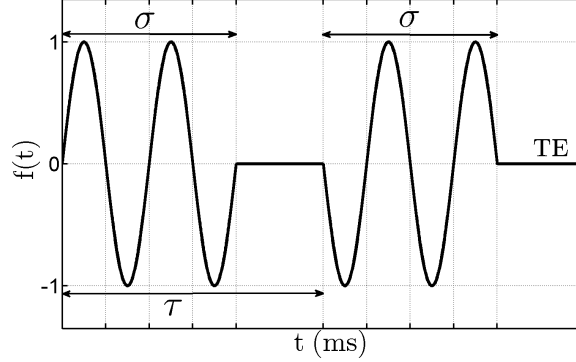


Figure 1.3: OGSE sine profile, each pulse contains 2 periods, with $t_0 = 0$.

1.3.2 Derivation of b-value

Under the assumption that water molecules experience a homogeneous (or homogenized) isotropic diffusion environment characterized by the diffusion coefficient D^{hom} inside the voxel $V_{i,j,l}$, the water molecules at position $\mathbf{r}_0 \in V_{i,j,l}$ at t_0 diffuse according to the probability density function:

$$P(\mathbf{r}, t) = \frac{\exp(-\frac{\|\mathbf{r}-\mathbf{r}_0\|^2}{4D^{hom}(t-t_0)})}{(4\pi D^{hom}(t-t_0))^{\frac{d}{2}}}, \quad d = 3,$$

where the support of $P(\mathbf{r}, t)$ is much smaller than $V_{i,j,l}$ because the diffusion distance in a dMRI experiment is much smaller than the size of a voxel. (We have neglected those \mathbf{r}_0 that are close to the boundary of $V_{i,j,l}$.)

Furthermore, under the assumption that $\delta \ll \Delta$ (the narrow pulse approximation), the influence of the diffusion-encoding magnetic field gradient pulse on the complex transverse magnetization due to water molecules starting at \mathbf{r}_0 at t_0 can be described by a gain of the complex phase $e^{-i\gamma \mathbf{g} \cdot \mathbf{r}_0 \delta}$ between t_0 and $t_0 + \delta$. Then, the magnetization due to water molecules at position \mathbf{r} at $t_0 + \Delta$ gains a complex phase $e^{i\gamma \mathbf{g} \cdot \mathbf{r} \delta}$ between $t_0 + \Delta$ and $t_0 + \Delta + \delta$. Thus, the effect on the dMRI signal, compared to having no diffusion gradient \mathbf{g} , is an *attenuation* (loss) of the signal:

$$\int_{\mathbf{r} \in V_{i,j,l}} \frac{\exp(-\frac{\|\mathbf{r}-\mathbf{r}_0\|^2}{4D^{hom}\Delta})}{(4\pi D^{hom}\Delta)^{\frac{d}{2}}} e^{i\gamma \mathbf{g} \cdot (\mathbf{r}-\mathbf{r}_0) \delta} = \exp(-\gamma^2 \delta^2 \|\mathbf{g}\|^2 D^{hom} \Delta),$$

Chapter 1. Diffusion magnetic resonance imaging in biological tissues

where the integration domain $V_{i,j,l}$ was extended to the whole space \mathbb{R}^3 .

If δ is not small compared to Δ , then in fact, the signal attenuation in the voxel $V_{i,j,l}$ still can be expressed in mono-exponential form [26]:

$$S(b, TE) = e^{-D^{hom} b},$$

where the b -value is a weighting factor as defined in [29] and it is

$$b(\mathbf{g}, \delta, \Delta) = \gamma^2 \|\mathbf{g}\|^2 \delta^2 (\Delta - \delta/3), \quad (1.6)$$

for the PGSE sequence. The replacement of Δ by $\Delta - \delta/3$ accounts for pulses that are not narrow.

Including the effect of the diffusion-encoding gradient means that the image contrast function in Eq. (1.2) becomes:

$$\mu_l(r_1, r_2) = \left(\int_{(l-\frac{1}{2})\Delta r_3}^{(l+\frac{1}{2})\Delta r_3} \rho(r_1, r_2, r_3) e^{-t/T_2(r_1, r_2, r_3)} e^{-D^{hom}(r_1, r_2, r_3) b} dr_3 \right). \quad (1.7)$$

The basis of diffusion weighted imaging is that the MRI signal is acquired with a diffusion gradient \mathbf{g} as well as with no diffusion gradient. The first image (after inverse Fourier transform) is divided by the second image and the log of the ratio is divided by b get an estimate of $D^{hom}(r_1, r_2, r_3)$ in each voxel. This estimated value is called the ‘‘Apparent Diffusion Coefficient’’ (ADC), and serves as the contrast mechanism.

For simplicity, in the rest of the thesis, the effect of T_2 relaxation will be neglected. To focus on understanding the image contrast function in the physical domain, the imaging gradients in Bloch-Torrey equation will also be neglected. Hence, for the remainder of the thesis, we focus on the following simplified form of the Bloch-Torrey equation:

$$\frac{\partial M(\mathbf{r}, t)}{\partial t} = -i\gamma \mathbf{r} \cdot \mathbf{g} f(t) M(\mathbf{r}, t) + \nabla \cdot (D(\mathbf{r}) \nabla M(\mathbf{r}, t)). \quad (1.8)$$

The b -value for a general pulse sequence $f(t)$ can be obtained by solving Eq. (1.8) on a homogeneous domain and expressing its signal under mono-exponential form.

In [30], V.M. Kenkre et al. used the Fourier transform of M ,

$$\hat{M}(k, t) = \int_{-\infty}^{\infty} M(x, t) \exp(-i k x) dx,$$

to obtain the signal in \mathbb{R} :

$$S(t) = \hat{M}\left(\gamma g \int_0^t f(s) ds, 0\right) \exp\left(-D\gamma^2 g^2 \int_0^t du \left(\int_u^t f(s) ds\right)^2\right). \quad (1.9)$$

At the echo time TE , for any standard diffusion sequence, the rephasing condition holds

$$\int_0^{TE} f(t) dt = 0, \quad (1.10)$$

1.4. Simple Gaussian signal model not adequate

so the pre-exponential factor in Eq. (1.9) becomes 1. The b -value is then

$$b(\mathbf{g}) = \gamma^2 g^2 \int_0^{TE} du \left(\int_u^{TE} f(s) ds \right)^2. \quad (1.11)$$

To use the solution in Eq. (1.9) there are certain limitations on the initial spin density, namely, its Fourier transform must exist.

The solution of Eq. (1.8) for uniform initial spin density can be found by the method of separation of variables [31]. Supposing that the solution M can be written in separable form:

$$M(x, t) = S(t) \exp(i\varphi(x, t)),$$

where the spin phase $\varphi(x, t)$ defined by:

$$\varphi(x, t) = \gamma g \cdot x \int_0^t f(s) ds, \quad (1.12)$$

we can obtain the signal at any time $t > 0$:

$$S(t) = S(0) \exp \left(-D\gamma^2 g^2 \int_0^t du \left(\int_0^u f(s) ds \right)^2 \right), \quad (1.13)$$

where at the echo time TE , the b -value can be obtained:

$$b(\mathbf{g}) = \gamma^2 g^2 \int_0^{TE} du \left(\int_0^u f(s) ds \right)^2. \quad (1.14)$$

We emphasize that although the formulas (1.11) and (1.14) are different, they coincide at the echo time TE where the rephasing condition (1.10) holds.

In the rest of the thesis, we will assume uniform initial spin density in each diffusion compartment and use the expression (1.14) for the b -value. In particular, for the trapezoidal PGSE [3]:

$$b(\mathbf{g}, \delta, \Delta) = \gamma^2 \|\mathbf{g}\|^2 \left[(\delta - \tau)^2 \left(\Delta - \frac{\delta - r}{3} \right) + \tau^2 \left(\frac{\tau}{5} - \frac{\delta}{6} \right) \right]. \quad (1.15)$$

One can see that when the rise time τ becomes 0, the above expression reduces to Eq. (1.6) of rectangular PGSE. For the sine OGSE in Eq. (1.5) with an *integer* number of periods n in each of the two durations σ , the corresponding b -value is:

$$b(\mathbf{g}) = \gamma^2 \|\mathbf{g}\|^2 \frac{3\sigma^3}{4n^2\pi^2} = \gamma^2 \|\mathbf{g}\|^2 \frac{3\sigma}{\omega^2}. \quad (1.16)$$

1.4 Simple Gaussian signal model not adequate

There is ample experimental evidence that diffusion in brain tissue at diffusion times relevant to dMRI is not Gaussian: the signal attenuation is not a simple decaying

exponential in b and the slope of $\log S(b)$ at $b = 0$ is not simply related to the intrinsic diffusion coefficients of the physical compartments. The reason for this is that in biological tissue, the diffusion environment seen by water molecules during the time period of Δ (tens of milliseconds) is not homogeneous due to the presence of cells membranes and other heterogeneities. The dMRI signal has been fitted as multiple compartmental Gaussian [32–35], or by including a kurtosis term to quantify the non-Gaussianness [36, 37], or by fitting with fractional order diffusion [38]. Although these phenomenological formulas may accurately fit experimental data, their reliable interpretation requires further investigation based on theoretical tools, numerical simulations, and tissue models.

1.5 Theoretical approaches in dMRI

In spite of significant efforts, theoretical understanding of diffusion MRI is still far from complete. In what follows, we list a number of theoretical approaches developed for dMRI (see [3] for details).

1. The first theoretical analysis of the dMRI signal for diffusion between parallel planes (a plate) goes back to Robertson who used the Laplacian eigenfunctions (for this shape, sines and cosines) to get an explicit *Gaussian phase approximation* (GPA) for the signal [39]. It is equivalent to keeping the second cumulant moment and neglecting the higher-order cumulant moments so that the signal still exhibits the classical Gaussian dependence on the gradient, while the dependence on pulse duration and diffusion time through the second cumulant becomes more intricate. Neuman has extended this analysis to cylinder and sphere [40]. Later on, the Gaussian phase approximation has been extensively used for the analysis of dMRI signals in a variety of structures (see [3]). In particular, the notion of an ADC relies, fundamentally, on this approximation.
2. Tanner and Stejskal computed the dMRI signal in the simple structures in the *narrow pulse approximation* (NPA) [41]. More generally, when the duration of gradient pulses is infinitely short, the dMRI signal can be expressed as the Fourier transform of the averaged diffusion propagator, from which some properties of the geometrical structure can be inferred [1, 2]. The accuracy of both approximations have been checked by numerical simulations [42–45].
3. Kärger introduced a model with two distinct pools of water molecules that co-exist and both occupy the whole volume of a voxel, while the exchange between pools was assumed to be uncorrelated from diffusion and to follow the standard linear kinetics [46, 47]. This Kärger model has become one of the major theoretical approximations to account for water exchange in the dMRI (see below).
4. Mitra *et al.* investigated the short-time behavior of the dMRI signal and showed the possibility to extract the surface-to-volume ratio, as well as per-

1.5. Theoretical approaches in dMRI

meability or surface relaxivity of general porous media [48–51]. In particular, Latour *et al.* measured the time-dependent diffusion coefficient in packed erythrocytes to estimate the erythrocyte membrane permeability and the surface-to-volume ratio of the cells [52]. In the opposite long-time limit, the time-dependent diffusion coefficient allowed one to determine the tortuosity of the medium [53].

5. Callaghan and co-workers introduced the notion of diffusion diffraction that can be used to determine the characteristic length scales of a medium according to positions of diffraction peaks [54].
6. Stoller *et al.* analyzed the behavior of the dMRI at large gradients and described the so-called localization regime [55]. This theoretical analysis has been further developed in [3, 56, 57] and experimentally confirmed in [58].
7. Barzykin *et al.* considered an exchange through the spherical boundary with the extra-cellular space [59, 60].
8. The Robertson’s idea of representing the dMRI signal onto the basis of Laplacian eigenfunctions has led to development of matrix formalisms [3, 57, 61–66]. First proposed by Caprihan *et al.* in [61] and one year later reformulated by Callaghan in a matrix form, this approach has become a power theoretical and numerical tool for the analysis of dMRI signals (see the review and pedagogical introduction in [3, 65, 66]). The explicit form of the Laplacian eigenfunctions in simple structures makes the computation of the dMRI signal very accurate and fast. The method is applicable to any diffusion-encoding sequences (temporal profile) and arbitrary bounded domain. In spite of this generality, matrix formalisms are most efficient for simple shapes (which include, e.g., a class of multilayered structures [67]).
9. Cumulant expansion and kurtosis imaging modality has been actively developed [3, 37, 68, 69].
10. More recently, Novikov and Kiselev proposed an effective medium theory in which spatial variations of the diffusion coefficient were related to correlation functions of heterogeneities of a medium [70].
11. Novikov *et al.* studied the effect of spatial configurations of permeable membranes onto the time-dependent diffusion coefficient [71] (see also [72]). The use of a scattering approach and of the renormalization group solution allowed to relate the long-time scaling behavior of the time-dependent diffusion coefficient to the strong structural fluctuations introduced by permeable membranes.

Some of these general approaches, as well as more specific models relevant to the brain dMRI, will be discussed below.

1.6 Numerical methods

In order to verify the above theoretical approaches or to compute the dMRI signal in complicated structures, one needs to resort to numerical simulations. Roughly speaking, numerical methods can be split into two groups:

1. **Monte Carlo simulations.** A probabilistic interpretation of diffusion equations is employed to represent the original continuous problem as the expectation of a functional of an appropriate stochastic process. Many random trajectories of this process are then generated and used to approximate the expectation and thus the solution. Since there is no discretization, neither of the domain, nor of boundary conditions, Monte Carlo techniques are flexible and easy to implement, especially for studying diffusion in complex geometries. These methods have also been often used in dMRI (e.g., Refs [42, 44, 45, 73–79]).
2. **Finite differences, finite elements, boundary elements, etc.** A domain and/or its boundary are discretized with a regular or adaptive mesh. The original continuous problem (partial differential equation) is then replaced by a set of linear equations to be solved numerically. The solution is obtained at all mesh nodes at successive time moments. Since the accuracy and efficiency of these deterministic numerical schemes significantly rely on the discretization, mesh construction turns out to be the key issue and often a limiting factor, especially in three dimensions. These methods have been frequently applied for computing dMRI signals, e.g., [43, 80–84].

1.7 Moments of the dMRI signal

Theoretical analysis of the dMRI signal as a function of the b -value is difficult. In the narrow pulse (NP) limit, $\delta \ll \Delta$, the following relationship between the moments of the signal and the diffusion propagator can be derived.

Let $P(\mathbf{r}, t | \mathbf{r}_0)$ be the probability of finding water molecules originally at \mathbf{r}_0 ($t = 0$) in position \mathbf{r} at time t , then the signal in the NP limit is:

$$S^{NP}(\|\mathbf{g}\|\delta\gamma, \Delta) = \int_{\mathbf{r}_0 \in \mathbb{R}^3} \rho(\mathbf{r}_0) \int_{\mathbf{r} \in \mathbb{R}^3} e^{-i\|\mathbf{g}\|\delta\gamma(\mathbf{r}-\mathbf{r}_0) \cdot \mathbf{u}_g} P(\mathbf{r}, \Delta | \mathbf{r}_0) d\mathbf{r} d\mathbf{r}_0, \quad (1.17)$$

where $\mathbf{u}_g := \mathbf{g}/\|\mathbf{g}\|$ is the normalized gradient direction, and $\rho(\mathbf{r}_0)$ is the initial density. We chose the independent variable in S^{NP} to be $\|\mathbf{g}\|\delta\gamma$ because the interior integral over \mathbf{r}_0 and \mathbf{r} in Eq. (1.17) can be seen as a one-dimensional Fourier transform, with the Fourier variable being $\|\mathbf{g}\|\delta\gamma$ and the spatial variable being $(\mathbf{r} - \mathbf{r}_0) \cdot \mathbf{u}_g$:

$$S^{NP}(\|\mathbf{g}\|\delta\gamma, \Delta) = \int_{\mathbb{R}} dk e^{-ik(\|\mathbf{g}\|\delta\gamma)} \left[\int_{\mathbf{r}_0 \in \mathbb{R}^3} \rho(\mathbf{r}_0) \int_{\mathbf{r} \in \mathbb{R}^3} \tilde{\delta}(k - (\mathbf{r} - \mathbf{r}_0) \cdot \mathbf{u}_g) P(\mathbf{r}, \Delta | \mathbf{r}_0) d\mathbf{r} d\mathbf{r}_0 \right],$$

1.8. Biological tissue dMRI

where $\tilde{\delta}(x)$ is the Dirac distribution. This allows one to relate derivatives of the Fourier transform and the moments of the original function:

$$i^{2n} \frac{d^{2n} S^{NP}}{d(\|\mathbf{g}\|\delta\gamma)^{2n}}(\|\mathbf{g}\|\delta\gamma, \Delta) = \int_{\mathbf{r}_0 \in \mathbb{R}^3} \rho(\mathbf{r}_0) \int_{\mathbf{r} \in \mathbb{R}^3} e^{-i\mathbf{g}\delta\gamma(\mathbf{r}-\mathbf{r}_0)} ((\mathbf{r} - \mathbf{r}_0) \cdot \mathbf{u}_{\mathbf{g}})^{2n} P(\mathbf{r}, \Delta|\mathbf{r}_0) d\mathbf{r} d\mathbf{r}_0.$$

In a dMRI experiment, the pulse sequence profile $f(t)$ is most often fixed while \mathbf{g} is varied in amplitude, so we can treat Δ as a constant and use the new independent variable $b = \gamma^2 \|\mathbf{g}\|^2 \delta^2 \Delta$ to obtain:

$$\frac{d^n S^{NP}}{d b^n}(0, \Delta) = \frac{(-1)^n n!}{(2n)!} \frac{1}{\Delta^n} \int_{\mathbf{r}_0 \in \mathbb{R}^3} \rho(\mathbf{r}_0) \int_{\mathbf{r} \in \mathbb{R}^3} ((\mathbf{r} - \mathbf{r}_0) \cdot \mathbf{u}_{\mathbf{g}})^{2n} P(\mathbf{r}, \Delta|\mathbf{r}_0) d\mathbf{r} d\mathbf{r}_0. \quad (1.18)$$

Thus in the narrow pulse limit, the derivatives of S give the moments of the probability density function $P(\mathbf{r}, t|\mathbf{r}_0)$, averaged over all starting positions \mathbf{r}_0 . For general pulse sequences, Eq. (1.18) is not exact.

In general, the first and second derivatives of S can be related to the Apparent Diffusion Coefficient and the Apparent Diffusion Kurtosis [36, 37] computed in dMRI:

$$ADC_0 = -\frac{d \log S}{db}(0) = -\frac{dS}{db}(0), \quad (1.19)$$

$$ADK_0 = 3 \frac{d^2 \log S}{db^2}(0) \left(\frac{d \log S}{db}(0) \right)^{-2} = 3 \frac{d^2 S}{db^2}(0) \left(\frac{dS}{db}(0) \right)^{-2} - 3, \quad (1.20)$$

where we denoted the quantities by ADC_0 and ADK_0 , respectively, to emphasize that the derivatives of $\log S(b)$ are taken at $b = 0$. The ADC_0 gives an indication of the mean squared distance traveled by water molecules, averaged over all the compartments, and ADK_0 gives an indication of the deviation from Gaussian diffusion.

1.8 Biological tissue dMRI

The signal measured by the MRI scanner is a mean-value measurement in a physical volume, called a voxel, whose size is much larger than the scale of the microscopic variations of the cellular structure. The resolution of dMRI is on the order of 1 mm³, meaning the dMRI signal combines the diffusion characteristics of a tissue volume (voxel) of 1 mm³. This is very large compared to cell features, which vary from sub- μm (diameter of neurites) to tens of μm (diameter of neuronal bodies, axons and glial cells) in the brain (see for example, [85]). In other words, dMRI provides the averaged characteristics of the microscopic structure on a macroscopic scale. Another important spatial scale to consider for this work is the diffusion distance, which gives an indication of the displacement of water molecules during the measured diffusion time. At physically realistic dMRI diffusion times of 10-100 ms, the average diffusion distance is, assuming an average diffusivity of 10⁻³ mm²/s, between 8-25 μm . Thus, from the diffusion point of view, the cellular structure

Chapter 1. Diffusion magnetic resonance imaging in biological tissues

beyond tens of μm from the starting positions of water molecules do not alter their displacements.

Voxel-level signal models accounting for heterogeneous domains

2.1 Diffusion models for brain tissue

One of the first analytical models of water diffusion in neural tissue was proposed by Szafer *et al.* [86]. Modeling a tissue as a regular lattice of cylinders, they derived approximate expressions for the apparent diffusion coefficients (ADCs) at long times. Ford and Hackney have implemented a Monte Carlo simulation of water self-diffusion among permeable cylindrical barriers to calculate the ADC in spinal cord injury which takes into account the distribution of axon diameters, permeability and relative axonal volume [80]. The numerical results indicated that both axonal swelling and cell membrane permeability were important factors contributing to ADC in traumatic spinal cord injury. Grant *et al.* reported an experimental evidence of multicomponent diffusion in single neurons [87]. Clark and co-workers studied experimentally the diffusion time dependence of the water diffusion tensor in the range 8-80 ms and showed no evidence for a change in mean diffusivity, fractional anisotropy, or in the eigenvalues with diffusion time in healthy human brain [88]. They concluded that these findings were consistent with a model of unrestricted, but hindered water diffusion with semi-permeable membranes, likely originating from the extra-cellular space in which the average extra-cellular separation is less than 7 micrometers. Hwang *et al.* developed a 3D finite difference approximation of the diffusion equation on synthetic images of neuronal tissues [82]. By exploiting histologic images of neuronal tissues as input model, this method was proposed to investigate the water diffusion behavior inside biological tissues and potentially assessing the status of neural injury and regeneration. Assaf *et al.* considered infinitely long isolated cylinders to model brain white matter, with two contributions to the dMRI signal coming from hindered diffusion outside cylinders and restricted diffusion inside cylinders [89] (see also [90, 91]). Kroenke *et al.* explained non-monoexponential dMRI signal decay by restricted diffusion in an ensemble of differently oriented neuronal fibers [92]. Sen and Basser presented a simplified, but self-consistent modeling framework for predicting the long-time apparent diffusion coefficients of water parallel and perpendicular to a “pack” of identical thick-walled (myelinated) cylindrical tubes (axons) arranged periodically in a regular lattice and immersed in an outer medium [93]. The model of randomly oriented cylinders has

also been applied for the quantitative analysis of dMRI in lungs [94]. Jespersen *et al.* proposed a simplified model of neural cytoarchitecture intended to capture the essential features important for water diffusion as measured by NMR [95] (see also [96]). In their model, two contributions to the dMRI signal come from (i) the dendrites and axons, which are modeled as infinitely long isolated cylinders with two diffusion coefficients (parallel and perpendicular to the cylindrical axis), and (ii) water diffusion within and across all other structures (i.e., in extra-cellular space and glial cells), which is modeled as an isotropic monoexponential diffusion. This model was confronted to dMRI measurements in a formalin-fixed baboon brain and shown to be able to provide an estimate of dendrite density. The model predictions of neurite density in rats have been successfully compared to optical myelin staining intensity and stereological estimation of neurite volume fraction using electron microscopy [97]. Recently, water diffusion anisotropy measurements have been directly related to characteristics of neuronal morphology [98]. Budde and Frank introduced a biophysical model of neurite beading (i.e., focal enlargement and constriction) and showed that this mechanism was sufficient to substantially decrease ADC and thus rationalize experimental findings after ischemic stroke [75]. Some other theoretical models and concepts of brain dMRI have been reviewed in [99].

2.2 Some mathematical models

There are two spatial scales considered in this thesis, one is the microscopic (micrometer) scale, at which cellular structures are resolved, and the other is the macroscopic scale, at which the cell features are averaged over the entire voxel. At the microscopic scale, we assume that the true cell membranes are spatially neglected (not resolved).

The microscopic model to be considered in this thesis is the Multiple Compartment Bloch-Torrey partial differential equation (PDE) [60, 67], which is a generalization of the Bloch-Torrey equation to heterogeneous domains. The domain of the Multiple Compartments Bloch-Torrey PDE is a spatial volume on the order of a voxel that contains the cells and the extra-cellular space. The unknown function of the PDE represents the complex transverse water proton magnetization due to diffusion-encoding magnetic field gradient pulses (T_2 effects and the imaging gradients are neglected). The dMRI signal of this PDE model is the integral of the solution of the PDE over all spatial positions in the voxel at the echo time.

Concerning macroscopic models for the dMRI signal, some of the early ones are Gaussian models, obtained in the limit of long diffusion time. If the diffusion time is long enough that all the water molecules experience the same environment, the macroscopic model is simply described by a single *effective* diffusion tensor. In the presence of permeable cell membranes, various analytical formulas for the effective diffusion tensor for special geometries such as cubes and spheres can be found in [52, 100, 101]. For general cell shapes, while assuming no contiguous extra-cellular space, an analytical formula for the effective diffusion tensor can be found in [71], where the time dependence of the average diffusion distance is considered. In [102]

2.2. Some mathematical models

the effective diffusion tensor for general cell shapes in the presence of a contiguous extra-cellular space was formulated based on the solution of a set of Laplace PDEs.

Macroscopic models based on multiple compartment diffusion have also been formulated. For example, in the no-exchange models [93, 95, 103], the cylindrical-shaped neurites are separated from the surrounding space that form two compartments. When there is no water exchange between these two compartments, the total dMRI signal is just the sum of the signals from each of the compartments. We note that in these no-exchange models, non-Gaussian diffusion can be allowed in each compartment, and this flexibility can potentially result in the applicability of the models at shorter diffusion times. However, the weakness of the no-exchange models is that water is assumed to stay (mostly) in a single compartment during the diffusion time. Even though no-exchange models may be appropriate for the brain white matter, where the myelin layer around axons prevents significant water exchange between the axons and the extra-cellular space, it is not clear if the water exchange can be neglected in the gray matter, where the cell membranes are permeable.

There are two macroscopic models based on multiple diffusion compartments, where diffusion within each compartment is considered *Gaussian*.

The first is the Kärger model [47], which was originally developed for micro-porous crystallites. The Kärger model is obtained by supposing multiple Gaussian diffusion compartments, each covering the whole space, and the spin exchange between the compartments being described by standard first-order kinetics exchange. These assumptions lead to a system of coupled ODEs that describes the time evolution of the signals in the different compartments. The dMRI signal can be written explicitly in terms of the model parameters because the ODE system has constant coefficients. The Kärger model was obtained on the basis of phenomenological modeling of the experimentally obtained signal curves and is valid under the *narrow pulse* assumption, i.e., the duration of the gradient pulse should be short compared to the diffusion time. The Kärger model has been checked in certain parameter regimes by comparing its prediction with Monte Carlo simulations [73, 76, 104]. In particular, Fieremans *et al.* discussed limitations of the Kärger model [76]. The Kärger model has been used in biological tissue imaging [73, 105–112] to invert for model parameters.

Recently, directly from the microscopic Bloch-Torrey PDE defined on a heterogeneous domain, a new macroscopic model for the dMRI signal was formulated [113] using homogenization techniques [114], in particular, by matching asymptotic expansions of the solution of the Bloch-Torrey PDE in different spatial sub-domains that are divided from each other by cell membranes. The compartments of this macroscopic model are then associated to the biological cells and the extra-cellular space. The dMRI signal is given by the solution of a system of coupled ODEs, similar to the Kärger model, but the ODEs have time-dependent coefficients and the solution needs to be obtained numerically. The main advantage of this new macroscopic model is that it is not subject to the narrow pulse restriction, in contrast to the Kärger model. The gradient pulse can be long in duration and can have a general temporal profile $f(t)$. However, the new ODE model is subject to the other

two limitations of the Kärger model, namely, the diffusion in each compartment should be (approximately) Gaussian, and the exchange time scale is sufficiently different from the diffusion time scale to ensure linear kinetics exchange. See [76] for a discussion of these two limitations for the Kärger model. The work of [113] can be thought of as giving a sound mathematical basis to the Kärger model as well as generalizing it beyond narrow pulse. This chapter aims to validate the ODE model for some complex geometries.

2.3 The voxel

We will define simplified geometrical models of the brain tissue in a voxel, consisting of spheres and long cylinders of various orientations embedded in the extra-cellular space. The spheres represent the neuronal bodies and the glial cells, while the cylinders represent the neurites. Since the intersection between the neuronal body and the attached neurites has a small surface area, the exchange between them is expected to be small, and will be ignored. For the justification of this geometrical model we refer to [93, 97, 103]. In addition, for simplicity, we assume that the extra-cellular space is connected so that we can consider it as a single diffusion compartment.

2.3.1 Periodic extension of the voxel

Let V be the voxel to be simulated. We ignore the effect of the neighboring voxels on V because the diffusion distance in our simulations, a few tens of μm , is much smaller than the voxel size (on the order of 1 mm). This allows us to replace the neighbors of V by the identical copies of itself. This periodic construction has the advantage of simplifying the boundary conditions to put on the faces of V to account for the spins that enter and exit V during the simulation time.

2.3.2 (Periodic) representative volume of the voxel

In order to compare the dMRI signal of the microscopic PDE model and the macroscopic models we choose a computational domain C that contains a representative volume of V , the voxel to be simulated. In the three-dimensional simulations that follow, due to computational limitations, C is much smaller than the voxel. We will suppose that C is repeated in all three coordinate directions as many times as necessary to make up V . In order to study long cylindrical cells in three dimensions, we should construct the cylinders so that they are oriented in such a way that when C is periodically repeated, the cylinders are not “broken” at the faces of C . Given that V itself will be periodically repeated, we assume the periodic extension of the cellular configuration in C as many times as necessary in our simulations.

2.4 Microscopic multiple compartments Bloch-Torrey PDE

The microscopic model for the dMRI signal is the multiple compartment Bloch-Torrey PDE [26, 60]. In the following we do not include the dependence of the dMRI signal on the imaging gradients and the T_2 relaxation in order to simplify the presentation. It would be easy to include the T_2 term in the microscopic model as well as in the macroscopic models but, as we will show in the numerical results section, enough complexity is already present in our problem just from the presence of the cellular membranes, without any T_2 effects. For the same reason, we also make the intrinsic diffusion coefficient the same in all the compartments, denoting it by D^0 , the permeability the same on all the membranes, denoting it by κ , and the spin density the same in all compartments.

Inside the computational domain C , there will be one extra-cellular compartment Ω^e , and sphere compartments, Ω^{s_j} , $j = 1, \dots$, where each Ω^{s_j} is a sphere, and the cylinder compartments, Ω^{c_k} , $k = 1, \dots$, where each Ω^{c_k} is a (part of a long) cylinder. The union of the compartments is the computational domain $C = \bigcup_{l=\{e, \{s_j\}, \{c_k\}\}} \Omega^l$. When C is periodically repeated, obviously, so are the Ω^l 's. Finally, we note that one could also have membrane compartments, consisting of a thick layer of space around the surfaces of the cylinders and the spheres. For the macroscopic models to be discussed later, we can also group all cells with similar diffusion characteristics into a single compartment to simplify things. For example, if we do not want to distinguish between spheres of different radii, then we can define the union of all the spheres as one compartment in the macroscopic model. This redefinition makes no difference for the microscopic PDE model since each sphere is always distinct from the others but it is notationally convenient when we want to compare the PDE model and the macroscopic models compartment by compartment.

The complex transverse water proton magnetization $M^l(\mathbf{r}, t|\mathbf{g})$ in each compartment Ω^l satisfies the Bloch-Torrey PDE [26]:

$$\frac{\partial M^l(\mathbf{r}, t|\mathbf{g})}{\partial t} = -if(t)(\gamma \mathbf{g} \cdot \mathbf{r}) M^l(\mathbf{r}, t|\mathbf{g}) + \nabla \cdot (D^0 \nabla M^l(\mathbf{r}, t|\mathbf{g})), \quad \forall l. \quad (2.1)$$

We recall that the diffusion-encoding gradient is denoted by $\mathbf{g} = (g_1, g_2, g_3)$ and its time profile by $f(t)$, i is the imaginary unit, $\gamma = 2.675 \cdot 10^8$ rad/s/Tesla is the gyromagnetic ratio of the water proton.

We supplement the PDE (2.1) with interface conditions where Ω^l and Ω^n come in contact. We denote the interface between Ω^l and Ω^n by Γ^{ln} . One interface condition is the continuity of flux:

$$D^0 \left(\nabla M^l(\mathbf{y}, t|\mathbf{g}) \cdot \mathbf{n}^l(\mathbf{y}) \right) = -D^0 \left(\nabla M^n(\mathbf{y}, t|\mathbf{g}) \cdot \mathbf{n}^n(\mathbf{y}) \right), \quad \mathbf{y} \in \Gamma^{ln}, \quad (2.2)$$

where $\mathbf{n}^l(\mathbf{y})$ and $\mathbf{n}^n(\mathbf{y})$ are the *outward*-point normals to Ω^l and Ω^n at \mathbf{y} , so in fact $\mathbf{n}^l(\mathbf{y}) = -\mathbf{n}^n(\mathbf{y})$. The second interface condition,

$$D^0 \left(\nabla M^l(\mathbf{y}, t|\mathbf{g}) \cdot \mathbf{n}^l(\mathbf{y}) \right) = \kappa \left(M^l(\mathbf{y}, t|\mathbf{g}) - M^n(\mathbf{y}, t|\mathbf{g}) \right), \quad \mathbf{y} \in \Gamma^{ln}, \quad (2.3)$$

incorporates a permeability coefficient κ across Γ^{ln} and models the ease with which water crosses the interface [67]. The larger the κ , the easier the passage of water. Now we add the initial condition:

$$M(\mathbf{r}, 0|\mathbf{g}) = M_0, \quad \mathbf{r} \in \Omega^l, \quad \forall l, \quad (2.4)$$

where we assumed the uniform excitation of the nuclei over the whole voxel, with M_0 being the initial magnetization. Then, same as [83], we assume that the computational domain $C = [-L_1/2, L_1/2] \times [-L_2/2, L_2/2] \times [-L_3/2, L_3/2]$ is extended by periodic copies of itself. According to [83], the boundary conditions on ∂C are:

$$M(\mathbf{r}, t|\mathbf{g})|_{r_k=-L_k/2} = M(\mathbf{r}, t|\mathbf{g})|_{r_k=L_k/2} e^{i\theta_k(t)}, \quad k = 1, 2, 3, \quad (2.5)$$

$$\frac{\partial M(\mathbf{r}, t|\mathbf{g})}{\partial r_k} \Big|_{r_k=-L_k/2} = \frac{\partial M(\mathbf{r}, t|\mathbf{g})}{\partial r_k} \Big|_{r_k=L_k/2} e^{i\theta_k(t)}, \quad k = 1, 2, 3, \quad (2.6)$$

for each of the faces perpendicular to the three coordinate axes, where $\mathbf{r} = (r_1, r_2, r_3)$ and $\mathbf{g} = (g_1, g_2, g_3)$, and

$$\theta_k(t) = \gamma g_k L_k \int_0^t f(s) ds.$$

Thus, the complete mathematical problem of the microscopic multiple compartment Bloch-Torrey PDE for a representative geometry contained in the computational box C consists of the PDE (2.1), the interface conditions (2.2, 2.3), the initial condition (2.4), and the boundary conditions (2.5, 2.6).

2.5 Compartment magnetizations

Now we define the compartment magnetization, denoted \overline{M}^l , of the PDE model, as the integral of the magnetization in Ω^l :

$$\overline{M}_{PDE}^l(b, t) := \int_{\mathbf{r} \in \Omega^l} M^l(\mathbf{r}, t|\mathbf{g}) d\mathbf{r}, \quad 0 \leq t \leq TE, \quad (2.7)$$

where, following convention, the b-value is defined as:

$$b(\mathbf{g}) = \gamma^2 \|\mathbf{g}\|^2 \int_0^{TE} du \left(\int_0^u f(s) ds \right)^2. \quad (2.8)$$

The dMRI signal measured in experiments (without the imaging gradients and T_2 effects) corresponds to

$$S_{PDE}(b) := \sum_l \overline{M}_{PDE}^l(b, TE) = \sum_l \int_{\mathbf{r} \in \Omega^l} M^l(\mathbf{r}, TE|\mathbf{g}) d\mathbf{r}. \quad (2.9)$$

Because C is assumed to be periodically repeated in the voxel V , it is sufficient to take the above integrals of the magnetization over C only because the signal is the same as if the magnetization is taken over V (and correctly normalized).

2.6. Kärger model

We note that the compartment magnetization $\overline{M}_{PDE}^l(b, t)$ defined in Eq. (2.7), though cannot be directly measured by experiments, are meaningful mathematically for all $t \leq TE$ and all l . By computing the compartment magnetizations we gain insight about the time evolution of the magnetizations in the different compartments and how they mix.

In a dMRI experiment, the TE and sequence $f(t)$ are usually fixed while \mathbf{g} is varied in amplitude and/or in direction to obtain the signal at different b-values.

In the rest of the thesis, we will set the initial magnetization to $M_0 = \frac{1}{|C|}$, so that $S_{PDE}(b = 0) = 1$ and $\overline{M}_{PDE}^l(b, t = 0) = \frac{|\Omega^l|}{|C|} := v^l$, where $|\Omega^l|$ is the volume of Ω^l , $|C|$ is the volume of the computational domain, and v^l is the volume *fraction* of Ω^l . Then the signal $S_{PDE}(b)$ will be automatically normalized and it is also the signal *attenuation*.

2.6 Kärger model

In the formulation of the Kärger model [47], one starts with a system of PDEs for the concentration, $u^l(\mathbf{r}, t)$, of water in P Gaussian diffusion compartments: $l = 1, \dots, P$. The governing equations for diffusion within and the exchange between the compartments are:

$$\begin{aligned} \frac{\partial u^1(\mathbf{r}, t)}{\partial t} &= \nabla \overline{D}^1 \nabla u^1(\mathbf{r}, t) - \frac{u^1(\mathbf{r}, t)}{w^1} + \sum_{l=2, \dots, P} \frac{u^l(\mathbf{r}, t)}{\tau^{1l}}, \\ &\vdots \\ \frac{\partial u^P(\mathbf{r}, t)}{\partial t} &= \nabla \overline{D}^P \nabla u^P(\mathbf{r}, t) - \frac{u^P(\mathbf{r}, t)}{w^P} + \sum_{l=1, \dots, P-1} \frac{u^l(\mathbf{r}, t)}{\tau^{Pl}}, \end{aligned} \quad (2.10)$$

where $\mathbf{r} \in \mathbb{R}^3$, τ^{lm} is the residence time, and \overline{D}^l is the *effective* diffusion coefficient of compartment l . This formulation implies that each compartment covers all of \mathbb{R}^3 , i.e., all the compartments co-exist in the whole space. A physical foundation for this consideration relies on coarse-graining (or homogenization) of the tissue microstructure [76].

From the mass conservation, if we assume that the spin density is the same in all the compartments, w^1, \dots, w^P satisfy:

$$\frac{1}{w^m} = \frac{1}{v^m} \sum_{l=1, l \neq m}^P \frac{v^l}{\tau^{ml}}, \quad m = 1, \dots, P, \quad (2.11)$$

where the volume fractions v^l are normalized as

$$\sum_{l=1}^P v^l = 1. \quad (2.12)$$

The PDEs (2.10) are subject to initial conditions:

$$u^l(\mathbf{r}, 0) = v^l \tilde{\delta}(\mathbf{r}), \quad l = 1, \dots, P, \quad (2.13)$$

where $\tilde{\delta}(\mathbf{r})$ is the Dirac delta distribution. We used the notation $\tilde{\delta}$ to distinguish it from the width of the gradient pulse δ in the PGSE sequence.

In the Kärger model, the compartment magnetization $\overline{M}_{KAR}^l(b, t)$, arising from compartment l , under the narrow pulse approximation for the PGSE sequence, $\delta \ll \Delta$, has the following form:

$$\overline{M}_{KAR}^l(b, t) = \int_{\mathbf{r} \in \mathbb{R}^3} e^{i\delta \mathbf{g} \cdot \mathbf{r}} u^l(\mathbf{r}, t) d\mathbf{r}. \quad (2.14)$$

We note that the region of integration in Eq. (2.14) is \mathbb{R}^3 . Taking the time derivative of \overline{M}_{KAR}^l from Eq. (2.14) and using Green's identity, one gets

$$\begin{aligned} \frac{d\overline{M}_{KAR}^m(b, t)}{dt} = & - \left(\delta^2 \gamma^2 \mathbf{g}^T \overline{D}^m \mathbf{g} + \frac{1}{v^m} \sum_{l=1, l \neq m}^P \frac{v^l}{\tau^{ml}} \right) \overline{M}_{KAR}^m(b, t) \\ & + \sum_{l=1, l \neq m}^P \frac{1}{\tau^{ml}} \overline{M}_{KAR}^l(b, t), \quad m = 1, \dots, P. \end{aligned} \quad (2.15)$$

It is a system of coupled ODEs, subject to the initial conditions:

$$\overline{M}_{KAR}^l(b, 0) = v^l, \quad l = 1, \dots, P. \quad (2.16)$$

The analytical solution of Eqs. (2.15) can be obtained by finding the eigen-decomposition of the underlying $P \times P$ matrix.

For a standard sequence with two rectangular gradient pulses of duration δ , the diffusion time is $t = \Delta - \delta/3$. For this reason, we evaluate the dMRI signal at this time

$$S_{KAR}(b) = \sum_{l=1}^P \overline{M}_{KAR}^l(b, \Delta - \delta/3), \quad (2.17)$$

In the original Kärger model, the pulse duration δ was neglected and the signal was evaluated at $t = \Delta$. Keeping the term $\delta/3$ improves the quality of the Kärger model.

2.7 Macroscopic ODE model

The derivation of the macroscopic ODE model [113] starts with the multiple compartment Bloch-Torrey PDE (2.1–2.6) and uses periodic homogenization theory, where the voxel was assumed to be a periodic repetition of a representative volume C . Periodic homogenization theory was used because it is technically simpler than the generic (non-periodic) case. The nature of the homogenized model depends on the scaling chosen for the permeability coefficient with respect to the periodicity

2.7. Macroscopic ODE model

size. In [113] the scaling was chosen to provide a macroscopic ODE model that is closest to the Kärger model. The resulting ODE model, being the limit, when the size of biological cells tends to zero, of the signal of the microscopic model, is expected to be an approximation of the microscopic PDE model at low membrane permeability and long diffusion times.

Clearly, biological tissue is not periodic with any period. However, it is known in some similar contexts (see, for instance, [115, 116] for the case of porous media) that even for media that are not truly periodic, the homogenized limit obtained in the periodic case remains formally relevant for describing generic (non-periodic) cases, i.e., the obtained macroscopic equations for both configurations have the same analytical form (only the exact values of the coefficients would change).

The macroscopic ODE model obtained in Ref. [113] governs the time evolution of the compartment magnetizations defined in Eq. (2.7):

$$\begin{aligned} \frac{d\bar{M}_{ODE}^m(b, t)}{dt} = & - \left(c(t)\gamma^2 \mathbf{g}^T \bar{D}^m \mathbf{g} + \frac{1}{v^m} \sum_{l=1, l \neq m}^P \frac{v^l}{\tau_{ODE}^{ml}} \right) \bar{M}_{ODE}^m(b, t) \\ & + \sum_{l=1, l \neq m}^P \frac{1}{\tau_{ODE}^{ml}} \bar{M}_{ODE}^l(b, t), \quad m = 1, \dots, P, \end{aligned} \quad (2.18)$$

where it was proven that if each $\Omega^l \in C$ is connected, then the coefficient in row m and column l of the ODE system, for all $l \neq m$, is:

$$\frac{1}{\tau_{ODE}^{ml}} := \kappa \frac{|\Gamma^{ml}|}{|\Omega^l|}, \quad (2.19)$$

with the relationship:

$$\frac{\tau_{ODE}^{lm}}{\tau_{ODE}^{ml}} = \frac{|\Omega^m|}{|\Omega^l|} = \frac{v^m}{v^l}, \quad (2.20)$$

where $|\Gamma^{ml}|$ is the surface area of the interface between Ω^m and Ω^l .

We note here that Eq. (2.19) has been used as an *estimate* of the residence time in the Kärger model. However, the derivation of the ODE model is only rigorous for small permeabilities such that Eq. (2.19) holds. The validity of the ODE model, at least as derived in [113], is not guaranteed if Eq. (2.19) does not hold. Thus, for us, we take Eq. (2.19) as the *definition* of $\frac{1}{\tau_{ODE}^{ml}}$.

The mathematical derivation of the function $c(t)$ from the full multiple compartment Bloch-Torrey PDE can be found in [113]. Here we use a more intuitive derivation, by looking at the ODE satisfied by the integral of the solution of the Bloch-Torrey PDE in a *homogeneous* medium with the constant diffusion tensor \bar{D}^0 . In [30] it was shown for the general gradient time profile $f(t)$, by the use of the Laplace transform, the integral of the magnetization satisfies, at *any* time:

$$\bar{M}^{hom}(b, t) := \int_{\mathbb{R}^3} m(\mathbf{r}, t | \mathbf{g}) d\mathbf{r} = \exp \left(-\mathbf{g}^T \bar{D}^0 \mathbf{g} \gamma^2 \int_0^t du \left(\int_0^u f(s) ds \right)^2 \right), \quad 0 \leq t \leq TE.$$

We note that the above equation is valid for any $t \geq 0$, not just at the echo time TE . Then we *define* $c(t)$ as:

$$c(t) := \frac{-\frac{\partial \overline{M}^{hom}(b,t)}{\partial t}}{\mathbf{g}^T \overline{D}^0 \mathbf{g} \gamma^2 \overline{M}^{hom}(b,t)} = \left(\int_0^t f(s) ds \right)^2, \quad (2.21)$$

for any profile $f(t)$.

For the rectangular pulsed gradient spin echo (PGSE) sequence in Eq. (1.3), Eq. (2.21) implies

$$c(t) = \begin{cases} (t - t_0)^2, & t_0 \leq t \leq t_0 + \delta, \\ \delta^2, & t_0 + \delta < t \leq t_0 + \Delta, \\ (t - t_0 - \Delta - \delta)^2, & t_0 + \Delta < t \leq t_0 + \Delta + \delta. \end{cases} \quad (2.22)$$

See Fig. 2.1 for the shape of $c(t)$. In the narrow pulse regime, $\delta \ll \Delta$, we can see that Eq. (2.22) yields the coefficient δ^2 of the Kärger model.

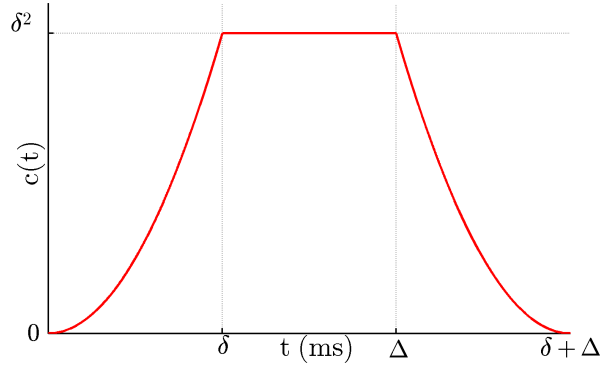


Figure 2.1: The function $c(t)$ for the rectangular PGSE profile, with $t_0 = 0$.

For the trapezoidal gradient shape in Eq. (1.4), it is easy to show that:

$$c(t) = \begin{cases} \left(\frac{(t-t_0)^2}{2\tau}\right)^2, & t_0 \leq t \leq t_0 + \tau, \\ \left((t-t_0) - \frac{1}{2}\tau\right)^2, & t_0 + \tau < t \leq t_0 + \delta - \tau, \\ \left(-\frac{((t-t_0)-\delta)^2}{2\tau} + \delta - \tau\right)^2, & t_0 + \delta - \tau < t \leq t_0 + \delta, \\ (\delta - \tau)^2, & t_0 + \delta < t \leq t_0 + \Delta, \\ \left(-\frac{((t-t_0)-\Delta)^2}{2\tau} + \delta - \tau\right)^2, & t_0 + \Delta < t \leq t_0 + \Delta + \tau, \\ \left(-\left((t-t_0) - \frac{1}{2}\tau + \delta + \Delta\right)\right)^2, & t_0 + \Delta + \tau < t \leq t_0 + \Delta + \delta - \tau, \\ \left(\frac{((t-t_0)-\delta-\Delta)^2}{2\tau}\right)^2, & t_0 + \Delta + \delta - \tau < t \leq t_0 + \Delta + \delta. \end{cases} \quad (2.23)$$

See Fig. 2.2 for the shape of $c(t)$.

2.7. Macroscopic ODE model

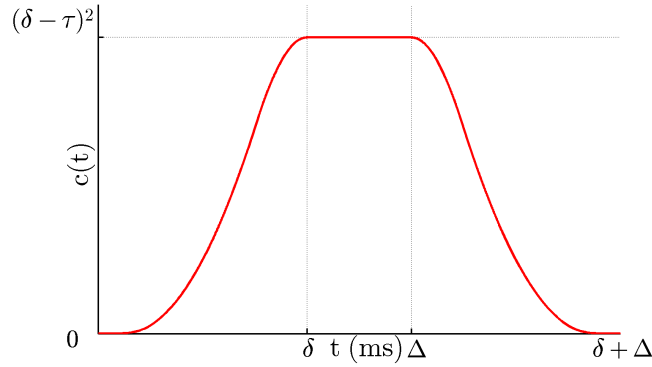


Figure 2.2: The function $c(t)$ for the trapezoidal PGSE profile, with $t_0 = 0$.

For the oscillating sine profile in Eq. (1.5), one gets:

$$c(t) = \begin{cases} \frac{1}{\omega^2} (\cos(\omega(t - t_0)) - 1)^2, & t_0 < t \leq t_0 + \sigma, \\ \frac{1}{\omega^2} (\cos(\omega(t - t_0 - \tau)) - 1)^2, & \tau + t_0 < t \leq t_0 + \tau + \sigma, \\ 0, & \text{otherwise.} \end{cases}$$

See Fig. 2.3 for the shape of $c(t)$.

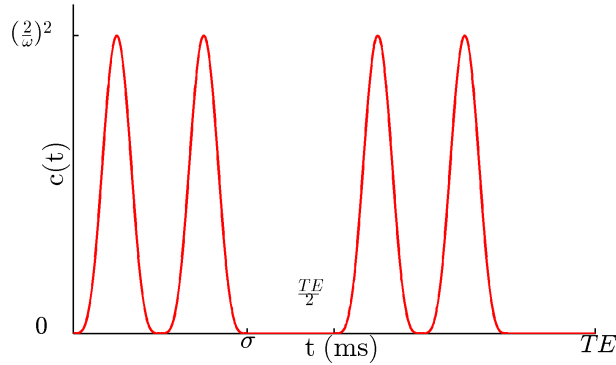


Figure 2.3: The function $c(t)$ for OGSE sine profile, each pulse contains 2 periods, with $t_0 = 0$.

Now we move to the definitions of the effective diffusion tensors. This is a rather delicate question because the effective diffusion tensors are much easier to define for a voxel V that contains many copies of C than for a generic voxel. In the first case, because all water molecules in V “see” only copies of C , and C is small compared to the diffusion distance, then the steady-state values of the effective diffusion tensors can be used. These steady-state quantities can be rigorously defined from the

solution of three Laplace (state-state) PDEs in C where periodic conditions on the faces of C are imposed. We will present these steady-state equations shortly. However, if V is a generic voxel, or in other words, the representative volume C is on the order of a voxel (hence, V is not periodic), it is not reasonable to suppose that the steady-state values computed on C with periodic boundary conditions would be achieved at diffusion times where the diffusion distance is much smaller than C .

In [113], it was shown that if we assume the periodic extension of $C = [-L_1/2, L_1/2] \times [-L_2/2, L_2/2] \times [-L_3/2, L_3/2]$ to the voxel where C is small compared to the diffusion distance, the effective diffusion tensors \bar{D}^m 's are quantities that can be obtained after solving three steady-state Laplace PDEs. Specifically, for Ω^m , it is

$$\bar{D}_{j,k}^m = \frac{1}{v^m} \int_{\Omega^m} D(\mathbf{r}) \nabla m_j(\mathbf{r}) \cdot \mathbf{e}_k \, d\mathbf{r}, \quad j, k = 1, \dots, 3, \quad (2.24)$$

where \mathbf{e}_k is the unit vector in the k^{th} direction, and we have to solve 3 steady-state Laplace equations over C for the unknown functions $m_j(\mathbf{r})$:

$$\nabla \cdot (D^0 \nabla m_j(\mathbf{r})) = 0, \quad \mathbf{r} \in \Omega^m, \quad (2.25)$$

subject to *impermeable* boundary condition on $\partial\Omega^m$:

$$\nabla m_j(\mathbf{y}) \cdot \mathbf{n}(\mathbf{y}) = 0, \quad \mathbf{y} \in \partial\Omega^m, \quad (2.26)$$

and *periodic* boundary conditions on ∂C :

$$m_j(\mathbf{r})|_{r_k=-L_k/2} = m_j(\mathbf{r})|_{r_k=L_k/2} - \delta_{j,k} L_k, \quad k = 1, \dots, 3, \quad (2.27)$$

$$\frac{\partial}{\partial r_k} m_j(\mathbf{r})|_{r_k=-L_k/2} = \frac{\partial}{\partial r_k} m_j(\mathbf{r})|_{r_k=L_k/2}, \quad k = 1, \dots, 3, \quad (2.28)$$

where $\delta_{j,k} = 1$ if $k = j$, and $\delta_{j,k} = 0$, otherwise. We emphasize that functions $m_j(\mathbf{r})$ are independent of the permeability and diffusion gradient. As a consequence,

1. The permeability coefficient does not enter into the definition of \bar{D}^m . In other words, the analysis was done around the low permeability limit $\kappa = 0$.
2. \bar{D}^m is a physical characteristic of the cellular geometry, it does not depend on the diffusion gradient.

It is easy to show that if the periodic extension of Ω^m is compact, namely, if Ω^m is a sphere compartment, then its effective diffusion tensor is 0:

$$\bar{D}^m = 0. \quad (2.29)$$

We account for long cylindrical cells by supposing the radius of the cylinder is small, and setting its effective diffusion tensor to:

$$\bar{D}^m = \mathbf{a} D^0 \mathbf{a}^T, \quad (2.30)$$

2.8. Limiting cases

where \mathbf{a} is the normalized ($\|\mathbf{a}\| = 1$) vector parallel to the axis of the cylinder. We will construct the computational domain C so that when it is periodically repeated, the Ω^m that corresponds to a cylinder becomes infinitely long along its longitudinal direction. We note that the expressions (2.19, 2.29, 2.30) have been used in previous works (for example, in [76]) for the Kärger model.

The initial condition of the ODE model is the same as for the Kärger model, namely, Eq. (2.16), and the dMRI signal for the ODE model is

$$S_{ODE}(b) = \sum_{l=1}^P \overline{M}_{ODE}^l(b, TE). \quad (2.31)$$

2.8 Limiting cases

Finally, we note that if there is no exchange ($\kappa = 0$) between any of the compartments, the macroscopic dMRI signal is

$$S_{NOEX}(b) = \sum_{m=1}^P v^m \exp\left(-\frac{\mathbf{g}^T \overline{D}^m \mathbf{g}}{\|\mathbf{g}\|^2} b\right), \quad (2.32)$$

where diffusion in each compartment is still considered as Gaussian. If the exchange between the compartments are infinitely fast ($\kappa = \infty$), then the dMRI signal is:

$$S_{FASTEX}(b) = \exp\left(-\left(\sum_{m=1}^P v^m \frac{\mathbf{g}^T \overline{D}^m \mathbf{g}}{\|\mathbf{g}\|^2}\right) b\right). \quad (2.33)$$

The Kärger model and the ODE model are formulated to explain the intermediate exchange regime that falls between the two extreme cases in Eqs. (2.32, 2.33).

One important property of both the Kärger model and the ODE model is that the ADC_0 is independent of time and of κ :

$$ADC_0^{KAR} = ADC_0^{ODE} = ADC_0^{FASTEX} = ADC_0^{NOEX} = \sum_{m=1}^P v^m \frac{\mathbf{g}^T \overline{D}^m \mathbf{g}}{\|\mathbf{g}\|^2}. \quad (2.34)$$

Thus, two necessary conditions for the applicability of these macroscopic models are: (i) the diffusion time should be long enough that the measured ADC_0 does not change (much) with time, and (ii) the cell membrane permeability κ should be low enough that it does not affect (much) the ADC_0 .

Numerical study of two macroscopic dMRI signal models

3.1 Method

We solved the multiple compartment Bloch-Torrey PDE in the computational domain C containing different cellular configurations using the finite elements method described in [84]. We generated the finite elements mesh in the computational domain C using the mesh generation platform Salome (<http://www.salome-platform.org/>). The computational domain C was chosen to contain a configuration of spheres and cylinders. The angles of the cylinders were chosen so that when C is periodically repeated, the cylinders become infinitely long. In the simulations, the extra-cellular fractions were between 0.31 and 0.51, higher than in brain tissue. Due to computational limitations of the three-dimensional simulations, C will be much smaller than a voxel. In all cases, the cellular configurations were constructed so that at the diffusion times simulated, all the diffusion compartments are (close to) Gaussian.

We set the intrinsic diffusion coefficient in all the compartments to be $D^0 = 3 \times 10^{-3} \text{mm}^2/\text{s}$. The initial magnetization was set to $\frac{1}{|C|}$ for all the compartments to normalize the dMRI signals to 1 at $b = 0$. For simplicity, for both the rectangular and trapezoidal PGSE sequences, we set $t_0 = 0$ and TE to be immediately after the diffusion-encoding sequence.

We computed the dMRI signal at 20 b-values between 0 and $4000 \text{s}/\text{mm}^2$. We will compare the following 5 models of the dMRI signal:

1. “PDE”: The (microscopic) multiple compartment Bloch-Torrey PDE.
2. “ODE”: The (macroscopic) ODE model.
3. “KAR”: The (macroscopic) Kärger model.
4. “NO EX”: The (macroscopic) No Exchange signal.
5. “FAST EX”: The (macroscopic) Fast Exchange signal.

The signals will be labeled as the above in the figures. We will also plot the compartment magnetizations, $\overline{M}_{PDE}^l(b, t)$, $\overline{M}_{ODE}^l(b, t)$ and $\overline{M}_{KAR}^l(b, t)$, for the different compartments as a function of time.

Chapter 3. Numerical study of two macroscopic dMRI signal models

The simulations were performed on a Dell PRECISION M4700 workstation (Intel(R) Core(TM)i7 CPU 3740QM@2.70GB). The solution of the microscopic Bloch-Torrey PDE took between 4 seconds to 37 minutes, per b-value, depending on the complexity of the cellular configuration and timing for gradient profile. The memory usage was between 28Mbytes to 409Mbytes. Table 3.1 shows the details of simulation time and memory usage. The ODE model was solved using the Matlab (home built) command “ode45”. The solution of the ODE took a few seconds per b-value. The memory usage was negligible.

Domain	Memory (MB)	Computational time	
		$\delta = \Delta = 5\text{ms}$	$\delta = \Delta = 40\text{ms}$
1 Sphere	36	15 seconds	38 seconds
76 spheres	409	15 minutes	37 minutes
Slanted parallel cylinders	36	15 seconds	37 seconds
3-compartments cylinder	28	4 seconds	10 seconds
Cylinders + spheres	227	8 minutes	22 minutes

Table 3.1: Memory usage and average computational time per b-value to solve the Bloch-Torrey PDE.

3.2 Numerical study

In this section, we will first illustrate the properties of the ODE model on a simple cellular configuration where C contains a single sphere as we vary the gradient pulse shape, the diffusion time, the cell permeability, and the cell radius. Then we put more complex three-dimensional cellular configurations inside C where C has side lengths varying between $5 - 15\mu\text{m}$.

3.2. Numerical study

3.2.1 Periodic lattice of spheres

We study the properties of the ODE model using a simple geometry of a periodic lattice of spheres. The computational domain is $C = [-2.5\mu\text{m}, 2.5\mu\text{m}]^3$. Inside C we placed one sphere of radius $R^s = 2.45\mu\text{m}$. The finite elements mesh for C is shown in Fig. 3.2(a). The gradient direction is $\mathbf{g} = [1, 0, 0]$.

This domain contains two compartments: the extra-cellular compartment Ω^e and the sphere compartment Ω^s . The corresponding volume fractions are $v^e = 0.51$ and $v^s = 0.49$. The surface area between the two compartments is $|\Gamma^{se}| = 75\mu\text{m}^2$. The effective diffusion coefficient of Ω^s is $\overline{D}^s = 0$ because the sphere is compact. We computed the effective diffusion tensor of Ω^e according to Eq. (2.24) to be:

$$\overline{D}^e = \begin{bmatrix} 2.32 & 0.00 & 0.00 \\ 0.00 & 2.32 & 0.00 \\ 0.00 & 0.00 & 2.32 \end{bmatrix} \times 10^{-3} \text{mm}^2/\text{s}.$$

We remind that the effective diffusion tensor describes the asymptotic behavior at (infinitely) long times.

3.2.1.1 Residence time

Now we verify the analytical formula of the residence time in Eq. (2.19) for the periodic lattice of spheres (Fig. 3.2(a)) by solving the Bloch-Torrey PDE with zero gradient, $\mathbf{g} = 0$, in other words, the diffusion equation, to obtain the compartment magnetizations $\overline{M}_{PDE}^e(0, t)$ and $\overline{M}_{PDE}^s(0, t)$ at different times: $t \in [0, 20]$ ms. If the compartment magnetizations can be approximated by an ODE model of the form given in (2.18), then necessarily:

$$\begin{aligned} \frac{d\overline{M}_{PDE}^e(0, t)}{dt} &\approx -\frac{1}{\tau^{se}}\overline{M}_{PDE}^e(0, t) + \frac{1}{\tau^{es}}\overline{M}_{PDE}^s(0, t), \\ \frac{d\overline{M}_{PDE}^s(0, t)}{dt} &\approx -\frac{1}{\tau^{es}}\overline{M}_{PDE}^s(0, t) + \frac{1}{\tau^{se}}\overline{M}_{PDE}^e(0, t). \end{aligned} \quad (3.1)$$

Using the relation (2.20), we can obtain the best fit τ^{es} at t :

$$\tau_{fit}^{es}(t) := \frac{\frac{v^e}{v^s}\overline{M}_{PDE}^e(0, t) - \overline{M}_{PDE}^s(0, t)}{\frac{d\overline{M}_{PDE}^s(0, t)}{dt}}. \quad (3.2)$$

To prevent the denominator of (3.2) from being zero, we choose an initial condition for the Bloch-Torrey PDE that is not the equilibrium solution. For example, setting

$$M(\mathbf{r}, 0|\mathbf{g}) = 1, \quad \mathbf{r} \in \Omega^s, \quad (3.3)$$

$$M(\mathbf{r}, 0|\mathbf{g}) = 0, \quad \mathbf{r} \in \Omega^e, \quad (3.4)$$

would suffice.

Now we compare the analytical approximation τ^{es} in Eq. (2.19) with $\tau_{fit}^{es}(t)$ in Eq. (3.2). We solved the PDE using the intrinsic diffusion coefficient $D^0 = 3 \times$

Chapter 3. Numerical study of two macroscopic dMRI signal models

$10^{-3}\text{mm}^2/\text{s}$ and two different values of permeability: $\kappa = 1 \times 10^{-5}\text{m/s}$ (Fig. 3.1(a)) and $\kappa = 1 \times 10^{-4}\text{m/s}$ (Fig. 3.1(b)), corresponding to two values of the residence time: $\tau^{es} = 81\text{ms}$ and $\tau^{es} = 8.1\text{ms}$, respectively. One can see on both Fig. 3.1(a) and Fig. 3.1(b) that $\tau_{fit}^{es}(t)$ is a constant for $t \in [0, 20]\text{ms}$. At the lower permeability $\kappa = 1 \times 10^{-5}\text{m/s}$, $\tau_{fit}^{es}(t)$ is very close to τ^{es} . At the higher permeability $\kappa = 1 \times 10^{-4}\text{m/s}$, there is a small difference between $\tau_{fit}^{es}(t)$ and τ^{es} , the relative difference being about 4%.

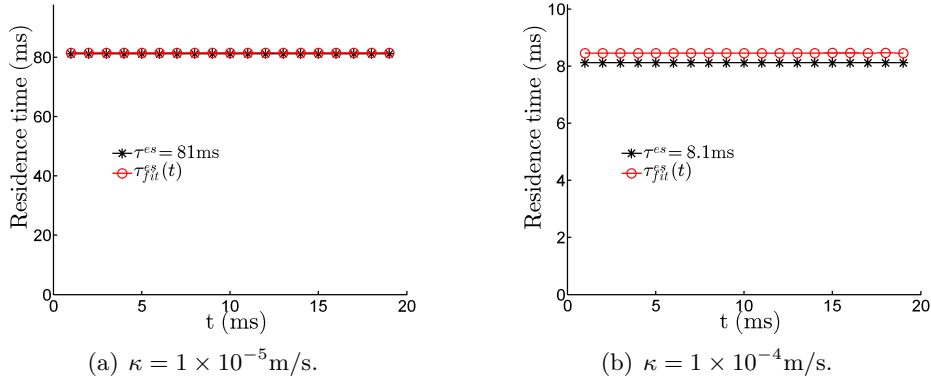


Figure 3.1: Verification for the residence time τ^{es} at two permeabilities (a) $\kappa = 1 \times 10^{-5}\text{m/s}$, (b) $\kappa = 1 \times 10^{-4}\text{m/s}$.

3.2.1.2 Compartment magnetization

We set the cell permeability to $\kappa = 10^{-5}\text{m/s}$. Applying a PGSE sequence with $\delta = 40\text{ms}$, $\Delta = 40\text{ms}$, we see that the $S_{ODE}(b)$ is very close to $S_{PDE}(b)$, whereas $S_{KAR}(b)$ is further away (Fig. 3.2(b)). We also show the compartment magnetizations in Ω^e and Ω^s from $t = 0\text{ms}$ to $t = 80\text{ms}$ at $b = 2000\text{s/mm}^2$ (Fig. 3.2(c) and Fig. 3.2(d)). We see that $\overline{M}_{ODE}^e(2000, t)$ and $\overline{M}_{ODE}^s(2000, t)$ follow the time evolution of $\overline{M}_{PDE}^e(2000, t)$ and $\overline{M}_{PDE}^s(2000, t)$, whereas the Kärger model compartment magnetizations $\overline{M}_{KAR}^e(2000, t)$ and $\overline{M}_{KAR}^s(2000, t)$ do not.

Next we apply a gradient sequence with two trapezoidal pulses, each pulse lasting 40ms. See Fig. 3.3(a) for the profile of $f(t)$. Figure 3.3(c) presents the dMRI signals, $S_{PDE}(b)$ and $S_{ODE}(b)$, while Fig. 3.3(e) shows the sum of the compartment magnetizations, $\overline{M}_{PDE}^e(2000, t) + \overline{M}_{PDE}^s(2000, t)$, $\overline{M}_{ODE}^e(2000, t) + \overline{M}_{ODE}^s(2000, t)$, as a function of time, at $b = 2000\text{s/mm}^2$. Then we apply a gradient sequence with four trapezoidal pulses, each pulse lasting 20 ms. See Fig. 3.3(b) for the profile of $f(t)$, while the signal and compartment magnetizations are shown in Fig. 3.3(d) and Fig. 3.3(f), respectively. These results for $\kappa 10^{-5}\text{m/s}$ (relatively slow exchange) indicate that the ODE model correctly reproduces the time evolution of the water proton magnetization in different compartments over the *entire time course* of the gradient sequence, even for complicated gradient shapes.

3.2. Numerical study

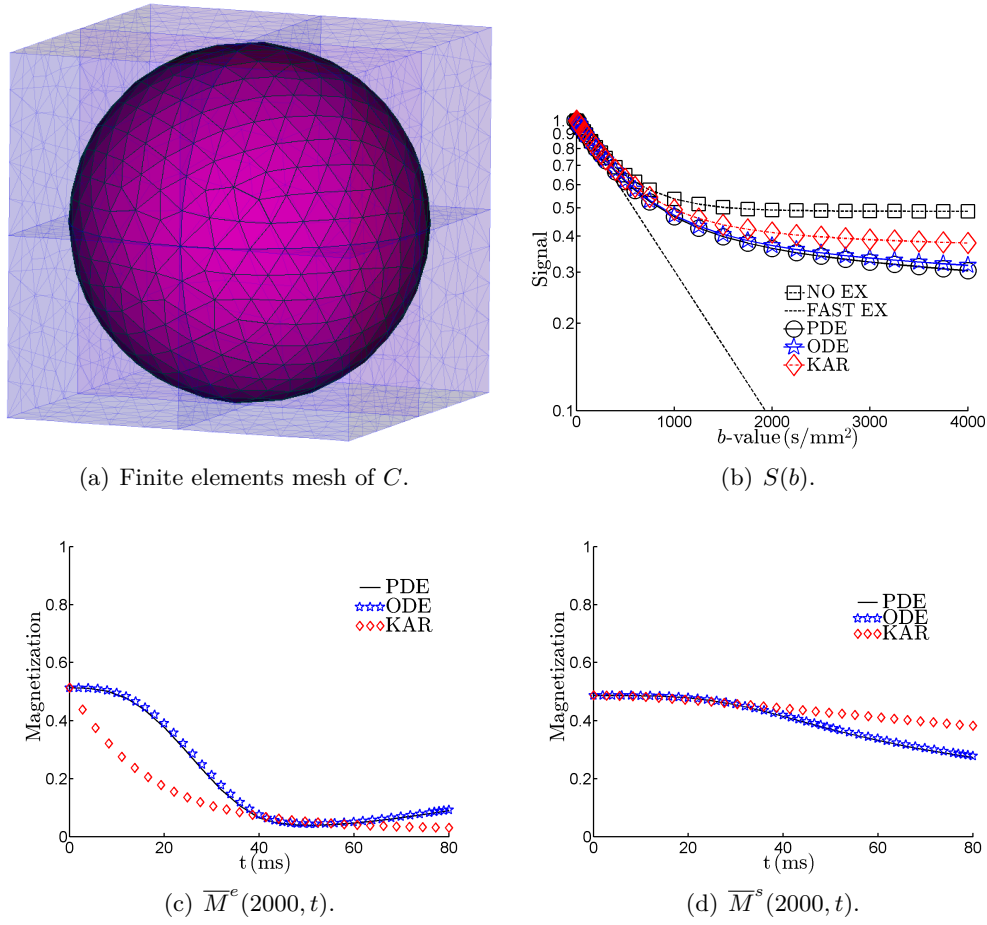


Figure 3.2: (a) Finite elements mesh of C ; (b) DMRI signals: $S_{PDE}(b)$, $S_{ODE}(b)$, $S_{NOEX}(b)$, $S_{FASTEX}(b)$; (c) Compartment magnetization in the extra-cellular compartment at $b = 2000\text{s/mm}^2$: $\overline{M}_{PDE}^e(2000, t)$, $\overline{M}_{ODE}^e(2000, t)$; (d) Compartment magnetization in the sphere at $b = 2000\text{s/mm}^2$: $\overline{M}_{PDE}^s(2000, t)$, $\overline{M}_{ODE}^s(2000, t)$. Cell radius $2.45\mu\text{m}$, $\kappa = 10^{-5}\text{m/s}$. PGSE sequence with $\delta = \Delta = 40\text{ms}$.

We also apply a gradient sequence of OGSE sine without gap time between two pulses and with one period in each pulse, each period lasting 40ms. See Fig. 3.4(a) for the profile of $f(t)$. Figure 3.4(c) presents the dMRI signals, $S_{PDE}(b)$ and $S_{ODE}(b)$, while Fig. 3.4(e) shows the sum of the compartment magnetizations, $\overline{M}_{PDE}^e(2000, t) + \overline{M}_{PDE}^s(2000, t)$, $\overline{M}_{ODE}^e(2000, t) + \overline{M}_{ODE}^s(2000, t)$, at $b = 2000\text{s/mm}^2$. Then we also apply a gradient sequence of OGSE sine with two periods in each pulse, each period lasting 20 ms. See Fig. 3.3(b) for the profile of $f(t)$. Figures 3.3(d) and 3.3(f) show similar results to that of trapezoidal shape sequences.

Chapter 3. Numerical study of two macroscopic dMRI signal models

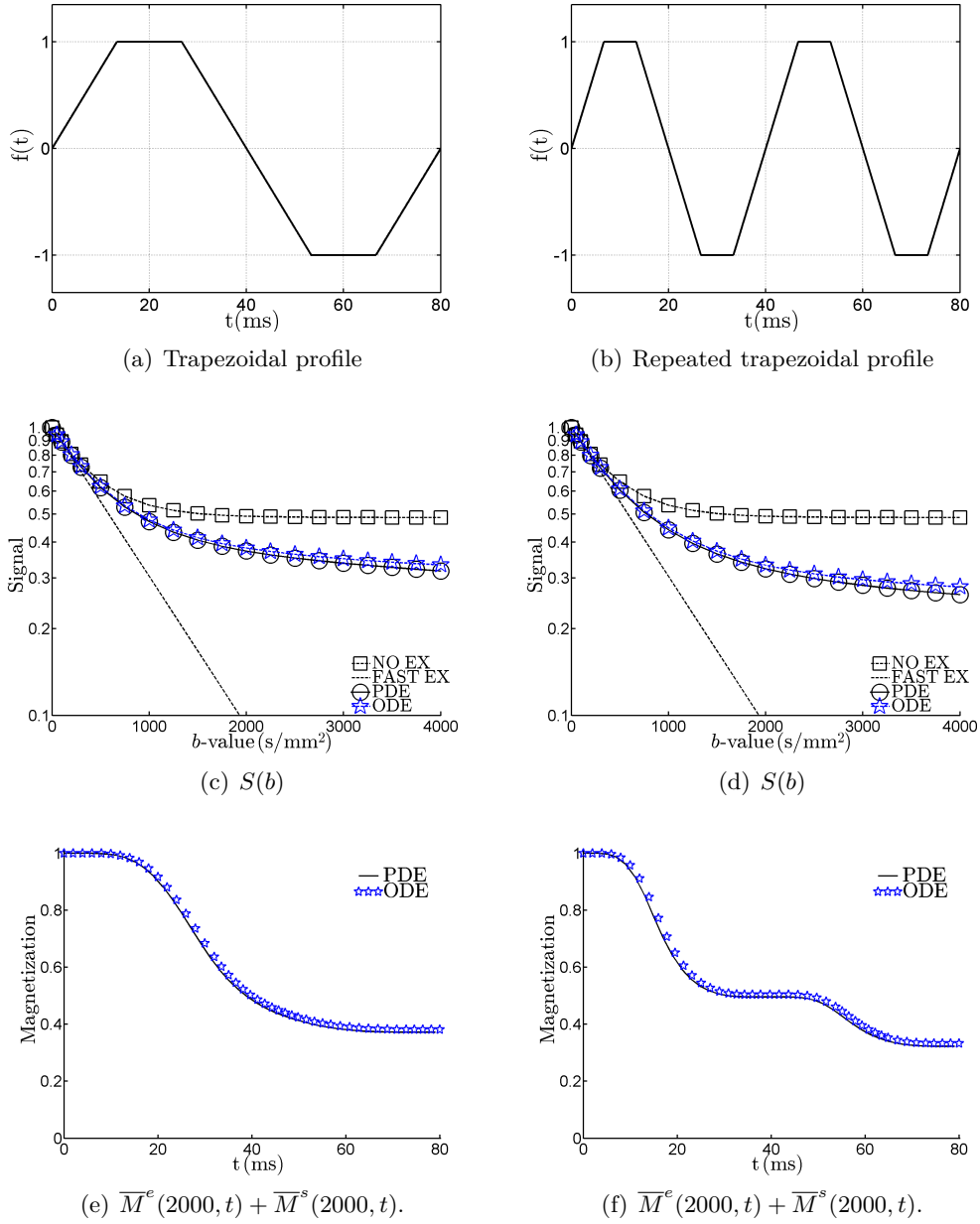
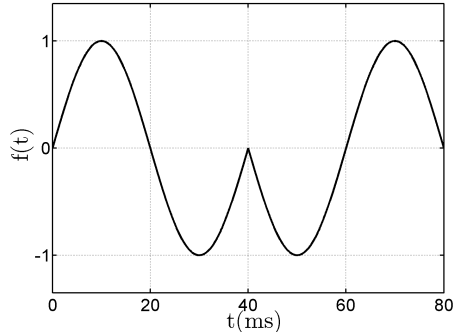
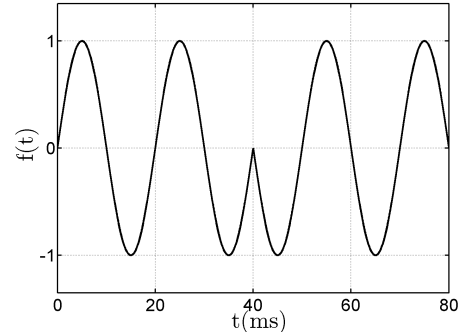


Figure 3.3: The domain is a periodic lattice of spheres, $R^s = 2.45\mu\text{m}$, $\kappa = 10^{-5}\text{m/s}$. Top: the gradient profiles: (a) two pulses $\delta = \Delta = 40\text{ms}$, $\tau = \delta/3$, (b) four pulses $\delta = \Delta = 20\text{ms}$, $\tau = \delta/3$. Middle: the dMRI signal, $S_{PDE}(b)$, $S_{ODE}(b)$, as a function of b-value. Bottom: the sums of the compartment magnetizations $\bar{M}_{PDE}^e(2000, t) + \bar{M}_{PDE}^s(2000, t)$, $\bar{M}_{ODE}^e(2000, t) + \bar{M}_{ODE}^s(2000, t)$, as a function of time at $b = 2000\text{s/mm}^2$.

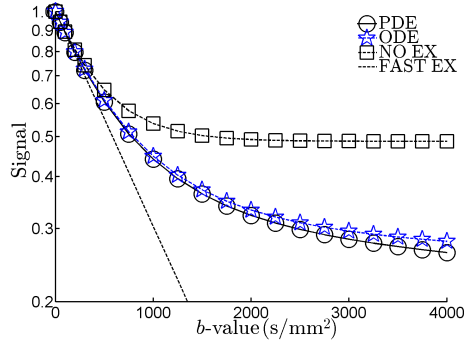
3.2. Numerical study



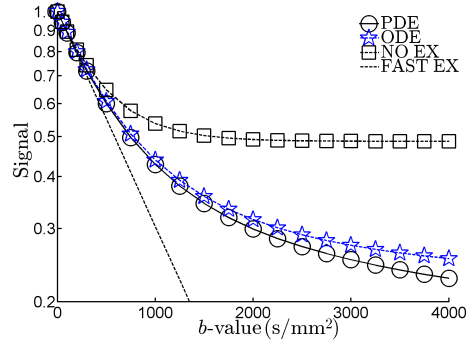
(a) OGSE sine profile: 1 period in each pulse.



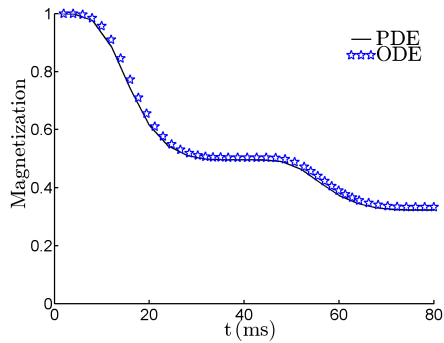
(b) OGSE sine profile: 2 periods in each pulse.



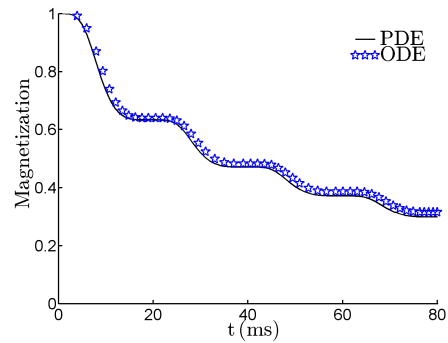
(c) $S(b)$.



(d) $S(b)$.



(e) $\bar{M}^e(2000, t) + \bar{M}^s(2000, t)$.

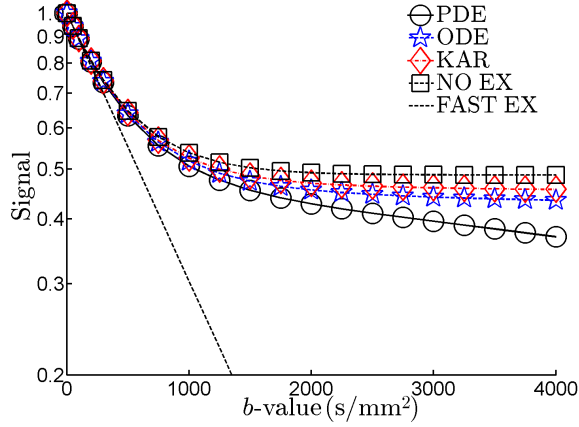


(f) $\bar{M}^e(2000, t) + \bar{M}^s(2000, t)$.

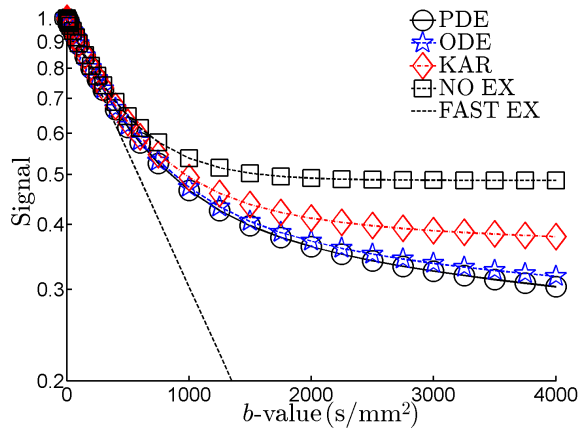
Figure 3.4: The domain is a periodic lattice of spheres, $R^s = 2.45\mu\text{m}$, $\kappa = 10^{-5}\text{m/s}$. Top: the gradient profiles. Middle: the dMRI signal, $S_{PDE}(b)$, $S_{ODE}(b)$, $S_{KAR}(b)$, as a function of b-value. Bottom: the sums of the compartment magnetizations $\bar{M}_{PDE}^e(2000, t) + \bar{M}_{PDE}^s(2000, t)$, $\bar{M}_{ODE}^e(2000, t) + \bar{M}_{ODE}^s(2000, t)$ as a function of time at $b = 2000\text{s/mm}^2$.

3.2.1.3 Diffusion time

Now we consider the convergence of the ODE model to the PDE model. Comparing a short diffusion time PGSE sequence with $\delta = \Delta = 10\text{ms}$ (Fig. 3.5(a)) to a long diffusion time PGSE sequence with $\delta = \Delta = 40\text{ms}$ (Fig. 3.5(b)), we see that $S_{ODE}(b)$ becomes closer to $S_{PDE}(b)$ as the diffusion time increases.



(a) PGSE, $\delta = 10\text{ms}$, $\Delta = 10\text{ms}$.



(b) PGSE, $\delta = 40\text{ms}$, $\Delta = 40\text{ms}$.

Figure 3.5: The domain is a periodic lattice of spheres, $R^s = 2.45\mu\text{m}$, $\kappa = 10^{-5}\text{m/s}$. $S_{ODE}(b)$ is closer to $S_{PDE}(b)$ for longer diffusion time.

3.2. Numerical study

3.2.1.4 Membrane permeability

Next, we consider the effect of membrane permeability. Figure 3.6 shows $S_{PDE}(b)$ and $S_{ODE}(b)$ of the spherical cell domain for different permeabilities: $\kappa = 10^{-5}\text{m/s}$, $\kappa = 2.5 \times 10^{-5}\text{m/s}$, $\kappa = 5 \times 10^{-5}\text{m/s}$, with two PGSE sequences: $\delta = \Delta = 10\text{ms}$ and $\delta = \Delta = 80\text{ms}$. We can see that at lower permeabilities (Fig. 3.6(a) and 3.6(b)), $S_{ODE}(b)$ is closer to $S_{PDE}(b)$ for longer diffusion time. In contrast, at higher permeability (Fig. 3.6(c)), the distance between $S_{ODE}(b)$ and $S_{PDE}(b)$ does not become smaller. This is expected because of stronger mixing between compartments at higher permeabilities.

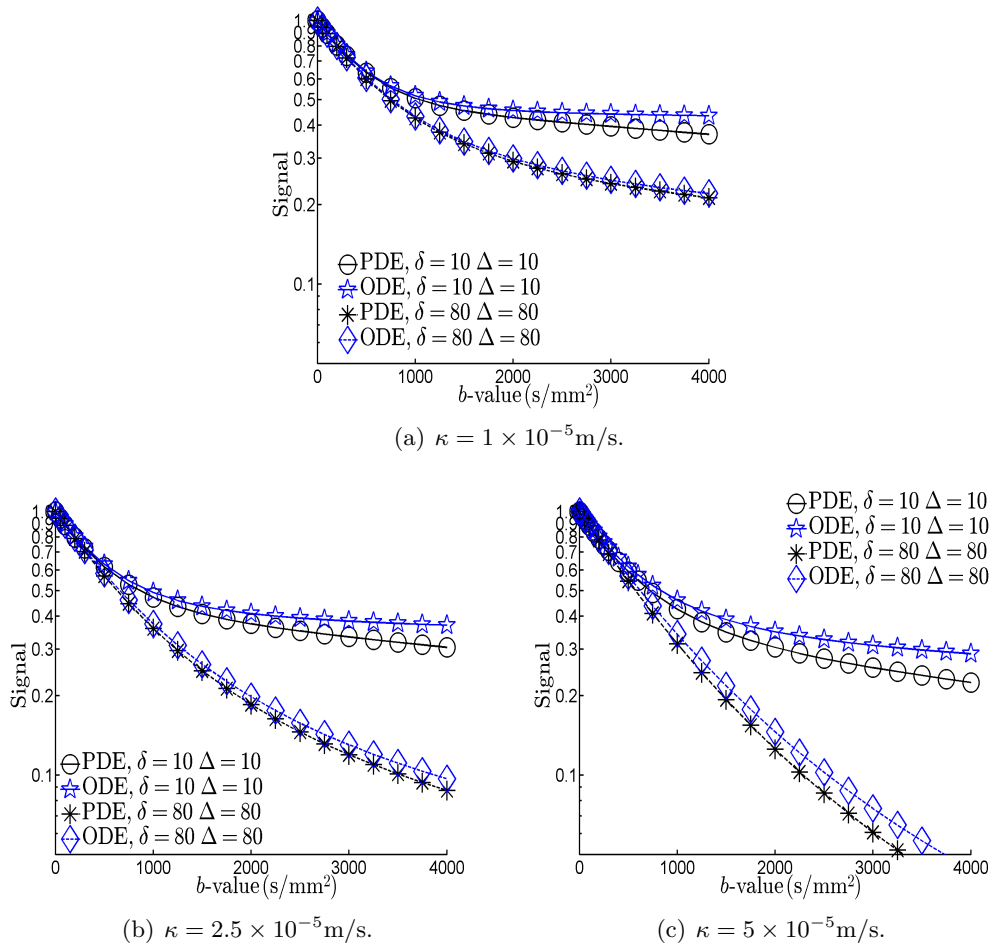


Figure 3.6: The domain is a periodic lattice of spheres, $R^s = 2.45\mu\text{m}$. The gradient sequence is PGSE with $\delta = 10\text{ms}$, $\Delta = 10\text{ms}$ and $\delta = 80\text{ms}$, $\Delta = 80\text{ms}$. The accuracy of the ODE model (as compared to the PDE model) improves as the diffusion time increases, if the permeability is low.

3.2.1.5 Cell size

Now we double the radius of the sphere to $R^s = 4.9\mu\text{m}$ as well as double the size of the computational domain, to $C = [-5\mu\text{m}, 5\mu\text{m}]^3$. This keeps the same volume fractions, $v^e = 0.51$, $v^s = 0.49$, but halves the surface-to-volume ratio. For this domain, we computed

$$\overline{D}^e = \begin{bmatrix} 2.32 & 0.00 & 0.00 \\ 0.00 & 2.32 & 0.00 \\ 0.00 & 0.00 & 2.32 \end{bmatrix} \times 10^{-3}.$$

This is exactly the same as the \overline{D}^e of the domain with $R^s = 2.45\mu\text{m}$, computed previously.

We set $\kappa = 10^{-5}\text{m/s}$ and show that the ODE model is less accurate for the domain with $R^s = 4.9\mu\text{m}$ (Fig. 3.7(b)) compared to the domain with $R^s = 2.45\mu\text{m}$ (Fig. 3.7(a)). The gradient sequences are PGSE, with $\delta = \Delta = 40\text{ms}$ and $\delta = \Delta = 80\text{ms}$.

This can be explained by the fact that at $R^s = 4.9\mu\text{m}$, the diffusion distance for water molecules inside the spheres is not yet zero in the range of times considered. To illustrate this argument, we computed the time-dependent ADC_0 for each compartment by setting $\kappa = 0\text{m/s}$ and solving the Bloch-Torrey PDE for many PGSE sequences, with $\delta = 1\text{ms}$, and Δ varying from 10ms to 160ms. We show the ADC_0 as a function of Δ for water inside Ω^e (Fig. 3.7(c)). The ADC_0 approaches the steady-state value of $2.32 \times 10^{-3}\text{mm}^2/\text{s}$ quickly for both sphere radii. On the other hand, if we consider water inside the sphere, Ω^s , we see in Fig. 3.7(d) that the ADC_0 for $R^s = 2.45\mu\text{m}$ is much closer to its theoretical steady-state value of $\overline{D}^s = 0$ than that for $R^s = 4.9\mu\text{m}$, on $[0\text{ms}, 160\text{ms}]$, the range of diffusion times considered. This means that when $R^s = 4.9\mu\text{m}$, the average diffusion distance for water molecules inside the sphere still varies a lot as a function of time and Ω^s cannot be considered a Gaussian diffusion compartment.

3.2. Numerical study

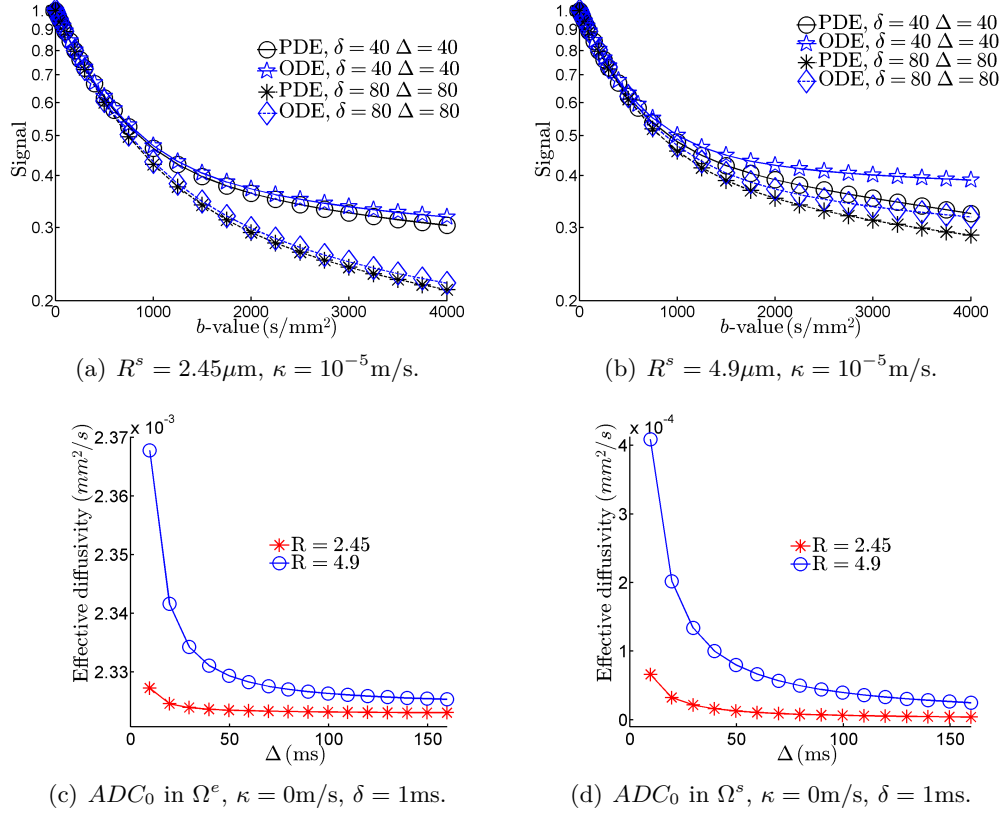


Figure 3.7: Two periodic lattices of spheres, with $R^s = 2.45 \mu m$ and $R^s = 4.9 \mu m$, $\kappa = 10^{-5} m/s$. $S_{PDE}(b)$ and $S_{ODE}(b)$ for the PGSE sequence with $\delta = \Delta = 40 ms$ and $\delta = \Delta = 80 ms$ are shown in (a) and (b). Setting $\kappa = 0 m/s$, we also computed the ADC_0 corresponding to many PGSE sequences, with $\delta = 1 ms$, and Δ varying from 10ms to 160ms, for the extra-cellular space Ω^e (c) and for the intra-cellular space Ω^s (d). One can see that while the extra-cellular space Ω^e can be considered a Gaussian diffusion compartment for both sphere sizes (look at the scale of the y-axis), the sphere compartment Ω^s cannot be considered a Gaussian diffusion compartment when $R = 4.9 \mu m$ because the ADC_0 is changing a lot with diffusion time on $[0ms, 160ms]$.

3.2.2 Simulation on complex geometries

3.2.2.1 Domain containing spheres of various sizes

We constructed the domain shown in Fig. 3.8(a) containing 76 spherical cells with a range of radii between $0.6 - 2.55 \mu m$. The spheres were put randomly in the computational domain is $C = [-5 \mu m, 5 \mu m]^3$ in a way to ensure no overlap. Formally, one has 76 different spherical compartments, each with its volume fraction and surface-to-volume ratio. However, it is convenient to combine 76 spheres to form a single compartment Ω^s . The extra-cellular space forms the second compartment Ω^e . The corresponding volume fractions are $v^s = 0.65$ and $v^e = 0.35$. The surface

Chapter 3. Numerical study of two macroscopic dMRI signal models

to volume ratio is $|\Gamma^{se}|/|\Omega^s| = 1.85\mu\text{m}^{-1}$. Here we assume that $|\Gamma^{se}|/|\Omega^s|$ gives a good approximation of the average surface-to-volume ratios of all the 76 spheres. The approximation is exact when all the spheres have the same radii. In the domain shown in Fig. 3.8(a), each sphere is compact, effective diffusion tensor for each of them can be considered as 0 from Eq. (2.29), and this consideration holds for their joint intra-cellular compartment. We also computed \overline{D}^e by solving Eq. (2.24):

$$\overline{D}^e = \begin{bmatrix} 2.20 & 0.00 & 0.00 \\ 0.00 & 2.25 & 0.00 \\ 0.00 & 0.00 & 2.24 \end{bmatrix} \times 10^{-3} \text{mm}^2/\text{s}.$$

We see in Fig. 3.8(b) that using two-compartment ODE model still gives a good approximation to the signal of the full PDE if we use the average surface-to-volume ratio of the 76 spheres.

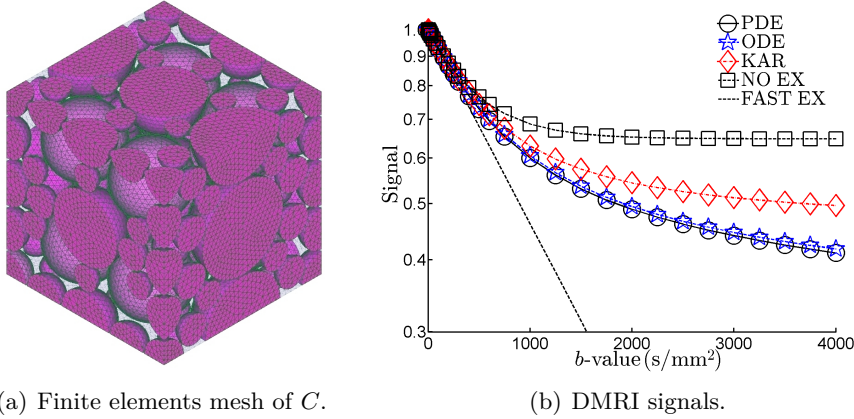


Figure 3.8: (a) The computational domain $C = [-5\mu\text{m}, 5\mu\text{m}]^3$ contains 76 spheres with radii $0.6 - 2.55\mu\text{m}$. The volume fractions of the spheres and of the extra-cellular space are $v^s = 0.65$ and $v^e = 0.35$, respectively. The membrane permeability is set to $\kappa = 10^{-5}\text{m/s}$. (b) The dMRI signals: $S_{PDE}(b)$, $S_{ODE}(b)$, $S_{KAR}(b)$, $S_{NOEX}(b)$, $S_{FASTEX}(b)$. The gradient sequence is PGSE with $\delta = \Delta = 25\text{ms}$.

3.2.2.2 Domain containing parallel cylinders

In order to test whether the ODE model works properly for anisotropic diffusion, we construct a domain containing slanted cylinders that all lie parallel to the $x - y$ -plane, make an angle $\pi/3$ with the x -axis, and have the radius $R^c = 2.35\mu\text{m}$ (Fig. 3.9(a)). The computational domain is $C = [-2.89, 2.89] \times [-2.5, 2.5] \times [-5, 5]\mu\text{m}^3$. This domain is split into two compartments: the compartment Ω^c of all the cylinders (with $v^c = 0.69$), and the extra-cellular space Ω^e (with $v^e = 0.31$). The volumes and surface areas are $|\Omega^e| = 91\mu\text{m}^3$, $|\Omega^c| = 198\mu\text{m}^3$, and $|\Gamma^{ce}| = 170\mu\text{m}^2$. We

3.2. Numerical study

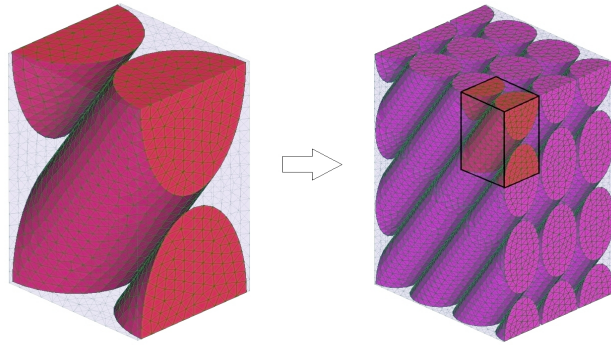
computed from Eq. (2.30):

$$\overline{D}^c = \begin{bmatrix} 0.75 & 0.00 & 1.30 \\ 0.00 & 0.00 & 0.00 \\ 1.30 & 0.00 & 2.25 \end{bmatrix} \times 10^{-3} \text{mm}^2/\text{s},$$

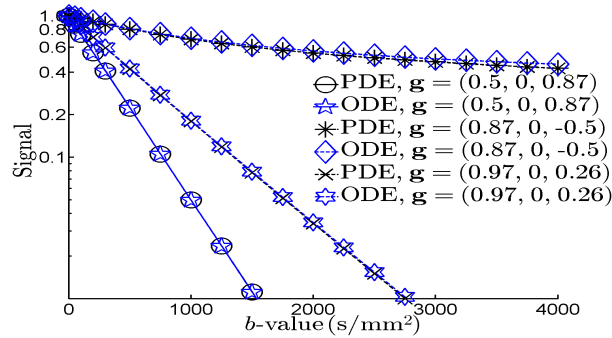
and from Eq. (2.24):

$$\overline{D}^e = \begin{bmatrix} 1.88 & 0.00 & 0.65 \\ 0.00 & 2.52 & 0.00 \\ 0.65 & 0.00 & 2.63 \end{bmatrix} \times 10^{-3} \text{mm}^2/\text{s}.$$

We set $\kappa = 10^{-5} \text{m/s}$ and $\delta = \Delta = 80 \text{ms}$ for the PGSE sequence. Three gradient directions (parallel, perpendicular and 45 degrees from axes of the cylinders) are considered. We show in Fig. 3.9(b) that $S_{PDE}(b)$ and $S_{ODE}(b)$ are close in all three gradient directions.



(a) Left: mesh of C . Right: periodic extension.



(b) DMRI signals.

Figure 3.9: In (a), left: finite elements mesh of $C = [-2.89, 2.89] \times [-2.5, 2.5] \times [-5, 5] \mu\text{m}^3$, right: when periodically extended, the cylinders are infinitely long. In (b): $S_{PDE}(b)$ and $S_{ODE}(b)$ when $\kappa = 10^{-5} \text{m/s}$. The gradient directions are $\mathbf{g}_1 = (0.5, 0, 0.87)$ and $\mathbf{g}_2 = (0.87, 0, -0.5)$, correspondingly parallel and perpendicular to the axis of cylinders, and $\mathbf{g}_3 = (0.97, 0, 0.26)$, lying in the middle of \mathbf{g}_1 and \mathbf{g}_2 . The sequence is PGSE, with $\delta = \Delta = 80 \text{ms}$.

3.2.2.3 Domain containing cylinders with thick membrane layer

Next, we constructed a domain with a cell membrane compartment (Fig. 3.10(a)). The computational domain $C = [-2.75, 2.75]^2 \times [-0.5, 0.5]\mu\text{m}^3$ contains a cylinder ($R^c = 2.0\mu\text{m}$) with a thick membrane (thickness $h = 0.45\mu\text{m}$) outside it. We consider C to be made up of three compartments: the extra-cellular space Ω^e ($|\Omega^e| = 11.5\mu\text{m}^3$), the membrane compartment Ω^m ($|\Omega^m| = 6.3\mu\text{m}^3$), and the cylinder compartment Ω^c ($|\Omega^c| = 12.5\mu\text{m}^3$), with the corresponding interfaces Γ^{em} ($|\Gamma^{em}| = 15.4\mu\text{m}^2$) and Γ^{mc} ($|\Gamma^{mc}| = 12.5\mu\text{m}^2$) ($|\Gamma^{ec}| = 0$, obviously). We know \overline{D}^c and \overline{D}^m from Eqs. (2.30, 2.29). We also computed

$$\overline{D}^e = \begin{bmatrix} 1.70 & 0.00 & 0.00 \\ 0.00 & 1.70 & 0.00 \\ 0.00 & 0.00 & 3.00 \end{bmatrix} \times 10^{-3} \text{mm}^2/\text{s}.$$

We would like to know whether the membrane compartment can be detected in the dMRI signal. For this purpose, we construct a second computational domain C , with two compartments: a combined cylinder and membrane compartment, Ω^{m+c} , with infinite permeability between Ω^m and Ω^c ($|\Omega^{m+c}| = 18.8\mu\text{m}^3$), and the same extra-cellular compartment Ω^e as for the three-compartment domain. In the two-compartment domain, there is only one surface $\Gamma^{e(m+c)}$ ($|\Gamma^{e(m+c)}| = 15.4\mu\text{m}^2$).

For permeability $\kappa^{mc} = 10^{-5}\text{m/s}$, Fig. 3.10(b) shows $S_{PDE}(b)$ and $S_{ODE}(b)$ in the gradient direction perpendicular with the cylinder axis for both domains. $S_{PDE}(b)$ and $S_{ODE}(b)$ are close to each other in both cases. The difference between the signals from the two domains can be seen in Fig. 3.10(b) but it is not clear whether the difference is large enough to be useful in detecting the membrane compartment in experimental settings.

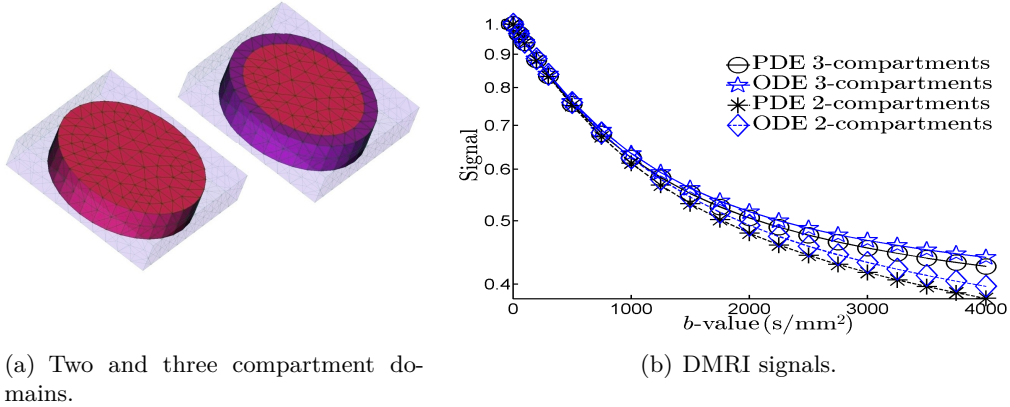


Figure 3.10: $C = [-2.75, 2.75]^2 \times [-0.5, 0.5]\mu\text{m}^3$, cylinder radius $R^c = 2.0\mu\text{m}$, membrane thickness $h = 0.45\mu\text{m}$. In (a), finite elements meshes, left: two-compartment domain (Ω^e and Ω^{c+m}), right: three-compartment domain (Ω^e and Ω^c and Ω^m). In (b). $S_{PDE}(b)$ and $S_{ODE}(b)$ of the three-compartment domain and the two-compartment domain, with $\kappa = 10^{-5}\text{m/s}$, subject to PGSE $\delta = \Delta = 80\text{ms}$, in the gradient direction $g = (1, 0, 0)$, perpendicular with the axis of cylinder.

3.2. Numerical study

3.2.2.4 Domain containing cylinders of different orientations and spheres

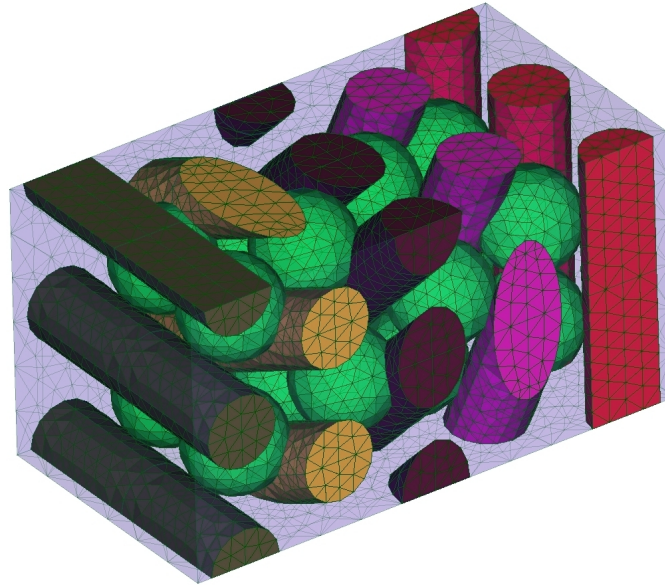
Finally, we constructed a domain of 5 layers of cylinders lying parallel to the $x - y$ plane and 4 layers of spherical cells all embedded in the extra-cellular space, see Fig 3.11(a). The five layers of cylindrical cells contain parallel cylinders that are oriented at 0, 26.5, 45, 63.5 and 90 degrees, respectively, from the x -axis (cylinder radius $R^c = 1.0\mu\text{m}$). The 4 layers of 16 spherical cells (sphere radius $R^s = 1.375\mu\text{m}$) are inserted between the 5 layers of cylindrical cells. When the spheres overlapped with cylinders, the latter have been (slightly) deformed. This deformation allowed to reduce the volume fraction of the extra-cellular space. Note also that some spheres and cylinders have joint interfaces. Although the cylinders were slightly deformed, we could still use Eq. (2.30) for computing the effective diffusion tensor.

In summary, we consider this domain to have 7 compartments: the extra-cellular space (Ω^e), the compartment of the 4 layers of 16 spherical cells (Ω^s), and 5 compartments consisting of the cylinders with the same orientation ($\Omega^{c_1}, \dots, \Omega^{c_5}$). In each layer of cylinders, the orientations of the cylinders are the same. One can note that the compartment combination for spheres can be done similarly to previous examples because of their compact shapes. On the other hand, despite of having very similar shapes and surface-over-volume ratios, the effective diffusion tensors of 5 layers of cylinders are not the same. So their compartment combination is not applicable, and one need to consider each layer separately.

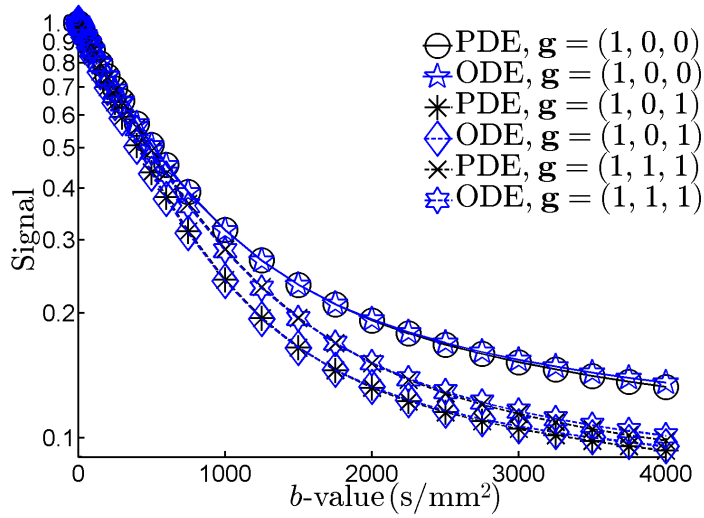
For the 7 compartments, the volumes are: $|\Omega^e| = 383\mu\text{m}^3$, $|\Omega^s| = 167\mu\text{m}^3$, $|\Omega^{c_1}| = 46\mu\text{m}^3$, $|\Omega^{c_2}| = 47\mu\text{m}^3$, $|\Omega^{c_3}| = 55\mu\text{m}^3$, $|\Omega^{c_4}| = 47\mu\text{m}^3$ and $|\Omega^{c_5}| = 46\mu\text{m}^3$. The surface areas are: $|\Gamma^{es}| = 291\mu\text{m}^2$, $|\Gamma^{ec_1}| = 93\mu\text{m}^2$, $|\Gamma^{ec_2}| = 85\mu\text{m}^2$, $|\Gamma^{ec_3}| = 98\mu\text{m}^2$, $|\Gamma^{ec_4}| = 85\mu\text{m}^2$, $|\Gamma^{ec_5}| = 93\mu\text{m}^2$, $|\Gamma^{sc_1}| = 0$, $|\Gamma^{sc_2}| = 21\mu\text{m}^2$, $|\Gamma^{sc_3}| = 37\mu\text{m}^2$, $|\Gamma^{sc_4}| = 21\mu\text{m}^2$, $|\Gamma^{sc_5}| = 0$. The cellular permeability for both cylinders and spheres is set to $\kappa = 10^{-5}\text{m/s}$. The computational domain is $C = [-3.75, 3.75] \times [-7.03, 7.03] \times [-3.75, 3.75]\mu\text{m}^3$. The computed effective extra-cellular diffusion tensor is:

$$\overline{D^e} = \begin{bmatrix} 2.29 & 0.00 & 0.11 \\ 0.00 & 2.05 & 0.00 \\ 0.11 & 0.00 & 2.29 \end{bmatrix} \times 10^{-3}\text{mm}^2/\text{s}.$$

We computed $S_{PDE}(b)$ and $S_{ODE}(b)$ in three gradient directions: $\mathbf{g}_1 = (1, 0, 0)$, $\mathbf{g}_2 = (1, 0, 1)$, and $\mathbf{g}_3 = (1, 1, 1)$, for the PGSE sequence with $\delta = \Delta = 40\text{ms}$. Figure 3.11(b) shows that the ODE and the PDE signals are almost indistinguishable.



(a) Finite elements mesh of C .



(b) DMRI signals

Figure 3.11: (a) Finite elements mesh of C containing 5 layers of cylinders and 4 layers of spheres. In each layer, the cylinders have the same orientation. (b) $S_{PDE}(b)$ and $S_{ODE}(b)$. The cell membrane permeability is $\kappa = 10^{-5}$ m/s. The gradient directions are $\mathbf{g}_1 = (1, 0, 0)$, $\mathbf{g}_2 = (1, 0, 1)$, and $\mathbf{g}_3 = (1, 1, 1)$. The pulse sequence is PGSE, with $\delta = \Delta = 40$ ms.

3.3 Discussion

We have shown by the numerical simulations that if the voxel is made up of spatial sub-domains that are separated from each other by low permeability membranes and if diffusion in the sub-domains are (close to) Gaussian (i.e., the condition of good equilibration in each compartment is satisfied), then the macroscopic ODE model of the dMRI signal (and the Kärger model, if the gradient profile is narrow pulse) is a good approximation to the microscopic Bloch-Torrey PDE model. However, for a generic voxel, spatial variations within the diffusion compartments are expected on the length scale of the voxel. For example, we would expect that the effective diffusion tensor of the tortuous extra-cellular space would not, in general, be constant over the entire voxel, exhibiting spatial variations on smaller length scales. However, the insight gained by the ODE model can still be important. In [113] the ODE model was derived by explicitly taking into account the discontinuity in the magnetization across the cell membranes and using different expansions of the PDE solution in each compartment, matching them via the interface conditions. A way to formulate better macroscopic models for “realistic” tissues is to account for the “smooth” spatial variations in the diffusivity within each compartment, for example, by expanding around a mean effective diffusivity as was done in [70]. However, this expansion should not be taken for the entire voxel because the magnetization is sharply varying in a large portion of the voxel, i.e., on the biological cell membranes.

3.4 Conclusions

A macroscopic ODE model governing the time evolution of the integrals of the water proton magnetization in compartments defined as spatial sub-domains of the imaging voxel was recently formulated from the microscopic heterogeneous domain Bloch-Torrey PDE. We conducted a numerical validation of this ODE model for complex geometries containing spheres and cylinders of various sizes and orientations. We illustrated by numerical simulations that this new ODE model was a good approximation to the dMRI signal of the full PDE model for general gradient pulse shapes when the diffusion in all the compartments is approximately Gaussian and the mutual exchange between them is slow. When the narrow gradient pulse assumption is not satisfied, the ODE model offers a much better approximation of the full PDE signal than the Kärger model. More work remains to be done to improve the macroscopic models to make them applicable to brain dMRI.

Parameters estimation using macroscopic dMRI signal models

In diffusion MRI, water motion inside a biological tissue is monitored in order to characterize the tissue microstructure at micrometer-order length scales. Varying gradients and diffusion times, one acquires the macroscopic signal which aggregates statistically averaged information about the domain at the millimeter scale. Inferring the microstructure from the macroscopic signal is a formidable inverse problem. In spite of considerable research over the last 50 years, this problem remains very poorly understood (see [3] and the bibliography in Chapter 1).

The complexity of brain tissue does not allow the extraction of the whole microstructure. In turn, one focuses on estimating some effective parameters of the tissue whose changes can afterwards be related to physiological or pathological modifications. Among such effective parameters, one often considers volume fractions of the intra-cellular and extra-cellular spaces (which may change during cell swelling), membrane permeability (which may characterize, to some extent, normal or abnormal functioning of cells), average size of cells, as well as effective diffusion coefficients. In this chapter, we consider the parameters estimation problem by using macroscopic dMRI signal models.

Instead of experimental data we will use synthetically generated data. This will allow us to clarify some relations between the microstructure and the dMRI signals, and to check the influence of various parameters on the stability and the quality of the parameters estimation.

In the first step, we choose a model microstructure and produce synthetic dMRI signals by solving numerically the microscopic Bloch-Torrey equation on this domain at a set of b-values. This signal is considered as an input to the parameters estimation problem. In the second step, we fit this signal at the set of b-values using the macroscopic Kärger and the ODE models to extract model parameters. If there are P compartments, the full set of macroscopic model parameters are:

- the volume fractions of the compartments: $\{v_m\}_{1 \leq m \leq P}$;
- the effective diffusion coefficients in a prescribed gradient direction \mathbf{g} that we define as: $\{D_{\mathbf{g}}^m = \mathbf{u}_{\mathbf{g}}^T \bar{D}^m \mathbf{u}_{\mathbf{g}}\}_{1 \leq m \leq P}$;
- the residence time for molecules in the compartment l before exchanging to

the compartment m :

$$\{\tau^{ml}\}_{1 \leq l, m \leq P, l \neq m}, \text{ where } \tau^{ml} \equiv \frac{1}{\kappa} \frac{|\Omega^l|}{|\Gamma^{ml}|};$$

We label this full set of model parameters by:

$$\mathcal{U}^{full} \equiv \left\{ v^m, D_{\mathbf{g}}^m, \tau^{lm} \right\}_{1 \leq l, m \leq P, l \neq m}.$$

In practice, we solved the least squares problems to be explained below for the parameters $\frac{1}{\tau^{lm}}$ instead of τ^{lm} , but for the ease of notation, we will list τ^{lm} as the searched-for parameter, instead of, more correctly, its reciprocal.

The total number of parameters in \mathcal{U}^{full} is

$$\mathcal{Z}^{full} \equiv |\mathcal{U}^{full}| = 2P + P(P-1)/2 - 1.$$

For example:

$$P = 2 \rightarrow \mathcal{Z}^{full} = 4,$$

$$P = 3 \rightarrow \mathcal{Z}^{full} = 8,$$

$$P = 4 \rightarrow \mathcal{Z}^{full} = 13.$$

If one needs the full effective diffusion tensors $\overline{D}^m, m = 1, \dots, P$ instead of just the effective diffusion coefficients in a given direction, $D_{\mathbf{g}}^m, m = 1, \dots, P$, then there would be an additional $5P$ parameters.

Because of the high number of model parameters as the number of compartments increases, for some problems, we will consider the parameters estimation problem under the simplifying assumption that a subset of \mathcal{U}^{full} is known. In this case, we will specify the subset of parameters to be estimated, \mathcal{U} , and the set of parameters whose values will be set to known values: \mathcal{U}^{known} . Together, they make the full set of macroscopic model parameters:

$$\mathcal{U}^{full} = \mathcal{U}^{known} \cup \mathcal{U}.$$

For the set of parameters to be estimated, \mathcal{U} , to define the parameter estimation problem, we denote the ODE signal by

$$S_{ODE}(b, \mathcal{U}^{known}, \mathcal{U}),$$

and the Kärger signal by

$$S_{KAR}(b, \mathcal{U}^{known}, \mathcal{U}).$$

In the following, we will suppose that the dMRI signal is “exactly” the output of the Bloch-Torrey PDE: $S_{PDE}(b)$, and the macroscopic parameters of the heterogeneous domain of the PDE model to be the “true” ones, labelled $\mathcal{U}_{true}^{full}$.

Even if we use the true parameters, there will be modeling errors associated with approximating $S_{PDE}(b)$ by $S_{ODE}(b_k, \mathcal{U}_{true}^{full}, \emptyset)$ or $S_{KAR}(b_k, \mathcal{U}_{true}^{full}, \emptyset)$. We denote the

4.1. The least squares problem

relative difference between the signals of the PDE model and the ODE and Kärger models using the true macroscopic parameters by:

$$R_{ODE}^{mod} \equiv \sqrt{\frac{1}{n_b} \sum_{k=1}^{n_b} \left| \frac{S_{PDE}(b_k) - S_{ODE}(b_k, \mathcal{U}_{true}^{full}, \emptyset)}{S_{PDE}(b_k)} \right|^2}, \quad (4.1)$$

and

$$R_{KAR}^{mod} \equiv \sqrt{\frac{1}{n_b} \sum_{k=1}^{n_b} \left| \frac{S_{PDE}(b_k) - S_{KAR}(b_k, \mathcal{U}_{true}^{full}, \emptyset)}{S_{PDE}(b_k)} \right|^2}, \quad (4.2)$$

where n_b is the number of b -values. The above expressions can be considered residuals of the functionals.

In addition, we assume that there will be experimental noise:

$$(S_{PDE})^{noi}(b) = S_{PDE}(b) + \mathcal{N}(b). \quad (4.3)$$

For simplicity we will only consider Gaussian noise. More precisely, for each b -value, we add directly a random Gaussian variable with mean 0 and standard deviation σ :

$$\mathcal{N}(b) = \mathcal{N}_b(0, \sigma^2). \quad (4.4)$$

4.1 The least squares problem

The least squares problems we solve are the following:

$$\min_{\mathcal{U}} \sum_{k=1}^{n_b} \left| \frac{S_{PDE}(b_k) + \mathcal{N}(b_k) - S_{ODE}(b_k, \mathcal{U}^{known}, \mathcal{U})}{S_{PDE}(b_k) + \mathcal{N}(b_k)} \right|^2 \quad (4.5)$$

or

$$\min_{\mathcal{U}} \sum_{k=1}^{n_b} \left| \frac{S_{PDE}(b_k) + \mathcal{N}(b_k) - S_{KAR}(b_k, \mathcal{U}^{known}, \mathcal{U})}{S_{PDE}(b_k) + \mathcal{N}(b_k)} \right|^2. \quad (4.6)$$

Here one aims to minimize the *relative* difference between numerical points and fitting function, instead of the *absolute* difference. This choice allows one to “equilibrate” contributions from large signals at small b -values and from small signal at large b -values. Other functionals can also be considered.

Two inherent constraints on the model parameters are already given in Eq. (2.20) and Eq. (2.12). Physical arguments imply the other constraints:

$$\begin{aligned} \frac{\tau^{lm}}{\tau^{ml}} &= \frac{v^m}{v^l}, \\ \sum_{l=1}^P v^l &= 1, \\ 0 < D_{\mathbf{g}}^m &\leq D^0, \quad \forall \|\mathbf{g}\| = 1, \quad \text{if } \Omega^m \text{ is not compact,} \\ \overline{D}^m &= 0, \quad \text{if } \Omega^m \text{ is compact,} \\ 0 &\leq v^m \leq 1, \\ 0 &\leq \tau^{lm}. \end{aligned} \quad (4.7)$$

We set the following limits on the data in order to solve the parameter estimation problem:

$$\begin{aligned} 0 < b_k &\leq 4000(\text{s}/\text{mm}^2), \\ 0.1 < S_{PDE}(b_k), \end{aligned}$$

for all k . We will use the notation

$$\mathcal{U}_{ODE}^{min}$$

and

$$\mathcal{U}_{KAR}^{min}$$

for the solution of the minimalization problems in Eq. (4.5) and Eq. (4.6), respectively.

We denote the residuals of the minimalization problems for a parameter set \mathcal{U} by

$$R_{ODE}(\mathcal{U}) \equiv \sqrt{\frac{1}{n_b} \sum_{k=1}^{n_b} \left| \frac{S_{PDE}(b_k) + \mathcal{N}(b_k) - S_{ODE}(b_k, \mathcal{U}^{known}, \mathcal{U})}{S_{PDE}(b_k) + \mathcal{N}(b_k)} \right|^2} \quad (4.8)$$

and

$$R_{KAR}(\mathcal{U}) \equiv \sqrt{\frac{1}{n_b} \sum_{k=1}^{n_b} \left| \frac{S_{PDE}(b_k) + \mathcal{N}(b_k) - S_{KAR}(b_k, \mathcal{U}^{known}, \mathcal{U})}{S_{PDE}(b_k) + \mathcal{N}(b_k)} \right|^2}. \quad (4.9)$$

The residuals of the least squares solutions will therefore be $R_{ODE}(\mathcal{U}_{ODE}^{min})$ and $R_{KAR}(\mathcal{U}_{ODE}^{min})$.

In summary, we use the following procedure to solve the least square problem:

Algorithm 1 Algorithm of parameter estimations using macroscopic models

- 1: Solve the Bloch-Torrey equation Eq. (2.1) with interface condition in Eqs. (2.2, 2.3) and boundary conditions (2.5, 2.6), and get the signal attenuation $S_{PDE}(b_k)$ at $b = b_1, \dots, b_{n_b}$.
 - 2: Solve the least squares problems (4.5) and (4.6) with constraints (4.7) (and additional constraints if exist); we used the Matlab function *lsqnonlin*, in which both the residual and the estimated parameters tolerances were set at 10^{-12} .
 - 3: Solve the system of ODEs to obtain $S_{ODE}(b_k, \mathcal{U}^{known}, \mathcal{U})$ for each b_k ; in Matlab we set the tolerance for the home built function *ode45* to 10^{-8} .
-

Unless otherwise noted, the default number of b-values used is $n_b = 20$, with

$$\begin{aligned} b = [0, 50, 100, 200, 300, 500, 750, 1000, 1250, 1500, 1750, \\ 2000, 2250, 2500, 2750, 3000, 3250, 3500, 3750, 4000] \times \text{s}/\text{mm}^2. \end{aligned} \quad (4.10)$$

4.2. Domain containing periodic lattice of spheres of the same size

4.2 Domain containing periodic lattice of spheres of the same size

First we consider a simple domain of a periodic lattice of spheres of the same size (see Fig. 3.2(a) for the computational domain C). There are two compartments: the extra-cellular compartment Ω^e and the spherical cells compartment Ω^s . The cell radius is R^s , the inter-cell distance is L . The cellular volume fraction is v^s . In this section, we consider the signal attenuation without noise, i.e, $\mathcal{N}(b_k) = 0, k = 1, \dots, n_b$ in Eq. (4.5) and Eq. (4.6).

4.2.1 Least squares problem on a 3-parameters set

We solve the least squares problems in Eq. (4.5) and Eq. (4.6) for the following set of three macroscopic model parameters:

$$\mathcal{U} = \{v^s, D_{\mathbf{g}}^e, \tau^{es}\},$$

where $\tau^{es} \equiv \frac{|\Omega^s|}{\kappa|\Gamma^{es}|}$. Because the sphere is compact, we consider the effective long-time diffusion coefficient of Ω^s to be $\bar{D}^s = 0$, which means:

$$\mathcal{U}^{known} = \{D_{\mathbf{g}}^s = 0\}.$$

The constraints from Eq. (4.7) are:

$$\begin{aligned} \frac{\tau^{es}}{\tau^{se}} &= \frac{v^s}{v^e}, \\ v^e + v^s &= 1, \\ 0 < D_{\mathbf{g}}^e &\leq D^0, \\ D_{\mathbf{g}}^s &= 0, \text{ because } \Omega^s \text{ is compact,} \\ 0 \leq v^m &\leq 1, \\ 0 \leq \tau^{es}. \end{aligned} \tag{4.11}$$

The signal data at 20 b-value from 0 to 4000s/mm² (listed previously) are obtained by solving the Bloch-Torrey PDE for the PGSE sequence: $\delta = \Delta = 40\text{ms}$ in gradient direction $\mathbf{g} = [1, 0, 0]$. We also note that diffusion on this domain could be considered as isotropic. The cell radius is $R^s = 2.45\mu\text{m}$, the inter-cell distance is $L = 5\mu\text{m}$, which corresponds to the cell volume fraction $v^s = 0.49$. The intrinsic diffusion coefficient is $D^0 = 3 \times 10^{-3}\text{mm}^2/\text{s}$. An intermediate membrane permeability of $\kappa = 10^{-5}\text{m/s}$ was chosen. The true model parameters are:

$$\mathcal{U}_{true} = \left\{ v^s = 0.49, D_{\mathbf{g}}^e = 2.32 \times 10^{-3}\text{mm}^2/\text{s}, \tau^{es} = 81\text{ms} \right\}.$$

The initial guess of the least squares problem is:

$$\mathcal{U}^0 = \left\{ c_v, \frac{D^0}{2}, c_{\tau} \frac{\tau_{true}^{es} \tau_{true}^{se}}{2(\tau_{true}^{es} + \tau_{true}^{se})} = 1.2 \times 10^{-5} c_{\tau} \right\},$$

where c_v is a random number (of a uniform distribution) between 0 and 1, c_τ is between 0.1 and 10. For this domain, we did not see any difference of parameter estimation results when c_v and c_τ are varied.

We present \mathcal{U}_{ODE}^{min} and \mathcal{U}_{KAR}^{min} in Table 4.1. Because $\delta = \Delta = 40\text{ms}$ does not satisfy the narrow pulse assumption, the Kärger model is not a good approximation of the full PDE model, whereas the ODE model is a better approximation. The modeling errors are $R_{ODE}^{mod} = 2.6\%$ and $R_{KAR}^{mod} = 14.0\%$, respectively. We see \mathcal{U}_{ODE}^{min} is close to \mathcal{U}_{true} for all three estimated parameters, whereas \mathcal{U}_{KAR}^{min} is not a good approximation of \mathcal{U}_{true} . In particular, the $S_{KAR}(b, \mathcal{U}^{known}, \mathcal{U})$ and the $S_{ODE}(b, \mathcal{U}^{known}, \mathcal{U})$ have a larger ADK_0 than $S_{PDE}(b)$ (see Fig. 3.2(b)), leading to the under-estimation of τ^{es} : $\tau_{KAR}^{es} = 33\text{ms} < \tau_{ODE}^{es} = 70\text{ms} < \tau_{true}^{es} = 81\text{ms}$. The residuals of the least squares solutions are $R_{ODE}(\mathcal{U}_{ODE}^{min}) = 0.02\%$ and $R_{KAR}(\mathcal{U}_{KAR}^{min}) = 0.2\%$, respectively.

Then we set $\kappa = 5 \times 10^{-5}\text{m/s}$ and show the results in the second row of Table 4.1. We see the modeling errors have increased significantly in this higher permeability case: $R_{ODE}^{mod} = 11.7\%$ and $R_{KAR}^{mod} = 41.0\%$. However, the results of parameter estimation \mathcal{U}_{ODE}^{min} are still good in comparison to \mathcal{U}_{true} , especially for v^s and τ^{es} . But from the results of \mathcal{U}_{KAR}^{min} , one can see that parameter estimation using Kärger model does not work well.

κ - PGSE	Parameter	\mathcal{U}^{true}	\mathcal{U}_{ODE}^{min}	\mathcal{U}_{KAR}^{min}
$\kappa = 1 \times 10^{-5}\text{m/s}$ $\delta = 40\text{ms}$ $\Delta = 40\text{ms}$	v^s	0.49	0.50	0.56
	τ^{es} (ms)	81	70	33
	$D_{\mathbf{g}}^e$ ($\times 10^{-3}\text{mm}^2/\text{s}$)	2.32	2.38	3.00
	$R(\mathcal{U}^{min})$		0.1%	0.5%
	R^{mod}		2.6%	14.0%
$\kappa = 5 \times 10^{-5}\text{m/s}$ $\delta = 40\text{ms}$ $\Delta = 40\text{ms}$	v^s	0.49	0.47	0.57
	τ^{es} (ms)	16	15	8
	$D_{\mathbf{g}}^e$ ($\times 10^{-3}\text{mm}^2/\text{s}$)	2.32	2.44	2.83
	$R(\mathcal{U}^{min})$		0.02%	0.3%
	R^{mod}		11.7%	41.0%

Table 4.1: Results of parameter estimations for the domain containing periodic lattice of spherical cells (Fig. 3.2(a)), $R^s = 2.45\mu\text{m}$, $L = 5\mu\text{m}$. PGSE sequence with $\delta = \Delta = 40\text{ms}$ in gradient direction $\mathbf{g} = [1, 0, 0]$ with $D^0 = 3 \times 10^{-3}\text{mm}^2/\text{s}$.

4.2.2 Contour plots of 2-parameters sets

Now we study the sensitivity of the solution of the least squares problems with respect to the various macroscopic model parameters. For this purpose, we use contour plots of $R_{ODE}(\mathcal{U})$ and $R_{KAR}(\mathcal{U})$ as we move in \mathcal{U} parameter space.

On the contour plots, we study two parameters at a time, leaving the remaining parameters at their known values. First we set

$$\mathcal{U} = \{v^s, D_{\mathbf{g}}^e\}, \quad \mathcal{U}^{known} = \{\tau^{es} = \tau_{true}^{es}\}, \quad (4.12)$$

4.2. Domain containing periodic lattice of spheres of the same size

where $\tau_{true}^{es} = 81\text{ms}$ and make plots of $R_{ODE}(\mathcal{U})$ and $R_{KAR}(\mathcal{U})$ in the first row of Fig. 4.1. Three specific points of interest on the contour plots are:

1. $\mathcal{U}_{true} = \{v^s = 0.49, D_{\mathbf{g}}^e = 2.32 \times 10^{-3}\text{mm}^2/\text{s}\};$
2. $\mathcal{U}_{ODE}^{min} = \{v^s = 0.47, D_{\mathbf{g}}^e = 2.23 \times 10^{-3}\text{mm}^2/\text{s}\};$
3. $\mathcal{U}_{KAR}^{min} = \{v^s = 0.40, D_{\mathbf{g}}^e = 1.85 \times 10^{-3}\text{mm}^2/\text{s}\}.$

We note the values of \mathcal{U}_{ODE}^{min} and \mathcal{U}_{KAR}^{min} above are slightly different from the values given in Table 4.1 because we set τ^{es} to a known value and only minimize on a 2-parameters set.

We see in Fig. 4.1(a) that \mathcal{U}_{ODE}^{min} is close to \mathcal{U}_{true} and in Fig. 4.1(b) that \mathcal{U}_{KAR}^{min} is far from \mathcal{U}_{true} .

Now we set

$$\mathcal{U} = \{v^s, \tau^{es}\}, \quad \mathcal{U}^{known} = \left\{ D_{\mathbf{g}}^e = \left(D_{\mathbf{g}}^e \right)_{true} \right\}, \quad (4.13)$$

where $\left(D_{\mathbf{g}}^e \right)_{true} = 2.3 \times 10^{-3}\text{mm}^2/\text{s}$ and make plots of $R_{ODE}(\mathcal{U})$ and $R_{KAR}(\mathcal{U})$ in the second row of Fig. 4.1. Three specific points of interest on the contour plots are:

1. $\mathcal{U}_{true} = \{v^s = 0.49, \tau^{es} = 81\text{ms}\};$
2. $\mathcal{U}_{ODE}^{min} = \{v^s = 0.48, \tau^{es} = 74\text{ms}\};$
3. $\mathcal{U}_{KAR}^{min} = \{v^s = 0.50, \tau^{es} = 41\text{ms}\}.$

We see in Fig. 4.1(c) that both estimated parameters of \mathcal{U}_{ODE}^{min} are close to \mathcal{U}_{true} and in Fig. 4.1(d) that the estimated τ^{es} of \mathcal{U}_{KAR}^{min} is far from \mathcal{U}_{true} .

Next we study the effect on the parameters estimation problem of various geometrical properties and signal acquisition choices. In detail, one by one, we will study the effect of permeability, diffusion time, range and number of b -values and cell size.

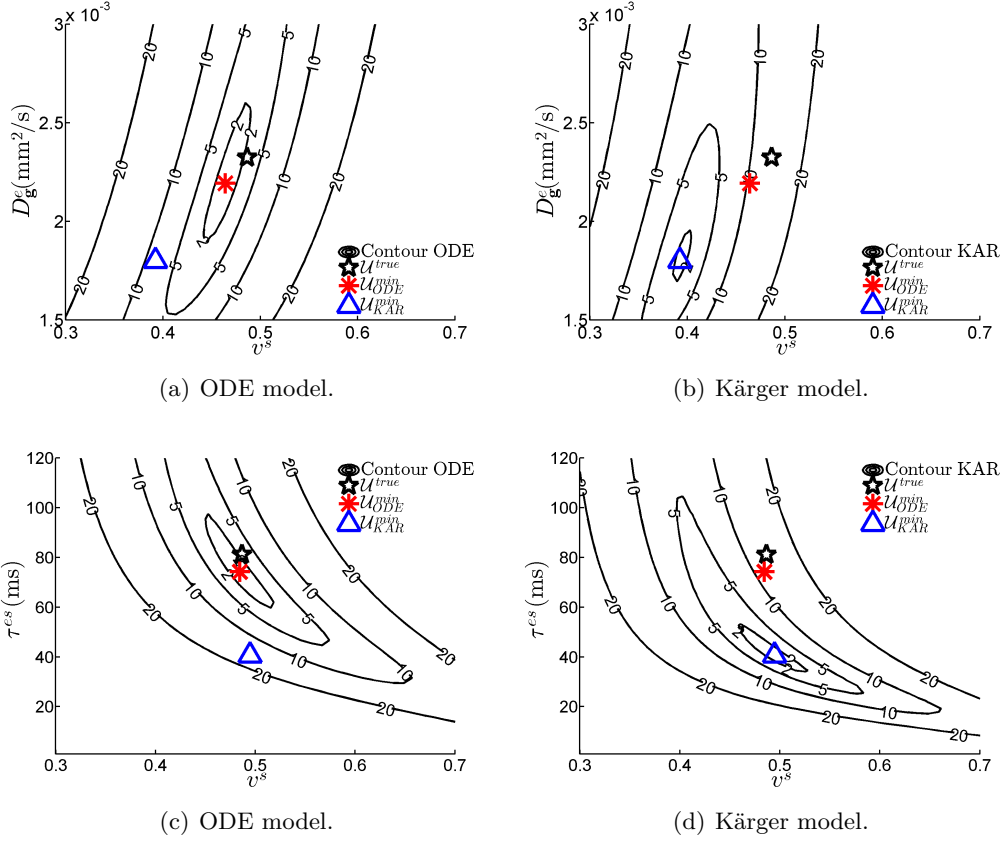


Figure 4.1: Contour plots of the residuals $R_{ODE}(\mathcal{U})$ and $R_{KAR}(\mathcal{U})$. First τ^{es} is fixed at the true value, while $\{v^s, D_g^e\}$ are estimated (a,b). Then D_g^e is fixed at the true value, while $\{v^s, \tau^{es}\}$ are estimated (c,d). PGSE with $\delta = \Delta = 40\text{ms}$, $n_b = 20$. R^{mod} : (a,c) 2.6%, (b,d) 14%; $R_{ODE}(\mathcal{U}_{ODE}^{min})$: (a,b) 0.5%, (c,d) 0.2%; $R_{KAR}(\mathcal{U}_{KAR}^{min})$: (a,b) 1.6%, (c,d) 0.6%.

4.2.3 Effect of permeability

First we study the effect of membrane permeability on the parameters estimation problem for the ODE model only.

We show in Fig. 4.2 the contour plots of \mathcal{U} for the two choices of 2-parameters sets defined in Eq. (4.12) and Eq. (4.13) for $\kappa = 1 \times 10^{-5}\text{m/s}$ and $\kappa = 5 \times 10^{-5}\text{m/s}$. With $\kappa = 5 \times 10^{-5}\text{m/s}$, specific points of interest on the contour plots for first 2-parameters set on Fig. 4.2(b) are:

- $\mathcal{U}_{true} = \{v^s = 0.49, D_g^e = 2.32 \times 10^{-3}\text{mm}^2/\text{s}\}$;
- $\mathcal{U}_{ODE}^{min} = \{0.41, 2.15 \times 10^{-3}\text{mm}^2/\text{s}\}$; $\mathcal{U}_{KAR}^{min} = \{0.30, 1.96 \times 10^{-3}\text{mm}^2/\text{s}\}$;

and for second 2-parameters set on Fig. 4.2(d) are:

4.2. Domain containing periodic lattice of spheres of the same size

- $\mathcal{U}_{true} = \{v^s = 0.49, \tau^{es} = 16\text{ms}\}$;
- $\mathcal{U}_{ODE}^{min} = \{0.44, 16\text{ms}\}$; $\mathcal{U}_{KAR}^{min} = \{0.44, 10\text{ms}\}$.

We can see that at higher permeability, the contours of unknowns tend to stretch, which can cause problems in solving the least squares problem in Eq. (4.5).

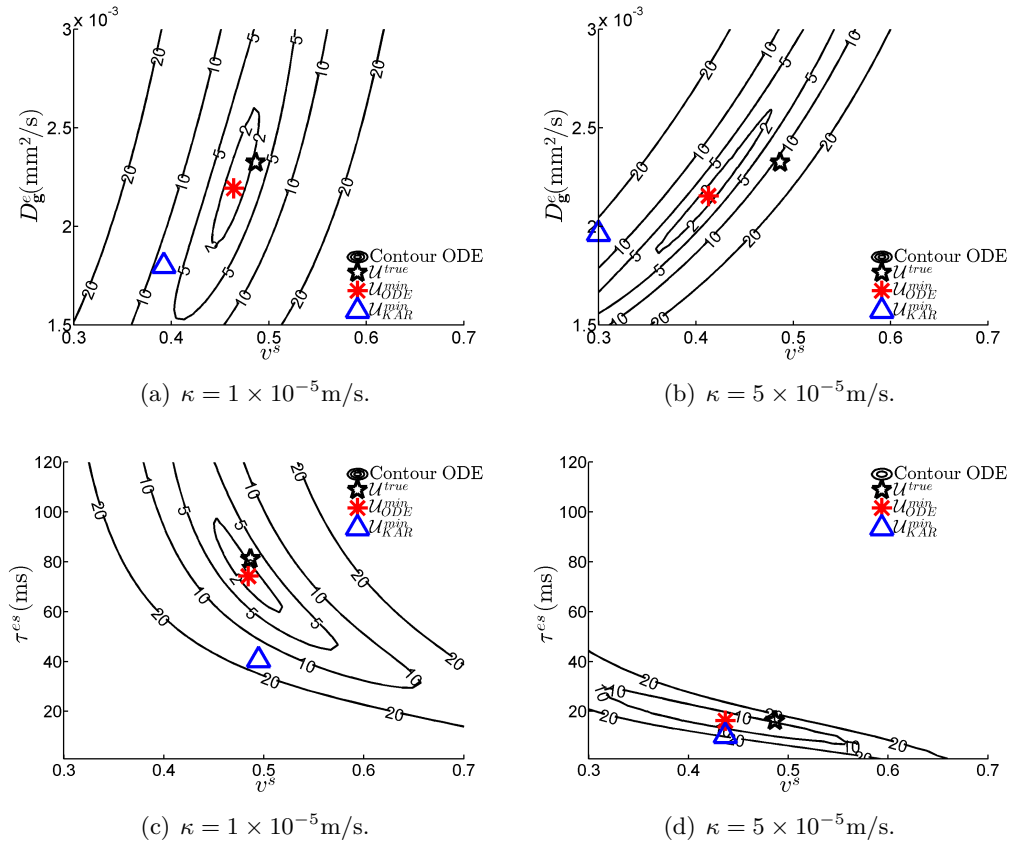


Figure 4.2: Contour plot of ODE model. Periodic lattice of spheres, cell radius $R^s = 2.45\mu\text{m}$, inter-cell distance $L = 5\mu\text{m}$. PGSE sequence: $\delta = 40\text{ms}$, $\Delta = 40\text{ms}$, $n_b = 20$. R^{mod} : (a,c) 2.6%, (b,d) 11.7%; $R_{ODE}(\mathcal{U}_{ODE}^{min})$: (a) 0.5%, (b) 0.4%, (c) 0.2% (d) 1.1%; $R_{KAR}(\mathcal{U}_{KAR}^{min})$: (a) 1.6%, (b) 6.1%, (c) 0.6% (d) 1.9%.

4.2.4 Effect of diffusion time

Now we study the effect of diffusion time on the parameters estimation problem for the ODE and Kärger models by changing times δ and Δ of the PGSE sequence. We use the following three sequences:

1. short diffusion time: $\delta = 10\text{ms}$, $\Delta = 10\text{ms}$;
2. long diffusion time in the narrow-pulse regime: $\delta = 10\text{ms}$, $\Delta = 70\text{ms}$;
3. long diffusion time beyond the narrow-pulse regime: $\delta = \Delta = 40\text{ms}$.

One can see in Fig. 4.3 the contour plots for the choice of the 2-parameters set defined in Eq. (4.12). At the short diffusion time $\delta = 10\text{ms}$, $\Delta = 10\text{ms}$, both \mathcal{U}_{ODE}^{min} and \mathcal{U}_{KAR}^{min} are far from \mathcal{U}_{true} with specific points for two 2-parameter sets:

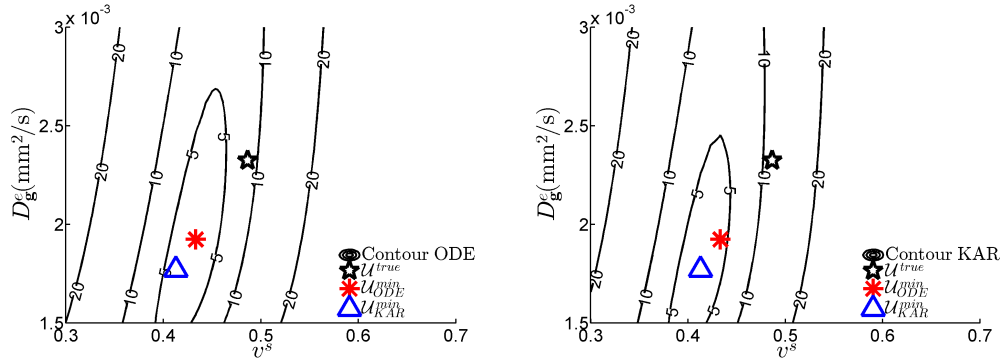
1. Figures 4.3(a) and 4.3(b): $\mathcal{U}_{true} = \{v^s = 0.49, D_g^e = 2.32 \times 10^{-3}\text{mm}^2/\text{s}\}$;
 $\mathcal{U}_{ODE}^{min} = \{0.43, 1.92 \times 10^{-3}\text{mm}^2/\text{s}\}$; $\mathcal{U}_{KAR}^{min} = \{0.41, 1.77 \times 10^{-3}\text{mm}^2/\text{s}\}$;
2. Figures 4.4(a) and 4.4(b): $\mathcal{U}_{true} = \{v^s = 0.49, \tau^{es} = 16\text{ms}\}$;
 $\mathcal{U}_{ODE}^{min} = \{0.52, 28\text{ms}\}$; $\mathcal{U}_{KAR}^{min} = \{0.52, 16\text{ms}\}$;

At the long diffusion time in the narrow-pulse regime $\delta = 10\text{ms}$, $\Delta = 70\text{ms}$, both \mathcal{U}_{ODE}^{min} and \mathcal{U}_{KAR}^{min} are close to \mathcal{U}_{true} for both two 2-parameter sets:

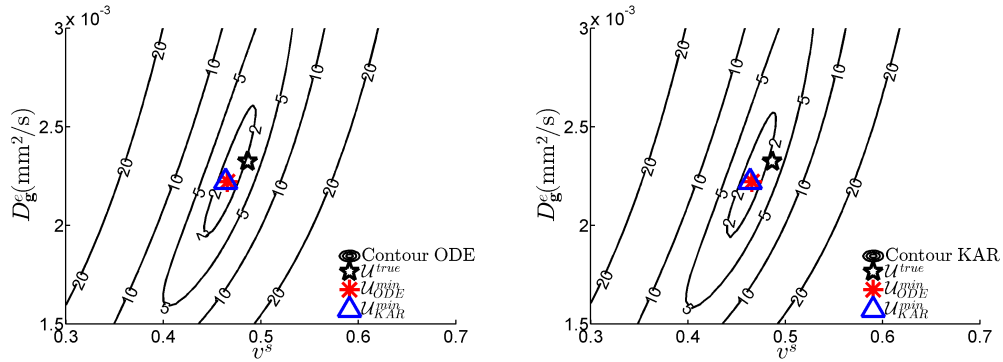
1. Figures 4.3(c) and 4.3(d): $\mathcal{U}_{true} = \{v^s = 0.49, D_g^e = 2.32 \times 10^{-3}\text{mm}^2/\text{s}\}$;
 $\mathcal{U}_{ODE}^{min} = \{0.47, 2.22 \times 10^{-3}\text{mm}^2/\text{s}\}$; $\mathcal{U}_{KAR}^{min} = \{0.46, 2.22 \times 10^{-3}\text{mm}^2/\text{s}\}$.
2. Figures 4.4(c) and 4.4(d): $\mathcal{U}_{true} = \{v^s = 0.49, \tau^{es} = 16\text{ms}\}$;
 $\mathcal{U}_{ODE}^{min} = \{0.48, 77\text{ms}\}$; $\mathcal{U}_{KAR}^{min} = \{0.48, 76\text{ms}\}$.

Finally, at the long diffusion time beyond the narrow-pulse regime $\delta = \Delta = 40\text{ms}$, as discussed above, \mathcal{U}_{ODE}^{min} is close to \mathcal{U}_{true} whereas \mathcal{U}_{KAR}^{min} is far from \mathcal{U}_{true} . One can see in Fig. 4.4 the contour plots for the choice of the 2-parameters set defined in Eq. (4.13) and the conclusions are similar.

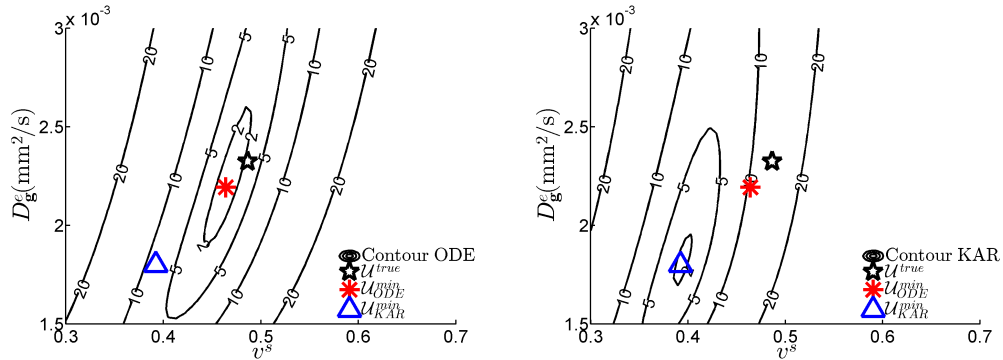
4.2. Domain containing periodic lattice of spheres of the same size



(a) ODE model, PGSE $\delta = 10\text{ms}$, $\Delta = 10\text{ms}$. (b) Kärger model, PGSE $\delta = 10\text{ms}$, $\Delta = 10\text{ms}$.



(c) ODE model, PGSE $\delta = 10\text{ms}$, $\Delta = 70\text{ms}$. (d) Kärger model, PGSE $\delta = 10\text{ms}$, $\Delta = 70\text{ms}$.



(e) ODE model, PGSE $\delta = 40\text{ms}$, $\Delta = 40\text{ms}$. (f) Kärger model, PGSE $\delta = 40\text{ms}$, $\Delta = 40\text{ms}$.

Figure 4.3: Contour plot of ODE model and Kärger model. Periodic lattice of spheres, cell radius $R^s = 2.45\mu\text{m}$, inter-cell distance $L = 5\mu\text{m}$. PGSE sequence, $n_b = 20$.

R^{mod} : (a) 8.4%, (b) 11.6%, (c) 2.4%, (d) 2.8%, (e) 2.6%, (f) 14%;

$R_{ODE}(U_{ODE}^{min})$: (a,b) 2.3%, (c,d) 0.3%, (e,f) 0.5%;

$R_{KAR}(U_{KAR}^{min})$: (a,b) 2.5%, (c,d) 0.3%, (e,f) 1.6%.

Chapter 4. Parameters estimation using macroscopic dMRI signal models

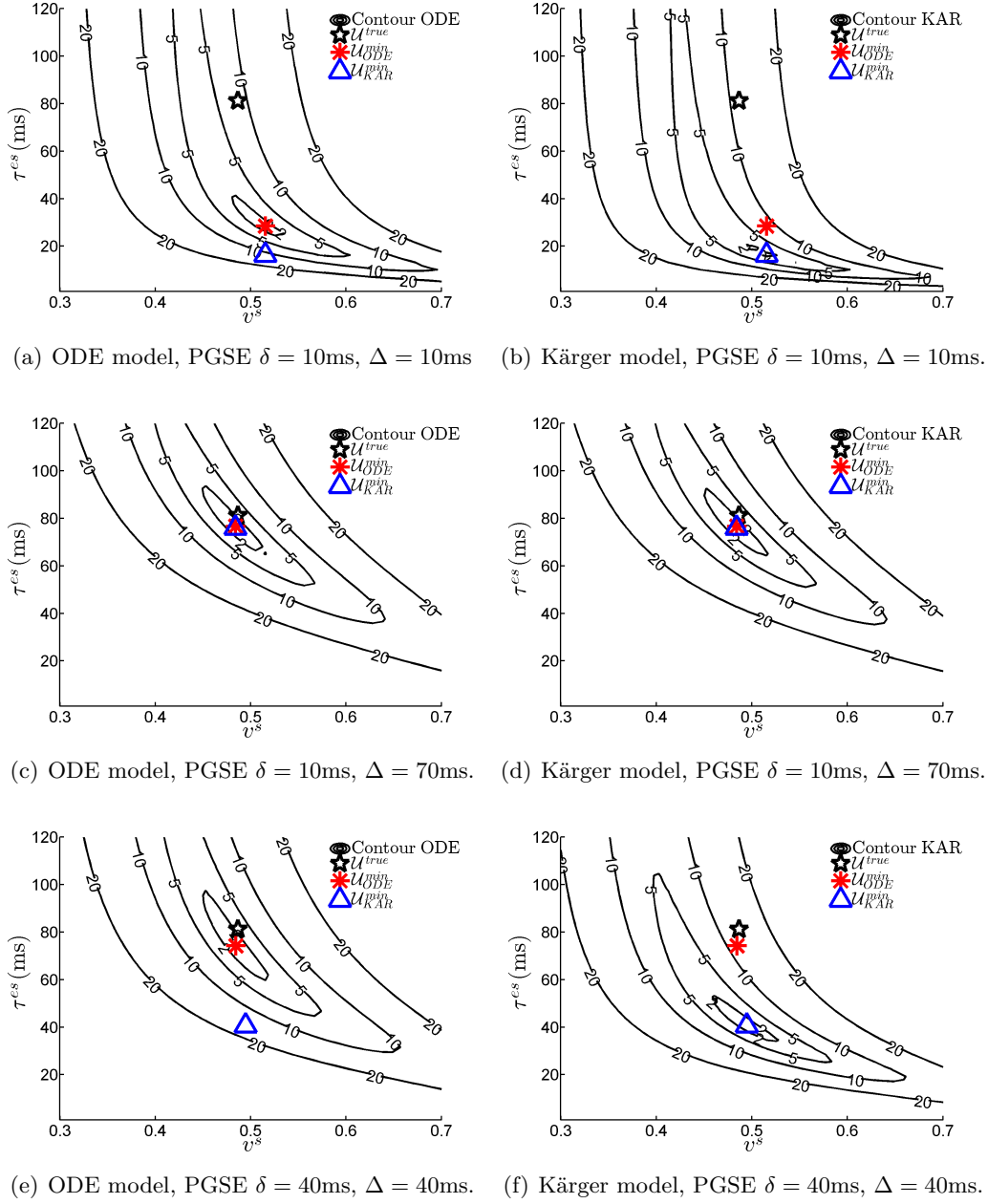


Figure 4.4: Contour plot of ODE model and Kärger model. Periodic lattice of spheres, cell radius $R^s = 2.45\mu\text{m}$, inter-cell distance $L = 5\mu\text{m}$. PGSE sequence, $n_b = 20$.
 R^{mod} : (a) 8.4%, (b) 11.6%, (c) 2.4%, (d) 2.8%, (e) 2.6%, (f) 14%;
 $R_{ODE}(\mathcal{U}_{ODE}^{min})$: (a,b) 1.2%, (c,d) 0.2%, (e,f) 0.2%;
 $R_{KAR}(\mathcal{U}_{KAR}^{min})$: (a,b) 1.5%, (c,d) 0.2%, (e,f) 0.6%.

4.2. Domain containing periodic lattice of spheres of the same size

4.2.5 Effects of b -values

Here we consider the effect of the choice of the number and magnitude of the b -values which are used to fit the signal.

First, we keep the same number of b -values $n_b = 20$ but use different ranges for them:

1. $[0, 1000\text{s/mm}^2]$:
 $b = [0, 20, 50, 100, 150, 200, 250, 300, 350, 400, 450,$
 $500, 550, 600, 650, 700, 750, 800, 900, 1000] \times \text{s/mm}^2.$
2. $[0, 2000\text{s/mm}^2]$:
 $b = [0, 100, 200, 300, 400, 500, 600, 700, 800, 900, 1000,$
 $1100, 1200, 1300, 1400, 1500, 1600, 1700, 1800, 2000] \times \text{s/mm}^2.$
3. $[0, 4000\text{s/mm}^2]$: see Eq. (4.10).

Figure 4.5 shows the contour plots for the two choices of 2-parameters sets defined in Eq. (4.12) and Eq. (4.13). The specific points for two 2-parameter sets of range $[0, 1000\text{s/mm}^2]$:

1. Figure 4.5(a): $\mathcal{U}_{true} = \{v^s = 0.49, D_g^e = 2.32 \times 10^{-3}\text{mm}^2/\text{s}\};$
 $\mathcal{U}_{ODE}^{min} = \{0.48, 2.31 \times 10^{-3}\text{mm}^2/\text{s}\}; \mathcal{U}_{KAR}^{min} = \{0.43, 2.11 \times 10^{-3}\text{mm}^2/\text{s}\}.$
2. Figure 4.5(b): $\mathcal{U}_{true} = \{v^s = 0.49, \tau^{es} = 81\text{ms}\};$
 $\mathcal{U}_{ODE}^{min} = \{0.48, 86\text{ms}\}; \mathcal{U}_{KAR}^{min} = \{0.48, 53\text{ms}\}.$

and range $[0, 2000\text{s/mm}^2]$:

1. Figure 4.5(c): $\mathcal{U}_{true} = \{v^s = 0.49, D_g^e = 2.32 \times 10^{-3}\text{mm}^2/\text{s}\};$
 $\mathcal{U}_{ODE}^{min} = \{0.48, 2.31 \times 10^{-3}\text{mm}^2/\text{s}\}; \mathcal{U}_{KAR}^{min} = \{0.42, 2.04 \times 10^{-3}\text{mm}^2/\text{s}\}.$
2. Figure 4.5(d): $\mathcal{U}_{true} = \{v^s = 0.49, \tau^{es} = 81\text{ms}\};$
 $\mathcal{U}_{ODE}^{min} = \{0.48, 74\text{ms}\}; \mathcal{U}_{KAR}^{min} = \{0.48, 47\text{ms}\}.$

One can see that although the estimations \mathcal{U}_{ODE}^{min} for all three ranges are close to each other and close to \mathcal{U}_{true} , smaller range of b -value tends to stretch out the contour plot at every level, which means the parameters estimation problem is more difficult to solve.

Chapter 4. Parameters estimation using macroscopic dMRI signal models

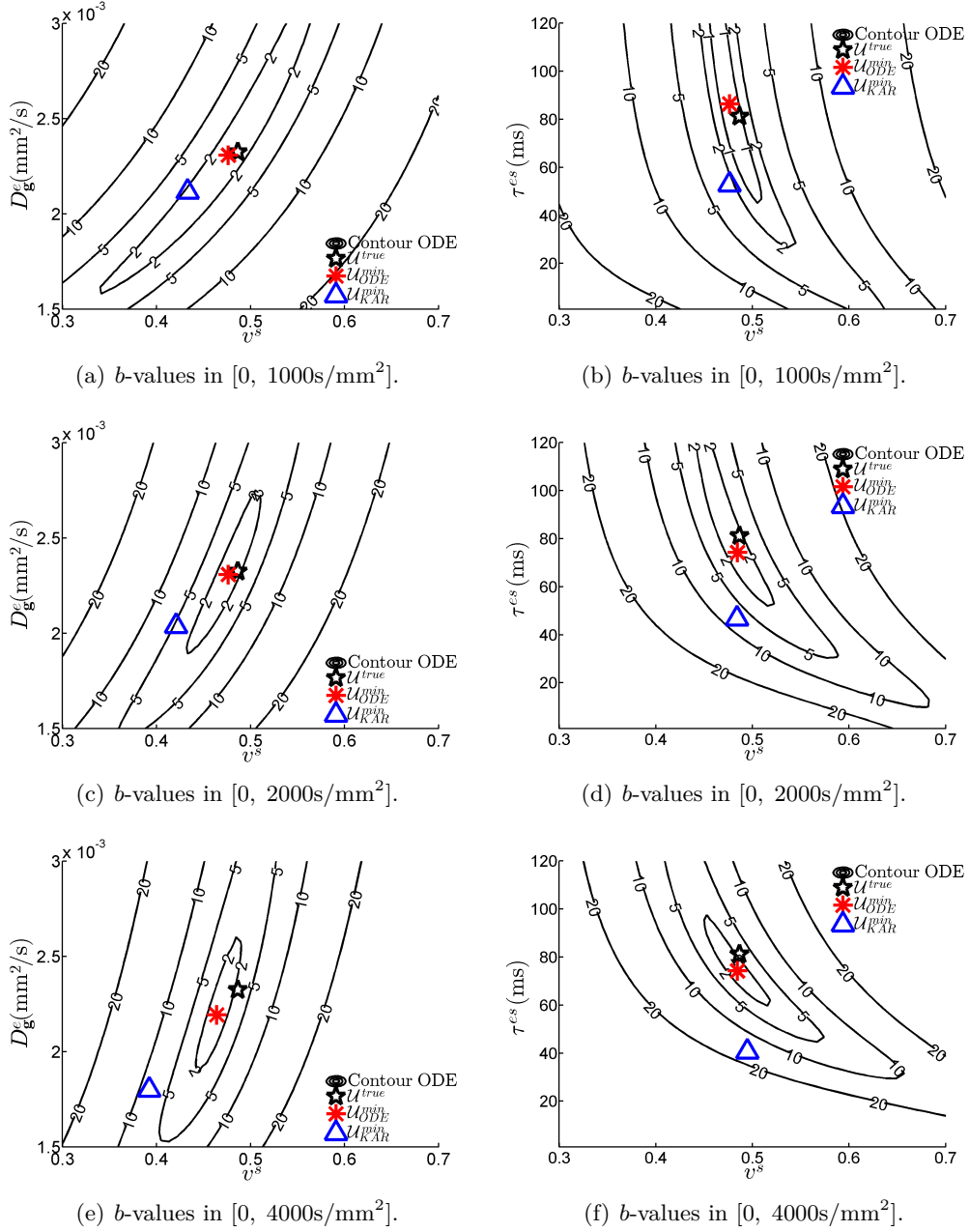


Figure 4.5: Domain containing periodic lattice of spheres shown in Fig. 3.2(a), cell radius $2.45\mu\text{m}$, cell distance $5\mu\text{m}$, contour plot of ODE model with PGSE profile $\delta = 40\text{ms}$, $\Delta = 40\text{ms}$, $n_b = 20$ b -values in range (a) [0, 1000s/mm²], (b) [0, 2000s/mm²], (c) [0, 1000s/mm²].

R^{mod} : (a,b) 0.8%, (c,d) 1.5%, (e,f) 2.6%;

$R_{ODE}(U_{ODE}^{min})$: (a) 0.1%, (b) 0.1%, (c) 0.1%, (d) 0.2%, (e) 0.5%, (f) 0.2%;

$R_{KAR}(U_{KAR}^{min})$: (a) 0.1%, (b) 0.1%, (c) 0.4%, (d) 0.3%, (e) 1.6%, (f) 0.6%.

4.2. Domain containing periodic lattice of spheres of the same size

Next we fix the range of b -values to $[0, 4000\text{s}/\text{mm}^2]$ and use different numbers of b -values:

1. $n_b = 10$:
 $b = [0, 250, 500, 1000, 1500, 2000, 2500, 3000, 3500, 4000] \times \text{s}/\text{mm}^2$.
2. $n_b = 20$: see Eq. (4.10).
3. $n_b = 40$:
 $b = [0, 20, 50, 100, 200, 300, 400, 500, 600, 700, 800, 900, 1000, 1100, 1200, 1300, 1400, 1500, 1600, 1700, 1800, 1900, 2000, 2100, 2200, 2300, 2400, 2500, 2600, 2700, 2800, 2900, 3000, 3100, 3200, 3300, 3400, 3600, 3800, 4000] \times \text{s}/\text{mm}^2$.

On Fig. 4.6, the specific points for two 2-parameter sets of $n_b = 10$:

1. Figure 4.6(a): $\mathcal{U}_{true} = \{v^s = 0.49, D_g^e = 2.32 \times 10^{-3}\text{mm}^2/\text{s}\}$;
 $\mathcal{U}_{ODE}^{min} = \{0.47, 2.23 \times 10^{-3}\text{mm}^2/\text{s}\}$; $\mathcal{U}_{KAR}^{min} = \{0.40, 1.85 \times 10^{-3}\text{mm}^2/\text{s}\}$.
2. Figure 4.6(b): $\mathcal{U}_{true} = \{v^s = 0.49, \tau^{es} = 81\text{ms}\}$;
 $\mathcal{U}_{ODE}^{min} = \{0.48, 74\text{ms}\}$; $\mathcal{U}_{KAR}^{min} = \{0.50, 41\text{ms}\}$.

and $n_b = 40$:

1. Figure 4.6(e): $\mathcal{U}_{true} = \{v^s = 0.49, D_g^e = 2.32 \times 10^{-3}\text{mm}^2/\text{s}\}$;
 $\mathcal{U}_{ODE}^{min} = \{0.47, 2.23 \times 10^{-3}\text{mm}^2/\text{s}\}$; $\mathcal{U}_{KAR}^{min} = \{0.40, 1.85 \times 10^{-3}\text{mm}^2/\text{s}\}$.
2. Figure 4.6(f): $\mathcal{U}_{true} = \{v^s = 0.49, \tau^{es} = 81\text{ms}\}$;
 $\mathcal{U}_{ODE}^{min} = \{0.48, 74\text{ms}\}$; $\mathcal{U}_{KAR}^{min} = \{0.50, 41\text{ms}\}$.

Despite of using different numbers of b -values, not only the \mathcal{U}_{ODE}^{min} for different n_b are close to each other and close to \mathcal{U}_{true} , but their contour plots are also very similar for both choices of 2-parameters sets. This shows that for the signal *without noise*, the number of b -values which cover a fixed range has a small effect on the ODE and Kärger models parameter estimations.

Chapter 4. Parameters estimation using macroscopic dMRI signal models

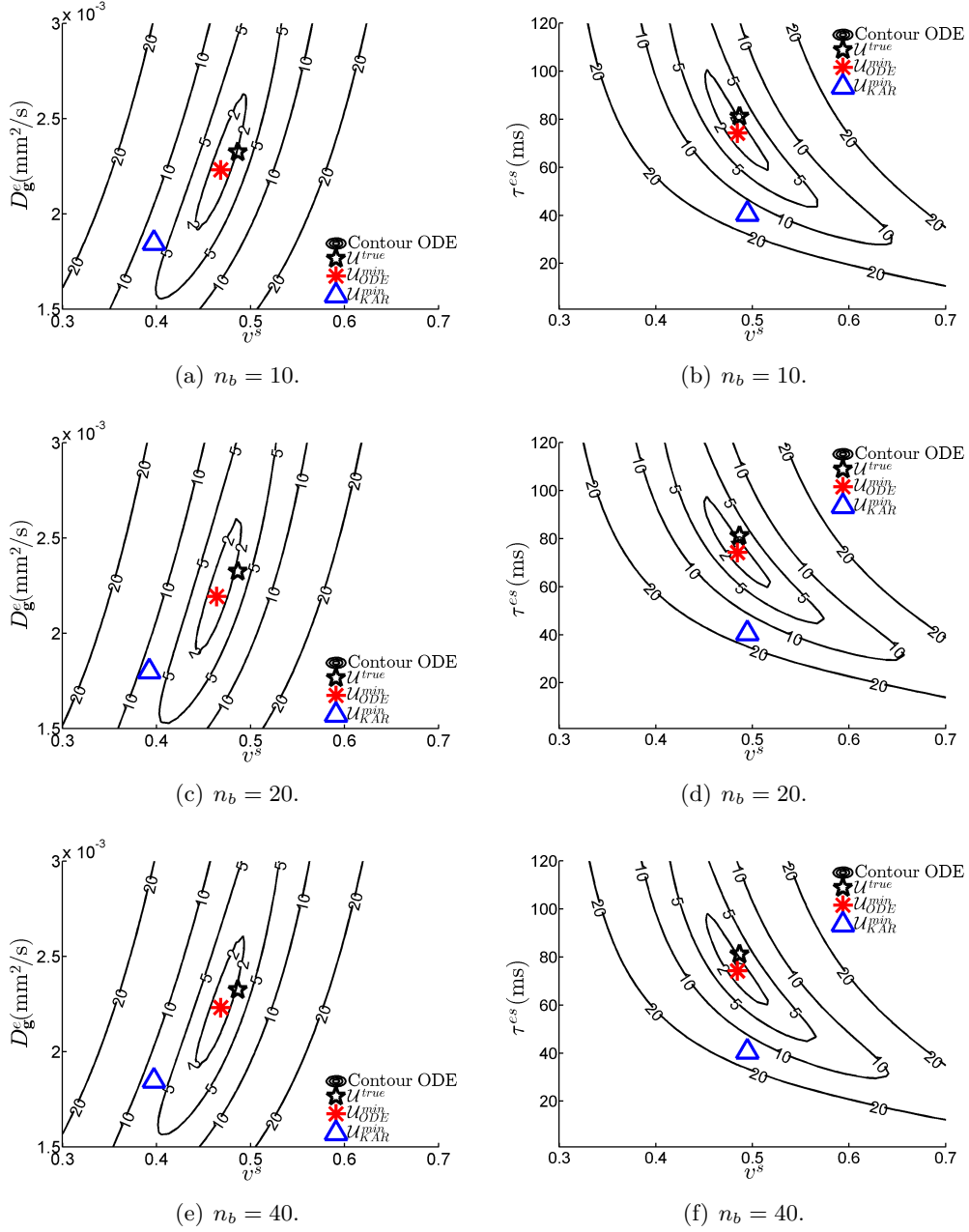


Figure 4.6: Domain containing periodic lattice of spheres in shown Fig. 3.2(a), cell radius $2.45\mu\text{m}$, cell distance $5\mu\text{m}$, contour plot of ODE model with PGSE profile $\delta = 40\text{ms}$, $\Delta = 40\text{ms}$, fixed range b -value in $[0, 4000\text{s/mm}^2]$ with different numbers (a) $n_b = 10$ (b) $n_b = 20$ (c) $n_b = 40$.

R^{mod} : (a,b) 2.2%, (c,d) 2.6%, (e,f) 2.4%;

$R_{ODE}(\mathcal{U}_{ODE}^{min})$: (a) 0.4%, (b) 0.2%, (c) 0.5%, (d) 0.2%, (e) 0.4%, (f) 0.2%;

$R_{KAR}(\mathcal{U}_{KAR}^{min})$: (a) 1.4%, (b) 0.6%, (c) 1.6%, (d) 0.6%, (e) 1.5%, (f) 0.6%.

4.2. Domain containing periodic lattice of spheres of the same size

4.2.6 Effects of cell size

Here we study the effect of cell size on the ODE model parameters estimation.

In details, we compare two sizes of cells:

1. cell radius $R^s = 2.45\mu\text{m}$ with cell distance $L = 5\mu\text{m}$;
2. cell radius $R^s = 4.9\mu\text{m}$ with cell distance $L = 10\mu\text{m}$.

This choice makes both computational domains to have the same volume fraction of the spherical cells compartment $v^s = 0.49$ and also preserves the effective diffusion coefficient of the extra-cellular compartment: $D_{\mathbf{g}}^e = 2.32 \times 10^{-3}$. (We will discuss in detail the relationship between v^s and $D_{\mathbf{g}}^e$ in Sect. 4.7.) In turn, the domain containing the spherical cells $R^s = 4.9\mu\text{m}$ with cell distance $L = 10\mu\text{m}$ with double geometrical length gives double residence time: $\tau^{es} = 162\text{ms}$. In summary, for $R^s = 4.9\mu\text{m}$ and $L = 10\mu\text{m}$, the true 3-parameters set is:

$$\mathcal{U}_{true} = \left\{ v^s = 0.49, D_{\mathbf{g}}^e = 2.32 \times 10^{-3} \text{mm}^2/\text{s}, \tau^{es} = 162\text{ms} \right\}.$$

We make the contour plots for different PGSE sequences:

1. short diffusion time: $\delta = 10\text{ms}$, $\Delta = 10\text{ms}$;
2. long diffusion time: $\delta = \Delta = 40\text{ms}$;
3. very long diffusion time: $\delta = \Delta = 80\text{ms}$.

Figures 4.7 and 4.8 show the contour plots for the two choices of 2-parameters sets defined in Eq. (4.12) and Eq. (4.13), respectively. On Fig. 4.7, the specific points of \mathcal{U}_{true} and \mathcal{U}_{ODE}^{min} for first 2-parameters set are:

- $R^s = 2.45\mu\text{m}$, $L = 5\mu\text{m}$ and $R^s = 4.9\mu\text{m}$, $L = 10\mu\text{m}$:
 $\mathcal{U}_{true} = \{v^s = 0.49, D_{\mathbf{g}}^e = 2.32 \times 10^{-3} \text{mm}^2/\text{s}\}.$
- $\delta = 10\text{ms}$, $\Delta = 10\text{ms}$:
 $R^s = 2.45\mu\text{m}$, $L = 5\mu\text{m}$ (Fig. 4.7(a)): $\mathcal{U}_{ODE}^{min} = \{0.43, 1.92 \times 10^{-3} \text{mm}^2/\text{s}\}.$
 $R^s = 4.9\mu\text{m}$, $L = 10\mu\text{m}$ (Fig. 4.7(b)): $\mathcal{U}_{ODE}^{min} = \{0.30, 1.65 \times 10^{-3} \text{mm}^2/\text{s}\}.$
- $\delta = 40\text{ms}$, $\Delta = 40\text{ms}$:
 $R^s = 2.45\mu\text{m}$, $L = 5\mu\text{m}$ (Fig. 4.7(c)): $\mathcal{U}_{ODE}^{min} = \{0.47, 2.23 \times 10^{-3} \text{mm}^2/\text{s}\};$
 $R^s = 4.9\mu\text{m}$, $L = 10\mu\text{m}$ (Fig. 4.7(d)): $\mathcal{U}_{ODE}^{min} = \{0.41, 1.85 \times 10^{-3} \text{mm}^2/\text{s}\}.$
- $\delta = 80\text{ms}$, $\Delta = 80\text{ms}$:
 $R^s = 2.45\mu\text{m}$, $L = 5\mu\text{m}$ (Fig. 4.7(e)): $\mathcal{U}_{ODE}^{min} = \{0.47, 2.27 \times 10^{-3} \text{mm}^2/\text{s}\};$
 $R^s = 4.9\mu\text{m}$, $L = 10\mu\text{m}$ (Fig. 4.7(f)): $\mathcal{U}_{ODE}^{min} = \{0.44, 2.12 \times 10^{-3} \text{mm}^2/\text{s}\}.$

and for second 2-parameters set are:

- $R^s = 2.45\mu\text{m}, L = 5\mu\text{m}$: $\mathcal{U}_{true} = \{v^s = 0.49, \tau^{es} = 81\text{ms}\}$;
 $R^s = 4.9\mu\text{m}, L = 10\mu\text{m}$: $\mathcal{U}_{true} = \{v^s = 0.49, \tau^{es} = 162\text{ms}\}$.
- $\delta = 10\text{ms}, \Delta = 10\text{ms}$:
 $R^s = 2.45\mu\text{m}, L = 5\mu\text{m}$ (Fig. 4.8(a)): $\mathcal{U}_{ODE}^{min} = \{0.52, 28\text{ms}\}$;
 $R^s = 4.9\mu\text{m}, L = 10\mu\text{m}$ (Fig. 4.8(b)): $\mathcal{U}_{ODE}^{min} = \{0.61, 6\text{ms}\}$.
- $\delta = 40\text{ms}, \Delta = 40\text{ms}$:
 $R^s = 2.45\mu\text{m}, L = 5\mu\text{m}$ (Fig. 4.8(c)): $\mathcal{U}_{ODE}^{min} = \{0.48, 74\text{ms}\}$;
 $R^s = 4.9\mu\text{m}, L = 10\mu\text{m}$ (Fig. 4.8(d)): $\mathcal{U}_{ODE}^{min} = \{0.51, 83\text{ms}\}$.
- $\delta = 80\text{ms}, \Delta = 80\text{ms}$:
 $R^s = 2.45\mu\text{m}, L = 5\mu\text{m}$ (Fig. 4.8(e)): $\mathcal{U}_{ODE}^{min} = \{0.48, 78\text{ms}\}$;
 $R^s = 4.9\mu\text{m}, L = 10\mu\text{m}$ (Fig. 4.8(f)): $\mathcal{U}_{ODE}^{min} = \{0.48, 134\text{ms}\}$.

We see that the modeling errors are much larger at the larger radius. It takes a very long diffusion time, for example $\delta = \Delta = 80\text{ms}$, to get \mathcal{U}_{ODE}^{min} to be closer to \mathcal{U}_{true} .

4.2. Domain containing periodic lattice of spheres of the same size

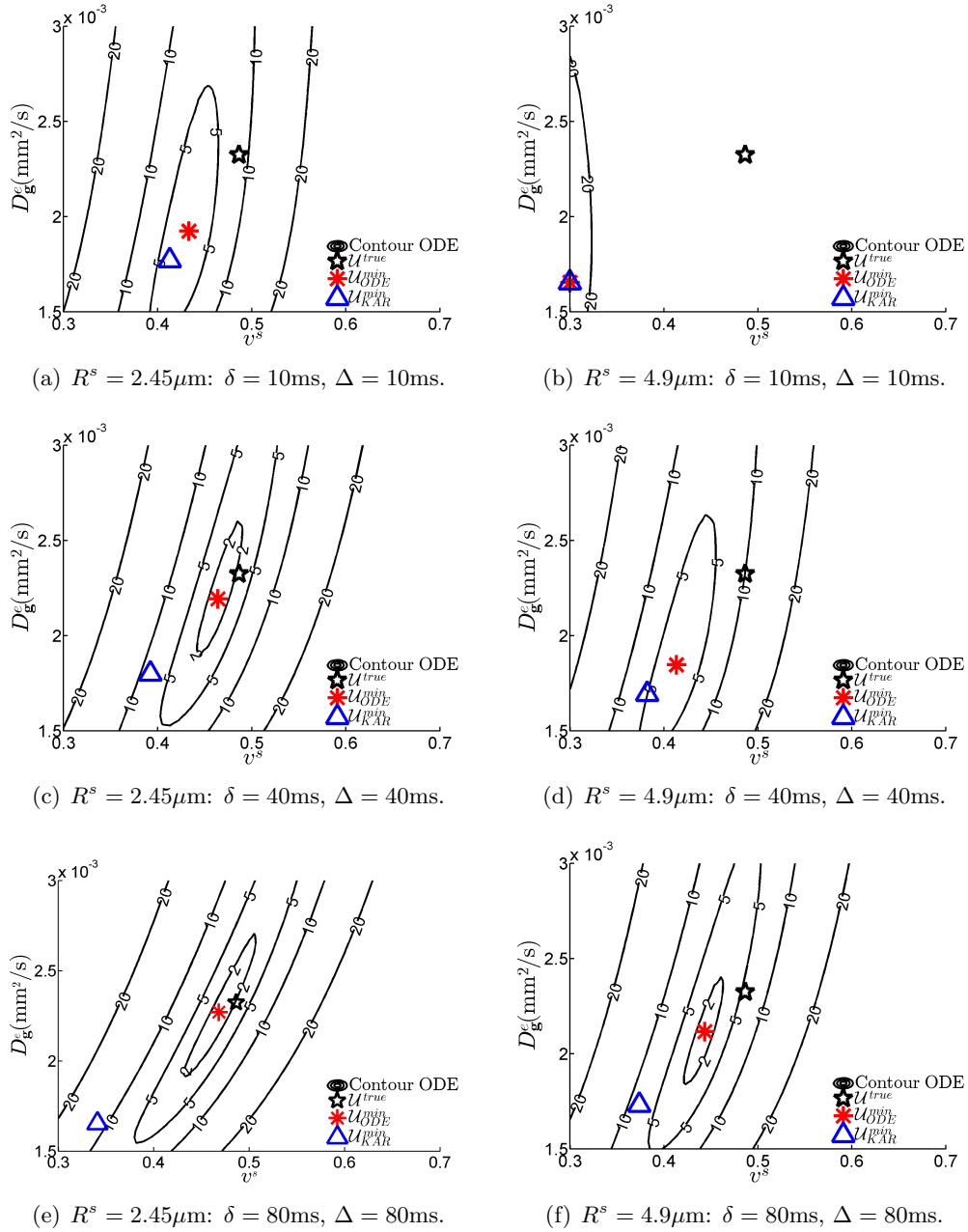


Figure 4.7: Domain containing periodic lattice of spheres shown in Fig. 3.2(a). Contour plot of ODE model with respect to v^s and D_g^e , $n_b = 20$.

R^{mod} : (a) 8.4%, (b) 59.7%, (c) 2.6%, (d) 10.1%, (e) 2.2%, (f) 5.7%;

$R_{ODE}(U_{ODE}^{min})$: (a) 2.3%, (b) 15.6%, (c) 0.5%, (d) 2.2%, (e) 0.4%, (f) 1.0%;

$R_{KAR}(U_{KAR}^{min})$: (a) 2.5%, (b) 16.7%, (c) 1.6%, (d) 2.7%, (e) 2.0%, (f) 2.0%.

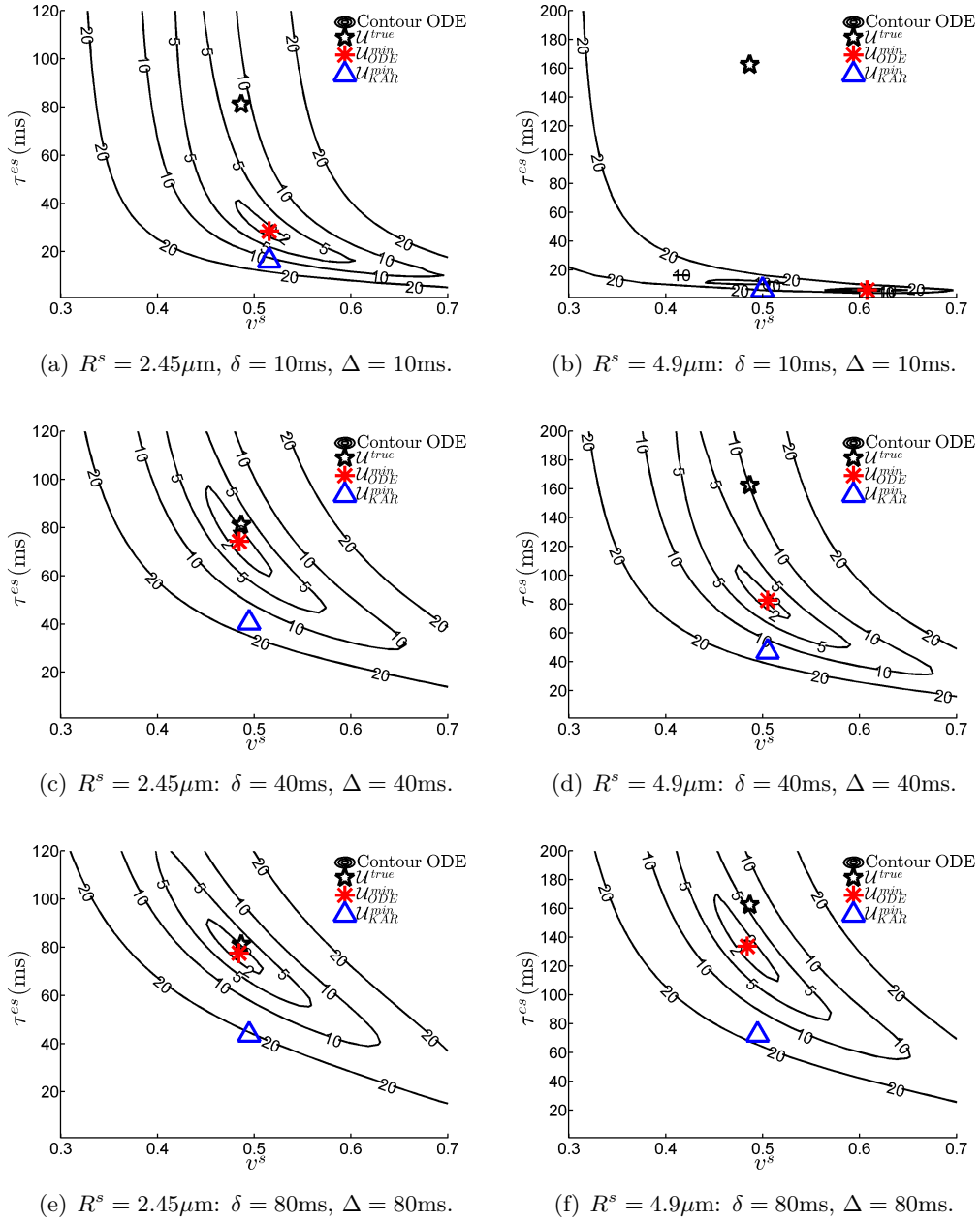


Figure 4.8: Domain containing periodic lattice of spheres shown in Fig. 3.2(a). Contour plot of ODE model with respect to v^s and τ^{es} , $n_b = 20$.

R^{mod} : (a) 8.4%, (b) 59.7%, (c) 2.6%, (d) 10.1% , (e) 2.2%, (f) 5.7%;

$R_{ODE}(\mathcal{U}_{ODE}^{min})$: (a) 1.2%, (b) 5.5%, (c) 0.2%, (d) 1.2% , (e) 0.2%, (f) 0.5%;

$R_{KAR}(\mathcal{U}_{KAR}^{min})$: (a) 1.5%, (b) 6.8%, (c) 0.6%, (d) 1.6% , (e) 0.7%, (f) 1.0%.

4.3. Periodic lattice of spherical cells of different sizes

4.3 Periodic lattice of spherical cells of different sizes

For the domain shown in Fig. 3.8(a), which contains many spherical cells of different sizes, we study the parameters estimation problem for different membrane permeabilities and investigate the effect of noisy signals. There are two compartments: Ω^e , the extra-cellular compartment, and Ω^s containing all 76 spherical cells with different radii between $0.6 - 2.55\mu\text{m}$. The corresponding volume fractions of this domain are $v^s = 0.65$ and $v^e = 0.35$.

4.3.1 Least squares problem on 3-parameters set

The least squares problems we solve remain Eq. (4.5) and Eq. (4.6). The 3-parameters set to be estimated is:

$$\mathcal{U} = \left\{ v^s, D_{\mathbf{g}}^e, \tau^{es} \right\}, \quad (4.14)$$

where $\tau^{es} \equiv \frac{|\Omega^s|}{\kappa|\Gamma^{es}|}$. The constraints are:

$$\begin{aligned} \frac{\tau^{es}}{\tau^{se}} &= \frac{v^s}{v^e}, \\ v^e + v^s &= 1, \\ 0 < D_{\mathbf{g}}^e &\leq D^0, \\ \overline{D}^s &= 0, \text{ because } \Omega^s \text{ is compact,} \\ 0 \leq v^m &\leq 1 \text{ and } 0 \leq \tau^{es}. \end{aligned}$$

The true model three-parameters set for this domain are:

$$\mathcal{U}_{true} = \left\{ v^s = 0.65, D_{\mathbf{g}}^e = 2.20 \times 10^{-3} \text{mm}^2/\text{s}, \tau^{es} = \tau_{true}^{es} \right\}.$$

where τ_{true}^{es} is given in Table 4.2 for each permeability. We also use the same initial guesses of the least squares problem as for the domain containing periodic lattice of spheres:

$$\mathcal{U}^0 = \left\{ c_v, \frac{D^0}{2}, c_\tau \frac{\tau_{true}^{es} \tau_{true}^{se}}{2(\tau_{true}^{es} + \tau_{true}^{se})} \right\},$$

where c_v is a random number (of a uniform distribution) between 0 and 1, c_τ is between 0.1 and 10. For this domain, we also did not see any difference of parameter estimation results when c_v and c_τ are varied.

Table 4.2 contains parameters estimation results for: $\kappa = 10^{-6}\text{m/s}$ ($\delta = \Delta = 100\text{ms}$), $\kappa = 2.5 \times 10^{-6}\text{m/s}$ ($\delta = \Delta = 80\text{ms}$), $\kappa = 5 \times 10^{-6}\text{m/s}$ ($\delta = \Delta = 50\text{ms}$), $\kappa = 10^{-5}\text{m/s}$ ($\delta = \Delta = 30\text{ms}$), $\kappa = 2.5 \times 10^{-5}\text{m/s}$ ($\delta = \Delta = 20\text{ms}$), $\kappa = 5 \times 10^{-5}\text{m/s}$ ($\delta = \Delta = 10\text{ms}$), $\kappa = 10^{-4}\text{m/s}$ ($\delta = \Delta = 5\text{ms}$). In this likely anisotropic diffusion domain, all of these signals were obtained using the same gradient direction $\mathbf{g} = (1, 0, 0)$ and are considered without noise. We can see that the results of the ODE model are always much better than that of the Kärger model. It is necessary to emphasize that for these examples the narrow pulse assumption does not hold because δ is not small compared to Δ . For low permeability ($\kappa = 10^{-6}\text{m/s}$, $\kappa = 2.5 \times 10^{-6}\text{m/s}$) and intermediate permeability ($\kappa = 5 \times 10^{-6}\text{m/s}$, $\kappa = 10^{-5}\text{m/s}$, $\kappa = 2.5 \times 10^{-5}\text{m/s}$), the estimated parameters are very good. At high permeability ($\kappa = 5 \times 10^{-5}\text{m/s}$, $\kappa = 10^{-5}\text{m/s}$), the macroscopic models are not good approximations of

Chapter 4. Parameters estimation using macroscopic dMRI signal models

the full PDE model, as can be seen by the large modeling errors, thus the parameters estimation results are not as accurate. For instance, for $\kappa = 5 \times 10^{-5}$ m/s, the modeling error for the ODE model is 7.6%, and the estimated parameters are still reasonable. But at very high permeability $\kappa = 10^{-4}$ m/s, the estimated parameters are very inaccurate due to the large modeling error, 20% in this case.

κ (m/s) - PGSE (ms)	Parameter	\mathcal{U}^{true}	\mathcal{U}_{ODE}^{min}	\mathcal{U}_{KAR}^{min}
$\kappa = 1 \times 10^{-6}$ m/s $\delta = 100$ ms $\Delta = 100$ ms	v^s	0.65	0.65	0.67
	τ^{es} (ms)	540	522	254
	D_g^e ($\times 10^{-3}$ mm ² /s)	2.20	2.21	2.37
	$R(\mathcal{U}^{min})$		0.02%	0.09%
	R^{mod}		0.09%	3.4%
$\kappa = 2.5 \times 10^{-6}$ m/s $\delta = 80$ ms $\Delta = 80$ ms	v^s	0.65	0.65	0.69
	τ^{es} (ms)	216	217	104
	D_g^e ($\times 10^{-3}$ mm ² /s)	2.20	2.20	2.57
	$R(\mathcal{U}^{min})$		0.02%	0.14%
	R^{mod}		0.76%	6.0%
$\kappa = 5 \times 10^{-6}$ m/s $\delta = 50$ ms $\Delta = 50$ ms	v^s	0.65	0.65	0.71
	τ^{es} (ms)	108	108	51
	D_g^e ($\times 10^{-3}$ mm ² /s)	2.20	2.22	2.74
	$R(\mathcal{U}^{min})$		0.03%	0.17%
	R^{mod}		0.2%	7.6%
$\kappa = 1 \times 10^{-5}$ m/s $\delta = 30$ ms $\Delta = 30$ ms	v^s	0.65	0.65	0.73
	τ^{es} (ms)	54	53	25
	D_g^e ($\times 10^{-3}$ mm ² /s)	2.20	2.26	3.00
	$R(\mathcal{U}^{min})$		0.05%	0.2%
	R^{mod}		0.9%	9.5%
$\kappa = 2.5 \times 10^{-5}$ m/s $\delta = 20$ ms $\Delta = 20$ ms	v^s	0.65	0.64	0.73
	τ^{es} (ms)	22	21	10
	D_g^e ($\times 10^{-3}$ mm ² /s)	2.20	2.29	3.00
	$R(\mathcal{U}^{min})$		0.06%	0.3%
	R^{mod}		2.6%	15.0%
$\kappa = 5 \times 10^{-5}$ m/s $\delta = 10$ ms $\Delta = 10$ ms	v^s	0.65	0.66	0.76
	τ^{es} (ms)	11	9	5
	D_g^e ($\times 10^{-3}$ mm ² /s)	2.20	2.53	3.00
	$R(\mathcal{U}^{min})$		1.5%	5.6%
	R^{mod}		7.6%	21.1%
$\kappa = 1 \times 10^{-4}$ m/s $\delta = 5$ ms $\Delta = 5$ ms	v^s	0.65	0.68	0.69
	τ^{es} (ms)	5	4	2
	D_g^e ($\times 10^{-3}$ mm ² /s)	2.20	3.00	3.00
	$R(\mathcal{U}^{min})$		4.2%	11%
	R^{mod}		20%	36%

Table 4.2: Parameters estimation results for the domain containing periodic lattice of spherical cells of different sizes shown in Fig. 3.8(a), with different permeabilities.

4.3. Periodic lattice of spherical cells of different sizes

4.3.2 Contour plots of 2-parameters sets

We also show in Fig. 4.9 the contour plots for the two choices of 2-parameters sets defined in Eq. (4.12) and Eq. (4.13). The specific points for two 2-parameter sets are:

1. Figures 4.9(a) and 4.9(b): $\mathcal{U}_{true} = \{v^s = 0.65, D_{og}^e = 2.20 \times 10^{-3} \text{mm}^2/\text{s}\}$;
 $\mathcal{U}_{ODE}^{min} = \{0.64, 2.21 \times 10^{-3} \text{mm}^2/\text{s}\}$; $\mathcal{U}_{KAR}^{min} = \{0.53, 1.50 \times 10^{-3} \text{mm}^2/\text{s}\}$.
2. Figures 4.9(c) and 4.9(d): $\mathcal{U}_{true} = \{v^s = 0.65, \tau^{es} = 54 \text{ms}\}$;
 $\mathcal{U}_{ODE}^{min} = \{0.64, 53 \text{ms}\}$; $\mathcal{U}_{KAR}^{min} = \{0.64, 32 \text{ms}\}$.

Once again, these contour plots show that \mathcal{U}_{ODE}^{min} are very close to \mathcal{U}_{true} while \mathcal{U}_{KAR}^{min} are not.

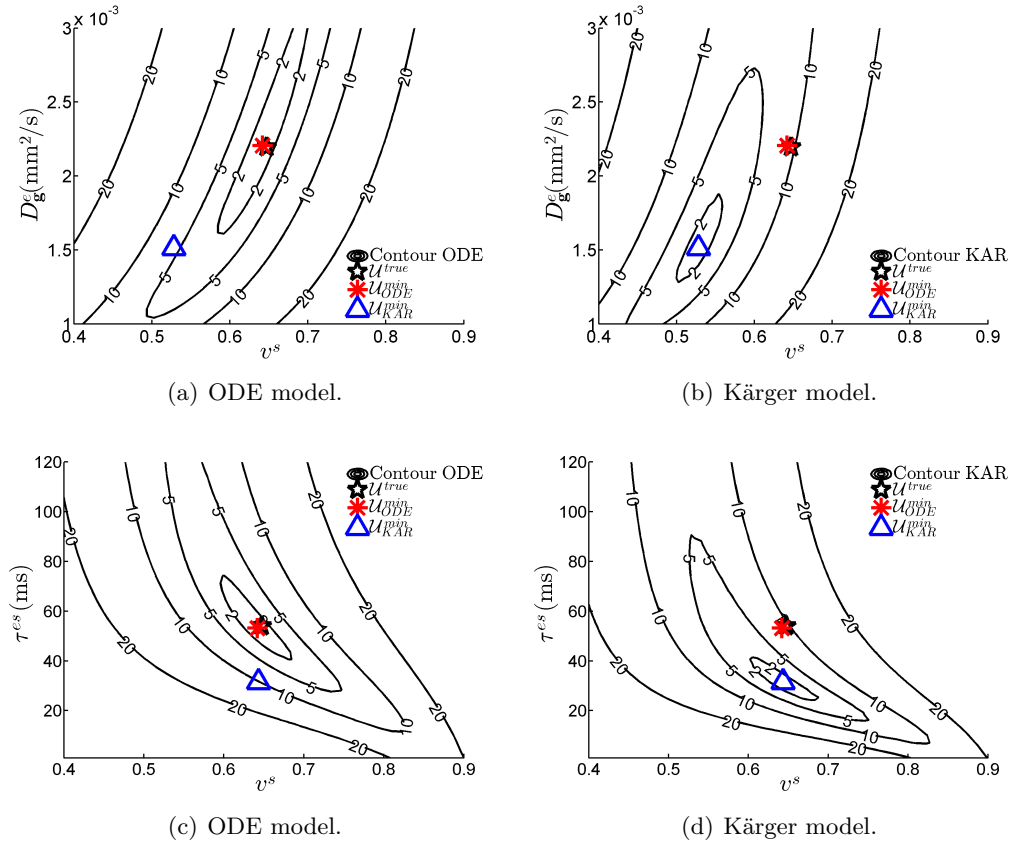


Figure 4.9: Domain containing spherical cells of different sizes, $\kappa = 10^{-5} \text{m/s}$, PGSE profile $\delta = \Delta = 30 \text{ms}$, contour plots of ODE model and Kärger model.

R^{mod} : (a,c) 0.9%, (b,d) 9.5%;

$R_{ODE}(\mathcal{U}_{ODE}^{min})$: (a,b) 0.2%, (c,d) 0.2%; $R_{KAR}(\mathcal{U}_{KAR}^{min})$: (a,b) 0.9%, (c,d) 0.4%.

4.3.3 Effect of noisy signal

Now we add N realizations of random noise to the signal at the n_b b -values:

$$(S_{PDE})_i^{noi}(b_k) = S_{PDE}(b_k) + \mathcal{N}_{b_k}^i(0, \sigma^2), \quad k = 1, \dots, n_b, \quad i = 1, \dots, N, \quad (4.15)$$

to get N samples of the noisy signal $(S_{PDE})_i^{noi}$. The 3-parameters set for the parameters estimation problem remains that from Eq. (4.14).

We define the solution of the least squares problem subject to the noisy signal $(S_{PDE})_i^{noi}$ by

$$\left(\mathcal{U}_{ODE}^{min}\right)_i^{noi}$$

and

$$\left(\mathcal{U}_{KAR}^{min}\right)_i^{noi}.$$

The average of estimated parameters for the N realizations of the noisy signal is defined as

$$\left(\mathcal{U}_{ODE}^{min}\right)_{ave}^{noi} \equiv \frac{1}{N} \sum_{i=1}^N \left(\mathcal{U}_{ODE}^{min}\right)_i^{noi}$$

and

$$\left(\mathcal{U}_{KAR}^{min}\right)_{ave}^{noi} \equiv \frac{1}{N} \sum_{i=1}^N \left(\mathcal{U}_{KAR}^{min}\right)_i^{noi}.$$

We also give a measure of the relative standard deviations of $\left(\mathcal{U}_{ODE}^{min}\right)_i^{noi}$ and $\left(\mathcal{U}_{KAR}^{min}\right)_i^{noi}$:

$$\sigma_{ODE} \equiv \sqrt{\frac{1}{N} \sum_{i=1}^N \left| \frac{\left(\mathcal{U}_{ODE}^{min}\right)_i^{noi} - \left(\mathcal{U}_{ODE}^{min}\right)_{ave}^{noi}}{\left(\mathcal{U}_{ODE}^{min}\right)_{ave}^{noi}} \right|^2}$$

and

$$\sigma_{KAR} \equiv \sqrt{\frac{1}{N} \sum_{i=1}^N \left| \frac{\left(\mathcal{U}_{KAR}^{min}\right)_i^{noi} - \left(\mathcal{U}_{KAR}^{min}\right)_{ave}^{noi}}{\left(\mathcal{U}_{KAR}^{min}\right)_{ave}^{noi}} \right|^2}.$$

Table 4.3 shows the results of $N = 100$ realizations of noisy signals for two levels of noise: $\sigma = 0.01$, $\sigma = 0.03$ and three different numbers of b -values: $n_b = 25$, $n_b = 100$ and $n_b = 400$. For each case, b -values are varied on a uniform grid of $[0, 4000]$ s/mm².

The results show that larger noise requires more b -values to reduce the error of parameter estimations. In fact, one can see on Table 4.3 that using more b -values not only decreases the relative standard deviation of all parameter estimations but also moves the average estimation of parameters closer to the true values for both small noise $\sigma = 0.01$ and large noise $\sigma = 0.03$.

4.3. Periodic lattice of spherical cells of different sizes

σ noise	n_b	Parameter	σ_{ODE}^{ave}	σ_{KAR}^{ave}	\mathcal{U}_{true}	$(\mathcal{U}_{ODE}^{min})^{noi}$	$(\mathcal{U}_{KAR}^{min})^{noi}$
0.01	25	v^s	7%	10%	0.65	0.65	0.69
		τ^{es} (ms)	21%	51%	54	47	29
		D^e ($\times 10^{-3}$ mm ² /s)	16%	26%	2.2	2.3	2.7
	100	v^s	4%	11%	0.65	0.65	0.72
		τ^{es} (ms)	7%	52%	54	52	25
		D^e ($\times 10^{-3}$ mm ² /s)	9.5%	30%	2.2	2.3	2.8
	400	v^s	2%	11%	0.65	0.65	0.72
		τ^{es} (ms)	5%	53%	54	52	25
		D^e ($\times 10^{-3}$ mm ² /s)	6%	32%	2.2	2.3	2.9
0.03	25	v^s	12%	13%	0.65	0.64	0.67
		τ^{es} (ms)	45%	66%	54	67	44
		D^e ($\times 10^{-3}$ mm ² /s)	28%	30%	2.2	2.2	2.3
	100	v^s	9%	11%	0.65	0.66	0.69
		τ^{es} (ms)	25%	48%	54	57	30
		D^e ($\times 10^{-3}$ mm ² /s)	24%	28%	2.2	2.4	2.7
	400	v^s	6%	10%	0.65	0.65	0.69
		τ^{es} (ms)	13%	50%	54	54	29
		D^e ($\times 10^{-3}$ mm ² /s)	14%	26%	2.2	2.3	2.7

Table 4.3: Relative errors of \mathcal{U} for the domain shown in Fig. 3.8(a) from $N = 100$ samples of Gaussian noises $\mathcal{N}(0, 0.01)$ and $\mathcal{N}(0, 0.03)$, $\kappa = 10^{-5}$ m/s, PGSE sequence with $\delta = \Delta = 30$ ms.

R^{mod} : (a,b,c,d,e,f) 0.9%.

Figure 4.10 shows the contour plots of $R_{ODE}(\mathcal{U})$ for two choices of 2-parameters sets defined in Eq. (4.12) and Eq. (4.13). Because the parameters estimation problems are posed only on 2-parameters sets we were able to solve the least squares problems in shorter computational time than when the full 3-parameters set is to be estimated. Hence, we give results for $N = 1000$ samples of noisy signals (whereas in Table 4.3 only $N = 100$ samples of noisy signals were used). Importantly, we plot in Fig. 4.10 the *convex hulls* of:

$$\left\{ \left(\mathcal{U}_{ODE}^{min} \right)_i^{noi} \right\}_{i=1, \dots, N=1000}$$

and

$$\left\{ \left(\mathcal{U}_{KAR}^{min} \right)_i^{noi} \right\}_{i=1, \dots, N=1000}.$$

We also show results of parameters estimation while using three previous sets of b -values with different numbers: $n_b = 25$, $n_b = 100$ and $n_b = 400$. One can see that with more b -values, each convex hull shrinks to the corresponding true least squares solution without noise and this position is very close to \mathcal{U}_{true} .

Chapter 4. Parameters estimation using macroscopic dMRI signal models

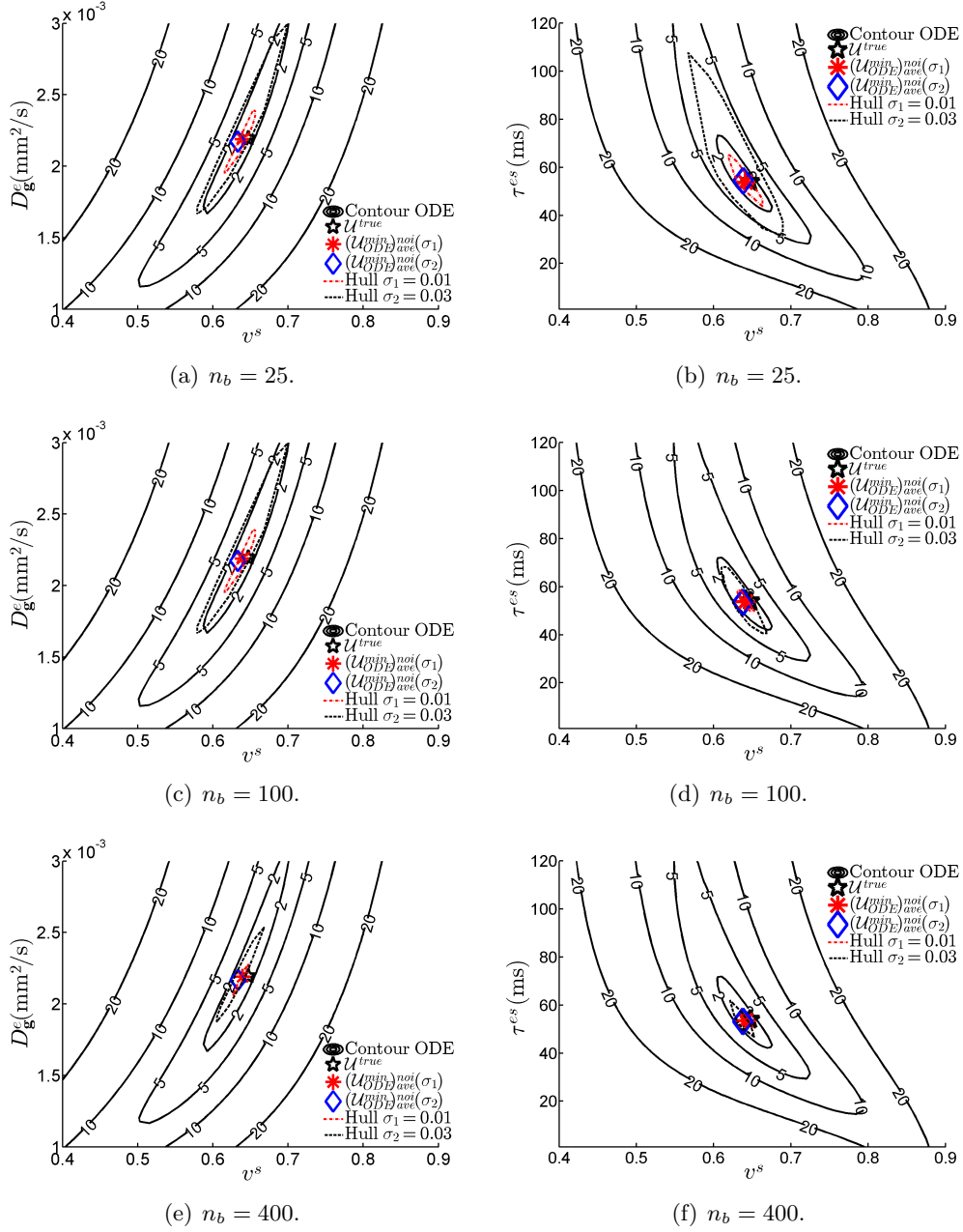


Figure 4.10: Domain containing spherical cells of different sizes: $\kappa = 10^{-5}$ m/s, PGSE with $\delta = \Delta = 30$ ms, convex hulls of 1000 samples of noisy signal with two noise levels: $\sigma_1 = 0.01$ and $\sigma_2 = 0.03$, contour plot of ODE model with respect to v^s and D_g^e (a,c,e) and v^s and τ^{es} (b,d,f).

R^{mod} : (a,b,c,d,e,f) 0.9%.

4.4. Domain containing parallel cylinders with thick membrane layer

4.4 Domain containing parallel cylinders with thick membrane layer

We come to the domain shown in Fig. 3.10(a), which contains a cylindrical cell ($R^c = 2.0\mu\text{m}$) with a thick membrane layer (thickness $h = 0.45\mu\text{m}$) outside it. There are three compartments: the extra-cellular compartment Ω^e , the intra-cellular compartment of the cylinder Ω^c and the membrane compartment Ω^m . Their volume fractions are respectively $v^e = 0.38$, $v^c = 0.41$ and $v^m = 0.21$.

4.4.1 Least squares problem on 4-parameters set

We choose the following 4-parameters set for the least squares problem in Eq. (4.5) and Eq. (4.6):

$$\mathcal{U} = \left\{ v^c, D_{\mathbf{g}}^e, \tau^{em}, \tau^{cm} \right\},$$

where $\tau^{em} \equiv \frac{|\Omega^m|}{\kappa|\Gamma^{em}|}$ and $\tau^{cm} \equiv \frac{|\Omega^m|}{\kappa|\Gamma^{cm}|}$. The constraints are:

$$\begin{aligned} \frac{\tau^{ij}}{\tau^{ji}} &= \frac{v^j}{v^i}, \forall i, j = e, m, c, \\ v^e + v^c + v^m &= 1, \\ 0 < D_{\mathbf{g}}^e &\leq D^0, \\ \overline{D}^m = \overline{D}^c &= 0, \text{ because } \Omega^m, \Omega^c \text{ are compact} \\ &\text{in the gradient direction (2D compact),} \\ 0 \leq v^e, v^m, v^c &\leq 1, \\ 0 \leq \tau^{em} \leq \tau^{cm}. \end{aligned} \tag{4.16}$$

Expecting that the surface between the extra-cellular compartment and the membrane, and the surface between the cylindrical compartment and the membrane, scale proportionally with the volume, we add one more constraint:

$$\left(\frac{|\Gamma^{cm}|}{|\Gamma^{em}|} \right)^2 = \frac{|\Omega^c|}{|\Omega^c| + |\Omega^m|}.$$

This constraint is equivalent to:

$$\left(\frac{\tau^{em}}{\tau^{cm}} \right)^2 = \frac{v^c}{v^c + v^m}. \tag{4.17}$$

The true model four-parameters set for this domain are:

$$\mathcal{U} = \left\{ v^c = 0.41, D_{\mathbf{g}}^e = 1.70 \times 10^{-3} \text{mm}^2/\text{s}, \tau^{em} = 41 \text{ms}, \tau^{cm} = 50 \text{ms} \right\}.$$

The initial guesses of the least squares problem are:

$$\mathcal{U}^0 = \left\{ c_v, \frac{D^0}{2}, c_{\tau_1} \tau_{true}^{em}, c_{\tau_2} \tau_{true}^{cm} \right\},$$

where c_v are varied in $[0, 1]$, c_{τ_1} and c_{τ_2} are varied in $[0, 2]$ to obtain different initial guesses.

For this domain, we did not see a significant difference in the parameters estimation results for v^s when c_v varied but we did notice that the estimated τ^{em} and τ^{cm}

changed when c_{τ_1} and c_{τ_2} varied. Thus, we varied c_{τ_1} and c_{τ_2} randomly to obtain 10 different initial guesses: $\mathcal{U}_i^0 (i = 1, \dots, 10)$. Then we compared the residuals of the solution of the least squares problem from the Matlab routine resulting from these 10 initial guesses and picked the one with the smallest residual as our estimated parameters set.

Table 4.4 summarizes the parameter estimations results. The estimated values for v^c and $D_{\mathbf{g}}^e$ are good. In turn, the estimated values for τ^{em} and τ^{cm} are less accurate but their ratio is still close to the true values due to condition in Eq. (4.17).

κ - PGSE	Parameter	\mathcal{U}^{true}	$(\mathcal{U}_{ODE}^{min})$	$(\mathcal{U}_{KAR}^{min})$
$\kappa = 1 \times 10^{-5} \text{m/s}$ $\delta = 80 \text{ms}$ $\Delta = 80 \text{ms}$	v^c	0.412	0.431	0.320
	τ^{em} (ms)	41	33	35
	τ^{cm} (ms)	50	40	50
	$D_{\mathbf{g}}^e$ ($\times 10^{-3} \text{mm}^2/\text{s}$)	1.70	1.79	1.87
	$R(\mathcal{U}^{min})$		0.00%	0.05%
	R^{mod}		1.8%	6.7%

Table 4.4: Estimated macroscopic model parameters for the domain containing parallel cylinders with thick membrane, $\kappa = 1 \times 10^{-5} \text{m/s}$, PGSE profile with $\delta = \Delta = 80 \text{ms}$.

4.4.2 Contour plots on 2-parameters sets

Now we make contour plots of 2-parameters sets to further investigate the properties of the parameters estimation problem for this domain. We fix two parameters at their true values and consider two remaining parameters as unknowns.

First we will study the 2-parameters set:

$$\mathcal{U} = \{v^c, D_{\mathbf{g}}^e\}, \quad \mathcal{U}^{known} = \{\tau^{em} = \tau_{true}^{em}, \tau^{cm} = \tau_{true}^{cm}\}, \quad (4.18)$$

where $\tau_{true}^{em} = 41 \text{ms}$, $\tau_{true}^{cm} = 50 \text{ms}$. And then we will study the 2-parameters set:

$$\mathcal{U} = \{\tau^{em}, \tau^{cm}\}, \quad \mathcal{U}^{known} = \left\{v^c = v_{true}^c, D_{\mathbf{g}}^e = \left(D_{\mathbf{g}}^e\right)_{true}\right\}, \quad (4.19)$$

where $v_{true}^c = 0.41$ and $\left(D_{\mathbf{g}}^e\right)_{true} = 1.7 \times 10^{-3} \text{mm}^2/\text{s}$.

Figure 4.11 presents the contour plots for both choices of \mathcal{U} above and the specific points for two 2-parameter sets:

1. Figures 4.11(a) and 4.11(b): $\mathcal{U}_{true} = \{v^c = 0.41, D_{\mathbf{g}}^e = 1.70 \times 10^{-3} \text{mm}^2/\text{s}\}$;
 $\mathcal{U}_{ODE}^{min} = \{0.40, 1.69 \times 10^{-3} \text{mm}^2/\text{s}\}$; $\mathcal{U}_{KAR}^{min} = \{0.36, 1.38 \times 10^{-3} \text{mm}^2/\text{s}\}$.
2. Figures 4.11(c) and 4.11(d): $\mathcal{U}_{true} = \{\tau^{em} = 41 \text{ms}, \tau^{cm} = 50 \text{ms}\}$;
 $\mathcal{U}_{ODE}^{min} = \{38 \text{ms}, 46 \text{ms}\}$; $\mathcal{U}_{KAR}^{min} = \{39 \text{ms}, 45 \text{ms}\}$.

The contours show that we can easily get a good approximation for v^c and $D_{\mathbf{g}}^e$ by using the ODE model because its \mathcal{U}_{ODE}^{min} is very close to \mathcal{U}_{true} , while \mathcal{U}_{KAR}^{min} is not close to \mathcal{U}_{true} . However, we can see clearly from Fig. 4.11(c) and Fig. 4.11(d) that it is very difficult to estimate τ^{em} and τ^{cm} because the contours stretch very long

4.4. Domain containing parallel cylinders with thick membrane layer

along the lines describing the true ratio between τ^{em} and τ^{cm} . This explains why we could not get good estimates of τ^{em} and τ^{cm} when we solved the least squares problem on the 4-parameters set previously.

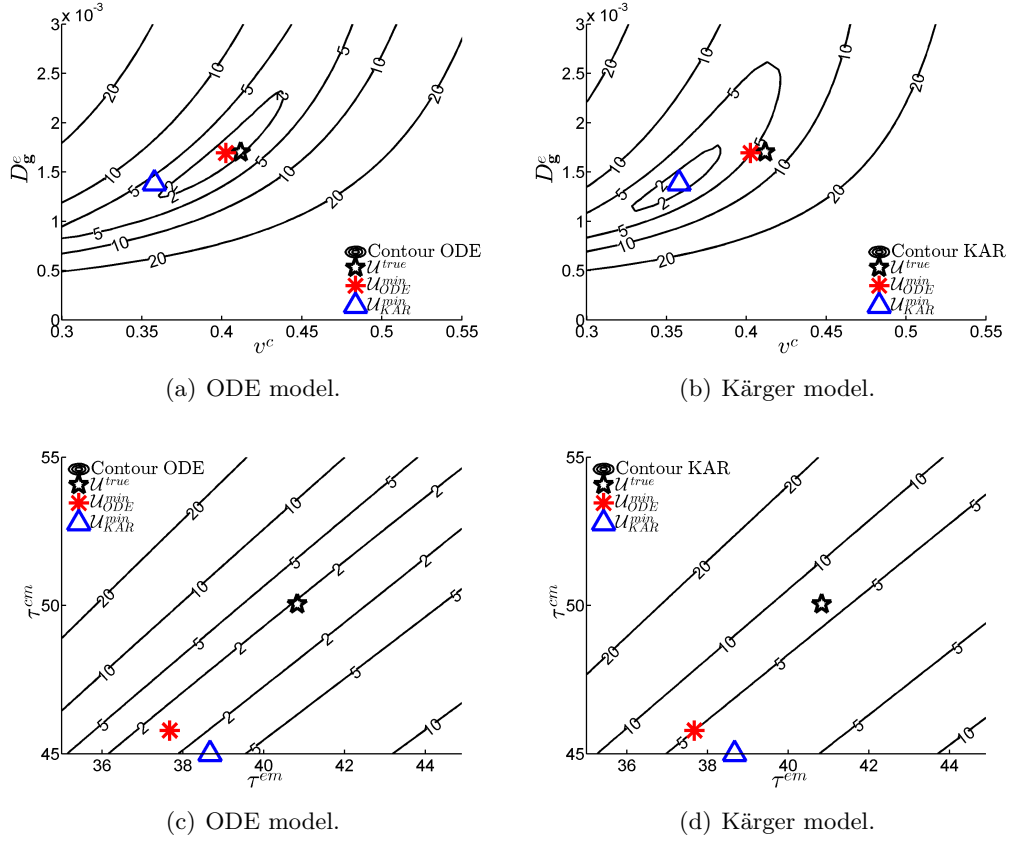


Figure 4.11: Domain containing parallel cylinders with thick membrane, $\kappa = 10^{-5}$ m/s, PGSE profile with $\delta = \Delta = 80$ ms (a,b) v^s and D_g^e , (c,d) τ^{em} and τ^{cm} .

R^{mod} : (a,c) 1.8%, (b,d) 6.7%;

$R_{ODE}(U_{ODE}^{min})$: (a,b) 1.3%, (c,d) 0.1%; $R_{KAR}(U_{KAR}^{min})$: (a,b) 3.9%, (c,d) 2.3%.

4.5 Domain containing slanted parallel cylinders

In the previous section, the gradient direction was set perpendicular to the cylinder axis in order to probe restricted diffusion in the cross-sectional plane. This allowed us to deal with isotropic diffusion. The next step consists in considering anisotropic diffusion on the domain shown in Fig. 3.9(a), which contains slanted cylinders that all lie parallel to the $x - y$ -plane, make an angle $\pi/3$ with the x -axis, and have a radius $R^c = 2.35\mu\text{m}$. This is also equivalent to setting the gradient in an intermediate direction between the cylinder axis and the cross-sectional plane. For the sake of simplicity, we consider only two compartments: the extra-cellular compartment Ω^e , and the intra-cellular compartment Ω^c of cylinders (i.e., there is no membrane compartment). Their volume fractions are $v^e = 0.31$ and $v^c = 0.69$, respectively.

In order to describe anisotropic diffusion in the long time limit, one needs to introduce two effective diffusion tensors, \overline{D}^e and \overline{D}^c , for both compartments.

Each diffusion tensor has to 6 unknown parameters so that one formally gets the following 14-parameters set for the least squares problem:

$$\mathcal{U} = \{v^c, \overline{D}^e, \overline{D}^c, \tau^{ec}\},$$

where $\tau^{ec} \equiv \frac{|\Omega^c|}{\kappa|\Gamma^{ec}|}$. One also needs at least 6 different gradient directions to estimate the effective diffusion tensors. The constraints for this domain are:

$$\begin{aligned} \frac{\tau^{ec}}{\tau^{ce}} &= \frac{v^c}{v^e}, \\ v^e + v^c &= 1, \\ 0 < \overline{D}_{ij}^c, \overline{D}_{ik}^e &\leq D^0, \forall i, j = 1, \dots, 3, \\ 0 &\leq v^e, v^c \leq 1, \\ 0 &\leq \tau^{ec}. \end{aligned} \tag{4.20}$$

A numerical solution of this optimization problem for 14 unknowns may be highly unstable. In order to investigate the stability of this problem, we focus on the contour plots on 2-parameters sets. For this purpose, we fix three gradient directions,

1. $\mathbf{g}_1 = (0.5, 0, 0.87)$: parallel to the axis of cylinders,
2. $\mathbf{g}_2 = (0.87, 0, -0.5)$: perpendicular to the axis of cylinders,
3. $\mathbf{g}_3 = (0.97, 0, 0.26)$: lying in the middle of \mathbf{g}_1 and \mathbf{g}_2 ,

and consider the effective diffusion tensors \overline{D}^e and \overline{D}^c projected onto these directions. In other words, we will estimate the effective diffusion coefficients $D_{\mathbf{g}}^c$ and $D_{\mathbf{g}}^e$ as previously.

We consider two choices of a 2-parameters set. The first choice is

$$\mathcal{U} = \{D_{\mathbf{g}}^c, D_{\mathbf{g}}^e\}, \quad \mathcal{U}^{known} = \{v^c = v_{true}^c, \tau^{ec} = \tau_{true}^{ec}\}, \tag{4.21}$$

4.5. Domain containing slanted parallel cylinders

where $v_{true}^c = 0.69$, $\tau_{true}^{ec} = 116\text{ms}$, while the second choice is

$$\mathcal{U} = \{v^c, \tau^{es}\}, \quad \mathcal{U}^{known} = \left\{ D_{\mathbf{g}}^c = \left(D_{\mathbf{g}}^c \right)_{true}, D_{\mathbf{g}}^e = \left(D_{\mathbf{g}}^e \right)_{true} \right\}, \quad (4.22)$$

where $\left(D_{\mathbf{g}}^c \right)_{true}$ and $\left(D_{\mathbf{g}}^e \right)_{true}$ are their true values for three prescribed gradient directions \mathbf{g} . The remaining parameters are set at their true values.

Figure 4.12 shows the contour plots for both choices of \mathcal{U} above in three different gradient directions [their signals are shown in Fig. 3.9(b)]. One can notice the following specific points for the first 2-parameters set:

1. $\mathbf{g}_1 = (0.5, 0, 0.87)$ (Fig. 4.12(a)):
 - $\mathcal{U}_{true} = \{D_{\mathbf{g}}^c = 3.00 \times 10^{-3}\text{mm}^2/\text{s}, D_{\mathbf{g}}^e = 3.00 \times 10^{-3}\text{mm}^2/\text{s}\};$
 - $\mathcal{U}_{ODE}^{min} = \{3.04 \times 10^{-3}\text{mm}^2/\text{s}, 2.98 \times 10^{-3}\text{mm}^2/\text{s}\};$
 - $\mathcal{U}_{KAR}^{min} = \{2.98 \times 10^{-3}\text{mm}^2/\text{s}, 3.01 \times 10^{-3}\text{mm}^2/\text{s}\}.$
2. $\mathbf{g}_2 = (0.87, 0, -0.5)$ (Fig. 4.12(c)):
 - $\mathcal{U}_{true} = \{D_{\mathbf{g}}^c = 0.00 \times 10^{-3}\text{mm}^2/\text{s}, D_{\mathbf{g}}^e = 1.52 \times 10^{-3}\text{mm}^2/\text{s}\};$
 - $\mathcal{U}_{ODE}^{min} = \{0.02 \times 10^{-3}\text{mm}^2/\text{s}, 1.56 \times 10^{-3}\text{mm}^2/\text{s}\}; \mathcal{U}_{KAR}^{min} = \{0.06 \times 10^{-3}\text{mm}^2/\text{s}, 1.49 \times 10^{-3}\text{mm}^2/\text{s}\}.$
3. $\mathbf{g}_3 = (0.97, 0, 0.26)$ (Fig. 4.12(e)):
 - $\mathcal{U}_{true} = \{D_{\mathbf{g}}^c = 1.51 \times 10^{-3}\text{mm}^2/\text{s}, D_{\mathbf{g}}^e = 2.27 \times 10^{-3}\text{mm}^2/\text{s}\};$
 - $\mathcal{U}_{ODE}^{min} = \{1.51 \times 10^{-3}\text{mm}^2/\text{s}, 2.26 \times 10^{-3}\text{mm}^2/\text{s}\};$
 - $\mathcal{U}_{KAR}^{min} = \{1.54 \times 10^{-3}\text{mm}^2/\text{s}, 2.21 \times 10^{-3}\text{mm}^2/\text{s}\}.$

and for the second 2-parameters set:

1. $\mathbf{g}_1 = (0.5, 0, 0.87)$ (Fig. 4.12(b)): $\mathcal{U}_{true} = \{v^s = 0.69, \tau^{es} = 116\text{ms}\};$
 $\mathcal{U}_{ODE}^{min} = \{0.50, 148\text{ms}\}; \mathcal{U}_{KAR}^{min} = \{0.50, 200\text{ms}\}.$
2. $\mathbf{g}_2 = (0.87, 0, -0.5)$ (Fig. 4.12(d)): $\mathcal{U}_{true} = \{v^s = 0.69, \tau^{es} = 116\text{ms}\};$
 $\mathcal{U}_{ODE}^{min} = \{0.67, 104\text{ms}\}; \mathcal{U}_{KAR}^{min} = \{0.67, 62\text{ms}\}.$
3. $\mathbf{g}_3 = (0.97, 0, 0.26)$ (Fig. 4.12(f)): $\mathcal{U}_{true} = \{v^s = 0.69, \tau^{es} = 116\text{ms}\};$
 $\mathcal{U}_{ODE}^{min} = \{0.68, 154\text{ms}\}; \mathcal{U}_{KAR}^{min} = \{0.68, 98\text{ms}\}.$

These contour plots provide useful information about the stability and quality of parameters estimation. For the parallel gradient direction \mathbf{g}_1 , diffusion is fast along the cylinder axis so that it is easy to estimate $D_{\mathbf{g}}^c$ and $D_{\mathbf{g}}^e$ (Fig. 4.12(a)) but impossible to estimate v^c and τ^{es} (Fig. 4.12(b)). In fact, the contour plots on Fig. 4.12(b) do not exhibit a distinguishable minimum. This is not surprising because the exchange between two compartments happens in the cross-sectional plane, while the signal probes diffusion along the cylinder axis.

For the perpendicular gradient direction \mathbf{g}_2 , diffusion is fast in the extra-cellular compartment and could be considered effectively zero in the compact intra-cellular compartment. As a consequence, the \mathcal{U}_{ODE}^{min} are close to \mathcal{U}_{true} for both 2-parameters set. The estimation of $D_{\mathbf{g}}^c$ (whose true value is zero in the long-time limit) is not

accurate because of the finite diffusion time (i.e., the infinite diffusion limit is not reached). In turn, the estimation of $D_{\mathbf{g}}^e$ is quite accurate.

Finally, for the intermediate gradient direction \mathbf{g}_3 , one faces the same problem as for the first case \mathbf{g}_1 but to a lesser extent. Although Fig. 4.12(e) suggests that the estimates of $D_{\mathbf{g}}^c$ and $D_{\mathbf{g}}^e$ from the ODE and Kärger models are close to their true values, the contour plots are strongly stretched in the vertical direction. It means that an estimate of $D_{\mathbf{g}}^e$ may be highly unstable and biased by noise. As earlier for the first case \mathbf{g}_1 , the estimation of τ^{ec} is impossible as no minimum is present on Fig. 4.12(f). Although the estimates of v^c from both the ODE and Kärger models are close to its true value, the presence of noise may strongly alter this procedure.

We conclude that parameters estimation for both the ODE and Kärger models in the case of anisotropic diffusion is much more challenging than for the isotropic case. In fact, one needs to carefully choose gradient directions in order to get stable estimates. In general, the situation is even more complex as highly extended structures (like cylinders here, e.g., axons) may be randomly oriented and well mixed with compact structures (e.g., glial cells). We consider an example of such situation in the next section.

4.5. Domain containing slanted parallel cylinders

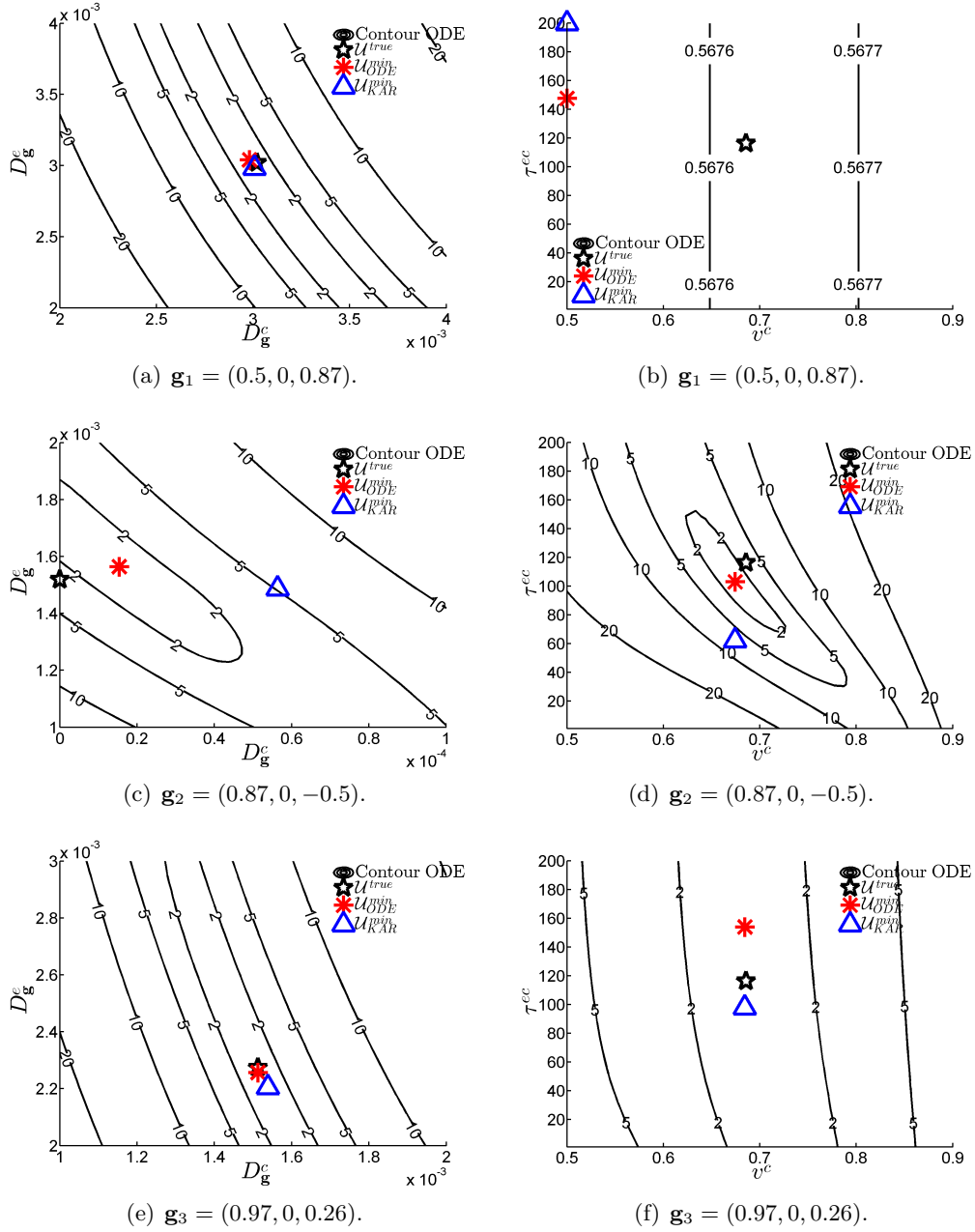


Figure 4.12: Domain containing slanted parallel cylinders, $\kappa = 10^{-5}$ m/s, PGSE with $\delta = \Delta = 80$ ms, contour plots for the ODE model.

R^{mod} : (a,b) 0.8%, (c,d) 3.8% , (e,f) 0.2%;

$R_{ODE}(U_{ODE}^{min})$: (a) 0.01%, (b) 0.57%, (c) 0.16%, (d) 0.17% , (e) 0.05%, (f) 0.05%;

$R_{KAR}(U_{KAR}^{min})$: (a) 0.01%, (b) 0.57%, (c) 0.14%, (d) 0.35% , (e) 0.05%, (f) 0.05%.

4.6 Domain containing spheres and deformed cylinders

Finally, we test the parameters estimation technique on our most complicated domain containing 5 layers of deformed cylinders (cylinder radius $R^c = 1.0\mu\text{m}$) lying parallel to the $x - y$ plane and 4 layers of spherical cells (sphere radius $R^s = 1.375\mu\text{m}$) all embedded in the extra-cellular space as shown in Fig. 3.11(a). This domain can be considered as having 7 compartments: the extra-cellular space (Ω^e), the compartment formed by the union of 4 layers of 16 spherical cells (Ω^s), and 5 compartments consisting of the cylinders with the same orientation ($\Omega^{c_1}, \dots, \Omega^{c_5}$). In each layer of cylinders, the orientations of the cylinders are the same. Their volume fractions are $v^e = 0.48$, $v^s = 0.21$, and we consider that all cylinder layers have the same average volume fraction $v^{c_k} = v^c = 0.06$ ($k = 1, \dots, 5$), the same residence times of exchanging with extra-cellular compartment $\tau^{ec_k} = \tau^{ec} = 53\text{ms}$ ($k = 1, \dots, 5$), and the same residence times of exchanging with sphere compartment $\tau^{sc_k} = \tau^{sc} = 307\text{ms}$ ($k = 1, \dots, 5$). The intrinsic diffusion coefficient is $D^0 = 3 \times 10^{-3}\text{mm}^2/\text{s}$, permeability is $\kappa = 1 \times 10^{-5}\text{m/s}$, we use PGSE sequences with $\delta = \Delta = 40\text{ms}$ for all gradient directions.

Because of the complex structure of the domain, we simplify the problem by assuming that we already knew the orientations of all 5 layers: 0, 26.5, 45, 63.5 and 90 degrees, respectively, from the x -axis, which means that we knew all their diffusion coefficients $D_{\mathbf{g}}^{c_k}, k = 1, \dots, 5$ by using Eq. (2.30). The constraints are:

$$\begin{aligned}
 \frac{\tau^{lm}}{\tau^{ml}} &= \frac{v^m}{v^l}, \quad l, m = e, s, c, \\
 v^e + v^s + 5v^c &= 1, \\
 0 < D_{\mathbf{g}}^e &\leq D^0, \\
 \overline{D}^s &= 0, \quad \text{because } \Omega^s \text{ is compact,} \\
 D_{\mathbf{g}}^{c_k} &= (D_{\mathbf{g}}^{c_k})_{\text{true}}, \quad k = 1, \dots, 5 \\
 0 \leq v^e, v^s &\leq 1, \\
 0 \leq \tau^{sc}, \tau^{ec}, \tau^{es}. &
 \end{aligned} \tag{4.23}$$

In order to investigate the stability of the parameters estimation procedure, we consider three choices of 2-parameters sets:

$$\begin{aligned}
 \mathcal{U} &= \{v^e, D_{\mathbf{g}}^e\}, \\
 \mathcal{U} &= \{v^s, \tau^{sc}\}, \\
 \mathcal{U} &= \{\tau^{ec}, \tau^{es}\},
 \end{aligned}$$

where three gradient directions were used for $D_{\mathbf{g}}^e$: $\mathbf{g}_1 = (1, 0, 0)$, $\mathbf{g}_2 = (1, 0, 1)$ and $\mathbf{g}_3 = (1, 1, 1)$. For each choice, the remaining parameters $\mathcal{U}^{\text{known}}$ are set at their true values.

Figure 4.13 shows the contour plot for all three 2-parameters sets in three gradient directions. One can notice the following specific points for first 2-parameters choice:

1. $\mathbf{g}_1 = (1, 0, 0)$ (Fig. 4.13(a)): $\mathcal{U}_{\text{true}} = \{v^e = 0.48, D_{\mathbf{g}}^e = 2.29 \times 10^{-3}\text{mm}^2/\text{s}\}$;
 $\mathcal{U}_{ODE}^{\text{min}} = \{0.52, 2.22 \times 10^{-3}\text{mm}^2/\text{s}\}$; $\mathcal{U}_{KAR}^{\text{min}} = \{0.69, 2.00 \times 10^{-3}\text{mm}^2/\text{s}\}$;

4.6. Domain containing spheres and deformed cylinders

2. $\mathbf{g}_2 = (1, 0, 1)$ (Fig. 4.13(d)): $\mathcal{U}_{true} = \{v^e = 0.48, D_{\mathbf{g}}^e = 2.42 \times 10^{-3} \text{mm}^2/\text{s}\}$;
 $\mathcal{U}_{ODE}^{min} = \{0.39, 2.46 \times 10^{-3} \text{mm}^2/\text{s}\}$; $\mathcal{U}_{KAR}^{min} = \{0.30, 3.00 \times 10^{-3} \text{mm}^2/\text{s}\}$;
3. $\mathbf{g}_3 = (1, 1, 1)$ (Fig. 4.13(g)): $\mathcal{U}_{true} = \{v^e = 0.48, D_{\mathbf{g}}^e = 2.30 \times 10^{-3} \text{mm}^2/\text{s}\}$;
 $\mathcal{U}_{ODE}^{min} = \{0.39, 2.50 \times 10^{-3} \text{mm}^2/\text{s}\}$; $\mathcal{U}_{KAR}^{min} = \{0.34, 3.00 \times 10^{-3} \text{mm}^2/\text{s}\}$;

Next, specific points for the second 2-parameters choice:

1. $\mathbf{g}_1 = (1, 0, 0)$ (Fig. 4.13(b)): $\mathcal{U}_{true} = \{v^s = 0.21, \tau^{sc} = 307 \text{ms}\}$;
 $\mathcal{U}_{ODE}^{min} = \{0.21, 175 \text{ms}\}$; $\mathcal{U}_{KAR}^{min} = \{0.19, 100 \text{ms}\}$.
2. $\mathbf{g}_2 = (1, 0, 1)$ (Fig. 4.13(e)): $\mathcal{U}_{true} = \{v^s = 0.21, \tau^{sc} = 307 \text{ms}\}$;
 $\mathcal{U}_{ODE}^{min} = \{0.21, 222 \text{ms}\}$; $\mathcal{U}_{KAR}^{min} = \{0.19, 107 \text{ms}\}$.
3. $\mathbf{g}_3 = (1, 1, 1)$ (Fig. 4.13(h)): $\mathcal{U}_{true} = \{v^s = 0.21, \tau^{sc} = 307 \text{ms}\}$;
 $\mathcal{U}_{ODE}^{min} = \{0.21, 208 \text{ms}\}$; $\mathcal{U}_{KAR}^{min} = \{0.19, 100 \text{ms}\}$.

And specific points for the third 2-parameters choice:

1. $\mathbf{g}_1 = (1, 0, 0)$ (Fig. 4.13(c)): $\mathcal{U}_{true} = \{\tau^{ec} = 53 \text{ms}, \tau^{es} = 57 \text{ms}\}$;
 $\mathcal{U}_{ODE}^{min} = \{81 \text{ms}, 46 \text{ms}\}$; $\mathcal{U}_{KAR}^{min} = \{38 \text{ms}, 30 \text{ms}\}$.
2. $\mathbf{g}_2 = (1, 0, 1)$ (Fig. 4.13(f)): $\mathcal{U}_{true} = \{\tau^{ec} = 53 \text{ms}, \tau^{es} = 57 \text{ms}\}$;
 $\mathcal{U}_{ODE}^{min} = \{28 \text{ms}, 54 \text{ms}\}$; $\mathcal{U}_{KAR}^{min} = \{25 \text{ms}, 30 \text{ms}\}$.
3. $\mathbf{g}_3 = (1, 1, 1)$ (Fig. 4.13(i)): $\mathcal{U}_{true} = \{\tau^{ec} = 53 \text{ms}, \tau^{es} = 57 \text{ms}\}$;
 $\mathcal{U}_{ODE}^{min} = \{85 \text{ms}, 52 \text{ms}\}$; $\mathcal{U}_{KAR}^{min} = \{31 \text{ms}, 30 \text{ms}\}$.

Since the present domain is truly anisotropic (without a selected direction as it was the case for slanted parallel cylinders), the contours for three gradient directions are very similar. In the contour plots of v^e and $D_{\mathbf{g}}^e$ (the first column, Fig. 4.13(a), 4.13(d), 4.13(g)), one can see that these two parameters can be estimated. The quality of the estimation slightly depends on the gradient direction. In practice, one can acquire signals in different directions and then combine them to get more accurate estimates. As usual, the ODE model provides more accurate estimates than the Kärger model. On the contrary, the contour plots of v^s and τ^{sc} (second column) and contour plots of τ^{ec} and τ^{es} (third column) exhibit very stretched patterns and no distinguishable minima. As a consequence, the estimation of the parameters τ^{sc} (the vertical axis in the second column) and τ^{ec} (the horizontal axis in the third column) is impossible. The absence of a well localized minimum does not allow to conclude, from these plots, about the stability of estimates of the other parameters v^s and τ^{es} . This conclusion is not surprising. For instance, the residence time τ^{ec} characterizes the exchange between the cylindrical and extra-cellular compartments. When the gradient direction is close to the cylinder axis, the signal does not contain enough information about the exchange, as we discussed earlier. Similarly, the residence time τ^{sc} that characterizes the exchange between deformed cylinders and spheres across their common interface is not accessible.

Chapter 4. Parameters estimation using macroscopic dMRI signal models

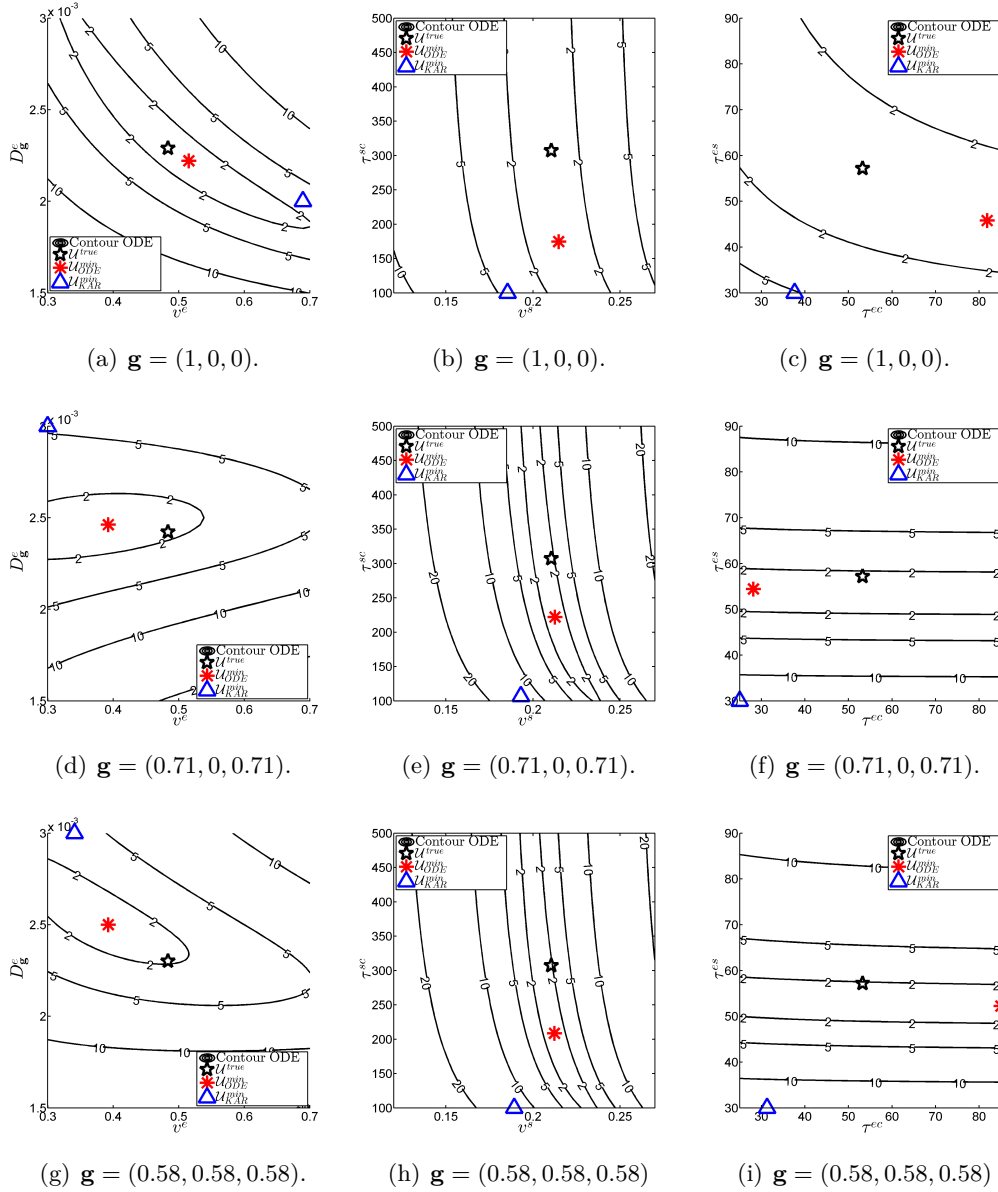


Figure 4.13: Spherical and cylindrical cells, $\kappa = 10^{-5}$ m/s, PGSE with $\delta = \Delta = 40$ ms: (a,d,g) v^e and $D_{\mathbf{g}}^e$, (b,e,h) v^s and τ^{sc} , (c,f,i) τ^{ec} and τ^{es} .

R^{mod} : (a,b,c) 0.4%, (d,e,f) 1.5%, (g,h,i) 1.8%

$R_{ODE}(U_{ODE}^{min})$: (a) 0.1%, (b) 0.06%, (c) 0.09%, (d) 0.2%, (e) 0.2%, (f) 0.2%, (g) 0.3%, (h) 0.2%, (i) 0.2%;

$R_{KAR}(U_{KAR}^{min})$: (a) 0.5%, (b) 0.4%, (c) 1.1%, (d) 10.9%, (e) 6.7%, (f) 6.0%, (g) 12.9%, (h) 0.8%, (i) 7.5%.

4.7 Conclusions and further improvements

Our analysis of the parameters estimation problem in the previous sections has revealed advantages and limitations of this approach. On the one hand, it seems to be possible to estimate a number of physiologically relevant parameters for “simple” tissues composed of not too elongated constituents. Among these parameters are the volume fractions, the apparent diffusion coefficient in the extra-cellular space, and the residence time which is related to the membrane permeability and surface-to-volume ratio. Clearly, these parameters can only represent averaged properties of the tissue. Nevertheless, a reliable experimental determination of these parameters has always presented a great challenge. We showed on simplified examples a possibility of solving the parameters estimation problem. Most importantly, we analyzed the stability features of this problem. In particular, we studied the robustness of the estimates against various biological and physical parameters (e.g., permeability, sequence timing, the range and number of b-values), as well as the robustness against noise. The ODE model always provided more accurate and stable estimates than the Kärger model. This study suggests a promising perspective for estimating many important parameters from dMRI signals.

At the same time, we analyzed the parameters estimation problem for more complicated domains which contain very elongated constituents (infinite cylinders). As expected, if the gradient is precisely aligned with the cylinder axis, one deals with unrestricted diffusion so that no information on the exchange can be extracted. But the quality of parameters estimation is dramatically reduced even for intermediate gradient directions. In other words, one needs to apply the gradient in (almost) perpendicular direction to ensure accurate estimates. This is a natural limitation of the parameters estimation procedure because biological tissues may contain elongated structures randomly oriented and also mixed with other (compact) elements (e.g., axons and glial cells). The quality of the parameters estimation may potentially be improved by acquiring signals in various directions and then fitting all these signals to the appropriate ODE models.

Another interesting perspective for future investigation consists in including additional constraints to the optimization problem. These constraints may account for some relationships between model parameters. In order to illustrate this point, we will get a relationship between v^c and $D_{\mathbf{g}}^e$ by performing simulations in simple shapes. Another simple analytical relationship exists between v^c and τ^{es} .

We first examine the relationship between v^c and $D_{\mathbf{g}}^e$ for two simple domains, namely, periodic lattices of two-dimensional cells of circular (Fig. 4.14(a)) and square (Fig. 4.14(b)) shapes. This is also equivalent to consider aligned cylinders (as shown in Fig. 3.10(a)) and apply the gradient perpendicularly to the cylinder axis. For each shape, we varied the cell radius R^c and the inter-cellular distance L^c in the following ranges:

$$R^c \in [2.3 : 0.01 : 2.6], \quad L^c \in [5.3 : 0.01 : 5.7]. \quad (4.24)$$

As a result, we produced $31 \times 41 = 1271$ domains, for both circular and square shapes. The volume fraction of the extra-cellular compartment v^c varied in the

range $[0.5, 0.75]$ for the circular shape and in the range $[0.65, 0.97]$ for the square shape.

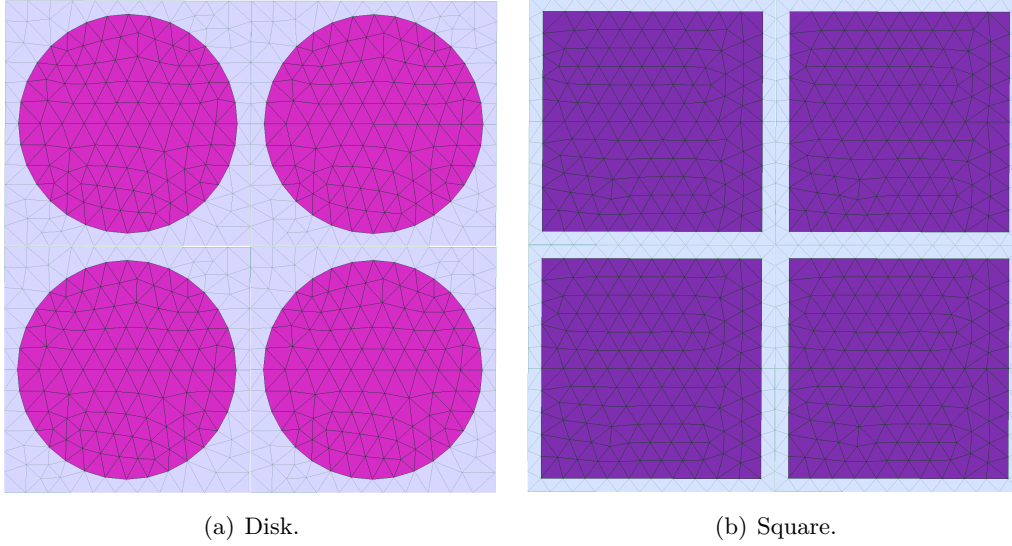


Figure 4.14: Circular (a) and square (b) shapes of two-dimensional cells which are formed into periodic lattices.

For each of these domains, we computed $D_{\mathbf{g}}^e$ by solving steady-state Laplace equation (2.25) (the intrinsic diffusion coefficient was set to $D^0 = 3 \times 10^{-3} \text{mm}^2/\text{s}$). The obtained values of $D_{\mathbf{g}}^e$ are plotted versus the corresponding volume fraction v^c in Fig. 4.14. In this way, we obtain numerically the relationship between $D_{\mathbf{g}}^e$ on v^c . One can see that this relationship turns out to be a curve, despite the fact that the values of $D_{\mathbf{g}}^e$ come from different R^c and L^c . We conclude that with fixed D^0 , the effective diffusion coefficient $D_{\mathbf{g}}^e$ of the extra-cellular compartment depends almost exclusively on v^c although this dependence is different for each shape.

Now we consider the relationship between v^c and τ^{ec} . For circular cells, one has

$$v^c = \frac{\pi(R^c)^2}{(L^c)^2}; \quad \tau^{ec} = \frac{|\Omega^c|}{|\Gamma^{ec}|\kappa} = \frac{R^c}{2\kappa};$$

from which

$$\tau^{ec} = \frac{\sqrt{v^c}L}{2\sqrt{\pi}\kappa}. \quad (4.25)$$

Similarly, one gets for square shapes:

$$\tau^{ec} = \frac{\sqrt{v^c}L}{4\kappa}. \quad (4.26)$$

These formulas show that, in addition to v^c and κ , one needs to know the cell distance L to identify the value of τ^{ec} .

4.7. Conclusions and further improvements

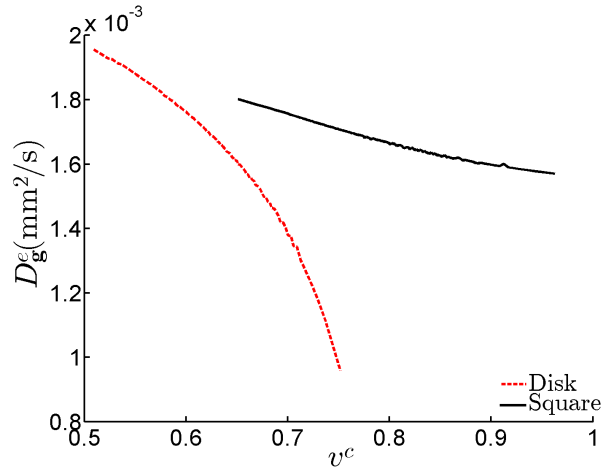


Figure 4.15: Relationship between v^c and D_g^e obtained by numerical solution of the steady-state Laplace equations for circular and square shapes.

Adding these supplementary constraints means finding the minimum of the contour plots in Fig. 4.16 along the constraint curve. As a consequence, one can get much better parameter estimations because the distance from the least squares solution with additional constraints (called $(U_{ODE}^{min})^{add}$) to U^{true} is smaller than the distance from U_{ODE}^{min} to U^{true} , as one can see both in Fig. 4.16(a) for the set $\{v^c, D_g^e\}$, and in Fig. 4.16(b) for the set $\{v^c, \tau^{es}\}$. This example illustrates that further analysis of relationships between unknown model parameters may significantly improve parameters estimations using macroscopic models.

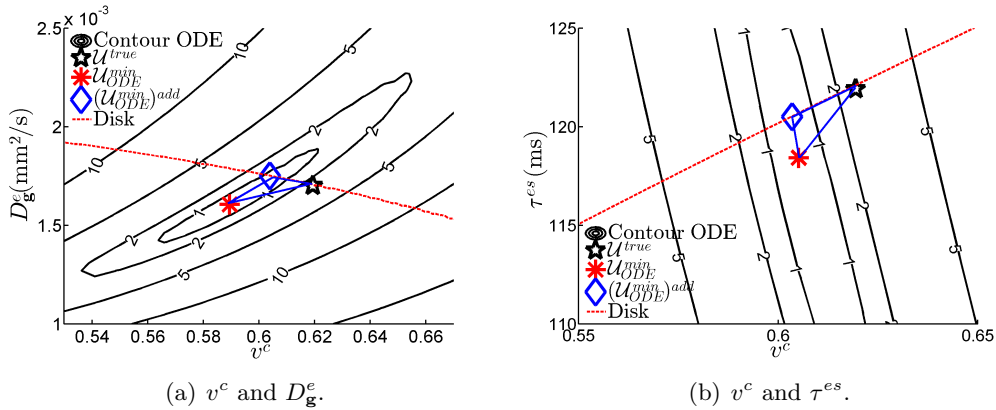


Figure 4.16: Contour plot of the ODE model for circular shapes with respect to v^c and D_g^e (a), and v^c and τ^{es} (b).

Conclusions and future directions

Conclusions

This thesis has been focused on the relationship between the tissue microstructure and the macroscopic dMRI signal. Inferring tissue parameters from experimentally measured signals is considered as the “Holy Grail” of diffusion MRI. In spite of a long standing history of intensive research in this field, many aspects of this inverse problem remain poorly understood. We proposed and tested an approximate solution to this problem, in which the dMRI signal is first approximated by an appropriate macroscopic model and then the effective parameters of this model are estimated.

We investigated two macroscopic models of the dMRI signal. The first is the Kärger model that assumes a certain form of (macroscopic) multiple compartmental diffusion and inter-compartment exchange, but is subject to the narrow pulse restriction on the diffusion-encoding magnetic field gradient pulses. The second is an ODE model of the multiple compartment magnetizations obtained from mathematical homogenization of the Bloch-Torrey equation, that is not subject to the narrow pulse restriction. In both models, the dMRI signal has been related to model parameters that represent averaged quantities over the voxel.

First, we investigated the validity of these macroscopic models by comparing the dMRI signal given by the Kärger and the ODE models with the dMRI signal simulated on some relatively complex tissue geometries by solving the microscopic Bloch-Torrey equation in the presence of semi-permeable biological cell membranes. We note that the Kärger model is a limit case of the ODE model where the duration of the diffusion-encoding magnetic field gradient pulses goes to zero. We concluded that the validity of both macroscopic models is limited to the case where diffusion in each compartment is effectively Gaussian and where the inter-compartmental exchange can be accounted for by standard first-order kinetic terms.

Second, assuming that the above conditions on the compartmental diffusion and inter-compartment exchange are satisfied, we solved the least squares problem associated with fitting the Kärger and the ODE model parameters to the simulated dMRI signal obtained by solving the microscopic Bloch-Torrey equation. Among various effective parameters, we considered the volume fractions of the intra-cellular and extra-cellular compartments (which may change during cell swelling), membrane permeability (which may characterize, to some extent, normal or abnormal functioning of cells), average size of cells, inter-cellular distance, as well as apparent diffusion coefficients. We started by studying the feasibility of the least squares solution for two groups of relatively simple tissue geometries. For the first group, in which domains consist of identical or variably-sized spherical cells embedded in

the extra-cellular space, we concluded that parameters estimation problem can be robustly solved, even in the presence of noise. In the second group, we considered parallel cylindrical cells, which may be covered by a thick membrane layer, and embedded in the extra-cellular space. When the diffusion gradient is applied perpendicularly to the cylinder axis, the parameter estimation problem can be robustly solved, just as for spherical cells. In the opposite case of the diffusion gradient parallel to the axis cylinder, one simply probes unrestricted diffusion which contains no information about the restricting domain and water exchange between compartments. As a consequence, the parameter estimation fails in this situation. For an intermediate gradient direction, the quality of parameter estimation strongly depends on how much the cellular structure is elongated in the gradient direction. In practice, the orientation of elongated cells is not known a priori; moreover, biological tissues may contain elongated structures randomly oriented and also mixed with other (compact) elements (e.g., axons and glial cells). This situation has been numerically investigated on our most complicated domain in which layers of cylindrical cells in various directions are mixed with layers of spherical cells. We checked that certain parameters can still be estimated rather accurately while the other remain inaccessible. In all considered cases, the ODE model provided more accurate estimates than the Kärger model.

Future directions

In this thesis, we have shown by numerical simulations that if the voxel is made up of spatial sub-domains that are separated from each other by low permeability membranes and if diffusion in the sub-domains are (close to) Gaussian, then the macroscopic ODE model of the dMRI signal (and the Kärger model, if the gradient profile is narrow pulse) is a good approximation to the microscopic Bloch-Torrey PDE model. However, for a generic voxel, it is expected that there would be spatial variations within the diffusion compartments on the length scale of the voxel. For example, we would expect that the extra-cellular space, being tortuous, would not, in general, be able to be described by a constant effective diffusion tensor on the length scale of the entire voxel. Nevertheless, it is still important to use the insight gained by the macroscopic models studied in this thesis, in particular, the ODE model that was derived by explicitly taking into account the discontinuity in the magnetization across the biological cell membranes. Specifically, the ODE model was derived using different expansions of the PDE solution in each compartment, matching them via the interface conditions.

A number of practical improvements can be suggested as perspectives. When the tissue is composed of elongated structures (e.g., axons), the parameters estimation fails if the gradient is close to the axis of these structures. The quality of the parameters estimation can be improved by acquiring signals in various directions and then fitting all these signals to the appropriate ODE models. To some extent, this is similar to acquisition of effective diffusion tensors for anisotropic diffusion when one needs many gradient directions to get accurate results. Another promising perspec-

4.7. Conclusions and further improvements

tive consists in studying relationships between different parameters of the model. For instance, the effective diffusion coefficient in the extra-cellular compartment and the residence times can be explicitly related to volume fractions, at least for simple shapes. Accounting for such relations as additional constraints in the least square problem would improve the parameters estimation by reducing the search region in the parameters space. Yet another possibility is to go beyond effective diffusion coefficients by considering higher-order cumulants such as the effective diffusion kurtosis. This quantity appears in front of the second-order term in the Taylor series expansion of the logarithm of the dMRI signal over b-values. It has been already argued that the kurtosis may be more sensitive to certain microstructure alterations. However, theoretical understanding of the relationship between the kurtosis and the tissue microstructure is still poor. Finding relations between the kurtosis and model parameters and their inclusion into the least square estimation present an interesting perspective of the present study.

List of publications

1. D. S. Grebenkov, H. T. Nguyen, and J.-R. Li, "A fast random walk algorithm for computing diffusion-weighted NMR signals in multiscale porous media: a feasibility study for a Menger sponge," *Microporous and Mesoporous Materials*, Volume 178, 2013, Pages 56-59.
2. H. T. Nguyen, J.-R. Li, D. S. Grebenkov, D. Le Bihan and C. Poupon, "Parameters estimation from the diffusion MRI signal using a macroscopic model," *IC-MSQUARE 2013*. Open Access Journal of Physics: IOP Conference Series. (Accepted).
3. J.-R. Li, H. T. Nguyen, D. V. Nguyen, H. Haddar, J. Coatléven and D. Le Bihan, "Numerical study of a macroscopic ODE model of the diffusion MRI signal," (About to be submitted).
4. H. T. Nguyen, J.-R. Li, D. S. Grebenkov, D. Le Bihan, and C. Poupon, "Parameters estimation using macroscopic dMRI signal models," (In preparation).

List of presentations

1. "New ODE Model for Diffusion MRI Signal," Magnetic Resonance in Porous Media 11 (MRPM11), Surrey - United Kingdom, 09/2012 (Poster Presentation).
2. "Parameters estimation from the diffusion MRI signal using a macroscopic model," International Conference on Mathematical Modeling in Physical Sciences 2013 (IC-MSQUARE 2013), Prague - Czech Republic, 09/2013 (Virtual Presentation).

List of Figures

1.1	PGSE rectangle shaped profile, with $t_0 = 0$	12
1.2	PGSE trapezoidal shaped profile, with $t_0 = 0$	12
1.3	OGSE sine profile, each pulse contains 2 periods, with $t_0 = 0$	13
2.1	The function $c(t)$ for the rectangular PGSE profile, with $t_0 = 0$	30
2.2	The function $c(t)$ for the trapzoidal PGSE profile, with $t_0 = 0$	31
2.3	The function $c(t)$ for OGSE sine profile, each pulse contains 2 periods, with $t_0 = 0$	31
3.1	Verification for the residence time τ^{es} at two permeabilities (a) $\kappa = 1 \times 10^{-5}$ m/s, (b) $\kappa = 1 \times 10^{-4}$ m/s.	38
3.2	(a) Finite elements mesh of C ; (b) DMRI signals: $S_{PDE}(b)$, $S_{ODE}(b)$, $S_{NOEX}(b)$, $S_{FASTEX}(b)$; (c) Compartment magnetization in the extra-cellular compartment at $b = 2000$ s/mm ² : $\overline{M}_{PDE}^e(2000, t)$, $\overline{M}_{ODE}^e(2000, t)$; (d) Compartment magnetization in the sphere at $b = 2000$ s/mm ² : $\overline{M}_{PDE}^s(2000, t)$, $\overline{M}_{ODE}^s(2000, t)$. Cell radius $2.45\mu\text{m}$, $\kappa = 10^{-5}$ m/s. PGSE sequence with $\delta = \Delta = 40$ ms.	39
3.3	The domain is a periodic lattice of spheres, $R^s = 2.45\mu\text{m}$, $\kappa = 10^{-5}$ m/s. Top: the gradient profiles: (a) two pulses $\delta = \Delta = 40$ ms, $\tau = \delta/3$, (b) four pulses $\delta = \Delta = 20$ ms, $\tau = \delta/3$. Middle: the dMRI signal, $S_{PDE}(b)$, $S_{ODE}(b)$, as a function of b-value. Bottom: the sums of the compartment magnetizations $\overline{M}_{PDE}^e(2000, t) + \overline{M}_{PDE}^s(2000, t)$, $\overline{M}_{ODE}^e(2000, t) + \overline{M}_{ODE}^s(2000, t)$, as a function of time at $b = 2000$ s/mm ²	40
3.4	The domain is a periodic lattice of spheres, $R^s = 2.45\mu\text{m}$, $\kappa = 10^{-5}$ m/s. Top: the gradient profiles. Middle: the dMRI signal, $S_{PDE}(b)$, $S_{ODE}(b)$, $S_{KAR}(b)$, as a function of b-value. Bottom: the sums of the compartment magnetizations $\overline{M}_{PDE}^e(2000, t) + \overline{M}_{PDE}^s(2000, t)$, $\overline{M}_{ODE}^e(2000, t) + \overline{M}_{ODE}^s(2000, t)$ as a function of time at $b = 2000$ s/mm ²	41
3.5	The domain is a periodic lattice of spheres, $R^s = 2.45\mu\text{m}$, $\kappa = 10^{-5}$ m/s. $S_{ODE}(b)$ is closer to $S_{PDE}(b)$ for longer diffusion time.	42
3.6	The domain is a periodic lattice of spheres, $R^s = 2.45\mu\text{m}$. The gradient sequence is PGSE with $\delta = 10$ ms, $\Delta = 10$ ms and $\delta = 80$ ms, $\Delta = 80$ ms. The accuracy of the ODE model (as compared to the PDE model) improves as the diffusion time increases, if the permeability is low.	43

3.7	Two periodic lattices of spheres, with $R^s = 2.45\mu\text{m}$ and $R^s = 4.9\mu\text{m}$, $\kappa = 10^{-5}\text{m/s}$. $S_{PDE}(b)$ and $S_{ODE}(b)$ for the PGSE sequence with $\delta = \Delta = 40\text{ms}$ and $\delta = \Delta = 80\text{ms}$ are shown in (a) and (b). Setting $\kappa = 0\text{m/s}$, we also computed the ADC_0 corresponding to many PGSE sequences, with $\delta = 1\text{ms}$, and Δ varying from 10ms to 160ms , for the extra-cellular space Ω^e (c) and for the intra-cellular space Ω^s (d). One can see that while the extra-cellular space Ω^e can be considered a Gaussian diffusion compartment for both sphere sizes (look at the scale of the y-axis), the sphere compartment Ω^s cannot be considered a Gaussian diffusion compartment when $R = 4.9\mu\text{m}$ because the ADC_0 is changing a lot with diffusion time on $[0\text{ms}, 160\text{ms}]$	45
3.8	(a) The computational domain $C = [-5\mu\text{m}, 5\mu\text{m}]^3$ contains 76 spheres with radii $0.6 - 2.55\mu\text{m}$. The volume fractions of the spheres and of the extra-cellular space are $v^s = 0.65$ and $v^e = 0.35$, respectively. The membrane permeability is set to $\kappa = 10^{-5}\text{m/s}$. (b) The dMRI signals: $S_{PDE}(b)$, $S_{ODE}(b)$, $S_{KAR}(b)$, $S_{NOEX}(b)$, $S_{FASTEX}(b)$. The gradient sequence is PGSE with $\delta = \Delta = 25\text{ms}$	46
3.9	In (a), left: finite elements mesh of $C = [-2.89, 2.89] \times [-2.5, 2.5] \times [-5, 5]\mu\text{m}^3$, right: when periodically extended, the cylinders are infinitely long. In (b): $S_{PDE}(b)$ and $S_{ODE}(b)$ when $\kappa = 10^{-5}\text{m/s}$. The gradient directions are $\mathbf{g}_1 = (0.5, 0, 0.87)$ and $\mathbf{g}_2 = (0.87, 0, -0.5)$, correspondingly parallel and perpendicular to the axis of cylinders, and $\mathbf{g}_3 = (0.97, 0, 0.26)$, lying in the middle of \mathbf{g}_1 and \mathbf{g}_2 . The sequence is PGSE, with $\delta = \Delta = 80\text{ms}$	47
3.10	$C = [-2.75, 2.75]^2 \times [-0.5, 0.5]\mu\text{m}^3$, cylinder radius $R^c = 2.0\mu\text{m}$, membrane thickness $h = 0.45\mu\text{m}$. In (a), finite elements meshes, left: two-compartment domain (Ω^e and Ω^{e+m}), right: three-compartment domain (Ω^e and Ω^c and Ω^m). In (b). $S_{PDE}(b)$ and $S_{ODE}(b)$ of the three-compartment domain and the two-compartment domain, with $\kappa = 10^{-5}\text{m/s}$, subject to PGSE $\delta = \Delta = 80\text{ms}$, in the gradient direction $g = (1, 0, 0)$, perpendicular with the axis of cylinder.	48
3.11	(a) Finite elements mesh of C containing 5 layers of cylinders and 4 layers of spheres. In each layer, the cylinders have the same orientation. (b) $S_{PDE}(b)$ and $S_{ODE}(b)$. The cell membrane permeability is $\kappa = 10^{-5}\text{m/s}$. The gradient directions are $\mathbf{g}_1 = (1, 0, 0)$, $\mathbf{g}_2 = (1, 0, 1)$, and $\mathbf{g}_3 = (1, 1, 1)$. The pulse sequence is PGSE, with $\delta = \Delta = 40\text{ms}$	50
4.1	Contour plots of the residuals $R_{ODE}(\mathcal{U})$ and $R_{KAR}(\mathcal{U})$. First τ^{es} is fixed at the true value, while $\{v^s, D_{\mathbf{g}}^e\}$ are estimated (a,b). Then $D_{\mathbf{g}}^e$ is fixed at the true value, while $\{v^s, \tau^{es}\}$ are estimated (c,d). PGSE with $\delta = \Delta = 40\text{ms}$, $n_b = 20$. R^{mod} : (a,c) 2.6%, (b,d) 14%; $R_{ODE}(\mathcal{U}_{ODE}^{min})$: (a,b) 0.5%, (c,d) 0.2%; $R_{KAR}(\mathcal{U}_{KAR}^{min})$: (a,b) 1.6%, (c,d) 0.6%.	60

List of Figures

- 4.2 Contour plot of ODE model. Periodic lattice of spheres, cell radius $R^s = 2.45\mu\text{m}$, inter-cell distance $L = 5\mu\text{m}$. PGSE sequence: $\delta = 40\text{ms}$, $\Delta = 40\text{ms}$, $n_b = 20$. R^{mod} : (a,c) 2.6%, (b,d) 11.7%; $R_{ODE}(\mathcal{U}_{ODE}^{min})$: (a) 0.5%, (b) 0.4%, (c) 0.2% (d) 1.1%; $R_{KAR}(\mathcal{U}_{KAR}^{min})$: (a) 1.6%, (b) 6.1%, (c) 0.6% (d) 1.9%. 61
- 4.3 Contour plot of ODE model and Kärger model. Periodic lattice of spheres, cell radius $R^s = 2.45\mu\text{m}$, inter-cell distance $L = 5\mu\text{m}$. PGSE sequence, $n_b = 20$. R^{mod} : (a) 8.4%, (b) 11.6%, (c) 2.4%, (d) 2.8% , (e) 2.6%, (f) 14%; $R_{ODE}(\mathcal{U}_{ODE}^{min})$: (a,b) 2.3%, (c,d) 0.3%, (e,f) 0.5%; $R_{KAR}(\mathcal{U}_{KAR}^{min})$: (a,b) 2.5%, (c,d) 0.3%, (e,f) 1.6%. 63
- 4.4 Contour plot of ODE model and Kärger model. Periodic lattice of spheres, cell radius $R^s = 2.45\mu\text{m}$, inter-cell distance $L = 5\mu\text{m}$. PGSE sequence, $n_b = 20$. R^{mod} : (a) 8.4%, (b) 11.6%, (c) 2.4%, (d) 2.8% , (e) 2.6%, (f) 14%; $R_{ODE}(\mathcal{U}_{ODE}^{min})$: (a,b) 1.2%, (c,d) 0.2%, (e,f) 0.2%; $R_{KAR}(\mathcal{U}_{KAR}^{min})$: (a,b) 1.5%, (c,d) 0.2%, (e,f) 0.6%. 64
- 4.5 Domain containing periodic lattice of spheres shown in Fig. 3.2(a), cell radius $2.45\mu\text{m}$, cell distance $5\mu\text{m}$, contour plot of ODE model with PGSE profile $\delta = 40\text{ms}$, $\Delta = 40\text{ms}$, $n_b = 20$ b -values in range (a) $[0, 1000\text{s}/\text{mm}^2]$, (b) $[0, 2000\text{s}/\text{mm}^2]$, (c) $[0, 1000\text{s}/\text{mm}^2]$. R^{mod} : (a,b) 0.8%, (c,d) 1.5%, (e,f) 2.6%; $R_{ODE}(\mathcal{U}_{ODE}^{min})$: (a) 0.1%, (b) 0.1%, (c) 0.1%, (d) 0.2% , (e) 0.5%, (f) 0.2%; $R_{KAR}(\mathcal{U}_{KAR}^{min})$: (a) 0.1%, (b) 0.1%, (c) 0.4%, (d) 0.3% , (e) 1.6%, (f) 0.6%. 66
- 4.6 Domain containing periodic lattice of spheres in shown Fig. 3.2(a), cell radius $2.45\mu\text{m}$, cell distance $5\mu\text{m}$, contour plot of ODE model with PGSE profile $\delta = 40\text{ms}$, $\Delta = 40\text{ms}$, fixed range b -value in $[0, 4000\text{s}/\text{mm}^2]$ with different numbers (a) $n_b = 10$ (b) $n_b = 20$ (c) $n_b = 40$. R^{mod} : (a,b) 2.2%, (c,d) 2.6%, (e,f) 2.4%; $R_{ODE}(\mathcal{U}_{ODE}^{min})$: (a) 0.4%, (b) 0.2%, (c) 0.5%, (d) 0.2% , (e) 0.4%, (f) 0.2%; $R_{KAR}(\mathcal{U}_{KAR}^{min})$: (a) 1.4%, (b) 0.6%, (c) 1.6%, (d) 0.6% , (e) 1.5%, (f) 0.6%. 68
- 4.7 Domain containing periodic lattice of spheres shown in Fig. 3.2(a). Contour plot of ODE model with respect to v^s and $D_{\mathbf{g}}^e$, $n_b = 20$. R^{mod} : (a) 8.4%, (b) 59.7%, (c) 2.6%, (d) 10.1% , (e) 2.2%, (f) 5.7%; $R_{ODE}(\mathcal{U}_{ODE}^{min})$: (a) 2.3%, (b) 15.6%, (c) 0.5%, (d) 2.2% , (e) 0.4%, (f) 1.0%; $R_{KAR}(\mathcal{U}_{KAR}^{min})$: (a) 2.5%, (b) 16.7%, (c) 1.6%, (d) 2.7% , (e) 2.0%, (f) 2.0%. 71
- 4.8 Domain containing periodic lattice of spheres shown in Fig. 3.2(a). Contour plot of ODE model with respect to v^s and τ^{es} , $n_b = 20$. R^{mod} : (a) 8.4%, (b) 59.7%, (c) 2.6%, (d) 10.1% , (e) 2.2%, (f) 5.7%; $R_{ODE}(\mathcal{U}_{ODE}^{min})$: (a) 1.2%, (b) 5.5%, (c) 0.2%, (d) 1.2% , (e) 0.2%, (f) 0.5%; $R_{KAR}(\mathcal{U}_{KAR}^{min})$: (a) 1.5%, (b) 6.8%, (c) 0.6%, (d) 1.6% , (e) 0.7%, (f) 1.0%. 72

4.9	Domain containing spherical cells of different sizes, $\kappa = 10^{-5}$ m/s, PGSE profile $\delta = \Delta = 30$ ms, contour plots of ODE model and Kärger model. R^{mod} : (a,c) 0.9%, (b,d) 9.5%; $R_{ODE}(\mathcal{U}_{ODE}^{min})$: (a,b) 0.2%, (c,d) 0.2%; $R_{KAR}(\mathcal{U}_{KAR}^{min})$: (a,b) 0.9%, (c,d) 0.4%.	75
4.10	Domain containing spherical cells of different sizes: $\kappa = 10^{-5}$ m/s, PGSE with $\delta = \Delta = 30$ ms, convex hulls of 1000 samples of noisy signal with two noise levels: $\sigma_1 = 0.01$ and $\sigma_2 = 0.03$, contour plot of ODE model with respect to v^s and D_g^e (a,c,e) and v^s and τ^{es} (b,d,f). R^{mod} : (a,b,c,d,e,f) 0.9%.	78
4.11	Domain containing parallel cylinders with thick membrane, $\kappa = 10^{-5}$ m/s, PGSE profile with $\delta = \Delta = 80$ ms (a,b) v^s and D_g^e , (c,d) τ^{em} and τ^{cm} . R^{mod} : (a,c) 1.8%, (b,d) 6.7%; $R_{ODE}(\mathcal{U}_{ODE}^{min})$: (a,b) 1.3%, (c,d) 0.1%; $R_{KAR}(\mathcal{U}_{KAR}^{min})$: (a,b) 3.9%, (c,d) 2.3%.	81
4.12	Domain containing slanted parallel cylinders, $\kappa = 10^{-5}$ m/s, PGSE with $\delta = \Delta = 80$ ms, contour plots for the ODE model. R^{mod} : (a,b) 0.8%, (c,d) 3.8% , (e,f) 0.2%; $R_{ODE}(\mathcal{U}_{ODE}^{min})$: (a) 0.01%, (b) 0.57%, (c) 0.16%, (d) 0.17% , (e) 0.05%, (f) 0.05%; $R_{KAR}(\mathcal{U}_{KAR}^{min})$: (a) 0.01%, (b) 0.57%, (c) 0.14%, (d) 0.35% , (e) 0.05%, (f) 0.05%.	85
4.13	Spherical and cylindrical cells, $\kappa = 10^{-5}$ m/s, PGSE with $\delta = \Delta = 40$ ms: (a,d,g) v^e and D_g^e , (b,e,h) v^s and τ^{sc} , (c,f,i) τ^{ec} and τ^{es} . R^{mod} : (a,b,c) 0.4%, (d,e,f) 1.5%, (g,h,i) 1.8% $R_{ODE}(\mathcal{U}_{ODE}^{min})$: (a) 0.1%, (b) 0.06%, (c) 0.09%, (d) 0.2% , (e) 0.2%, (f) 0.2%, (g) 0.3%, (h) 0.2%, (i) 0.2%; $R_{KAR}(\mathcal{U}_{KAR}^{min})$: (a) 0.5%, (b) 0.4%, (c) 1.1%, (d) 10.9% , (e) 6.7%, (f) 6.0%, (g) 12.9%, (h) 0.8%, (i) 7.5%.	88
4.14	Circular (a) and square (b) shapes of two-dimensional cells which are formed into periodic lattices.	90
4.15	Relationship between v^c and D_g^e obtained by numerical solution of the steady-state Laplace equations for circular and square shapes. . .	91
4.16	Contour plot of the ODE model for circular shapes with respect to v^c and D_g^e (a), and v^c and τ^{es} (b).	91

List of Tables

3.1	Memory usage and average computational time per b-value to solve the Bloch-Torrey PDE.	36
4.1	Results of parameter estimations for the domain containing periodic lattice of spherical cells (Fig. 3.2(a)), $R^s = 2.45\mu\text{m}$, $L = 5\mu\text{m}$. PGSE sequence with $\delta = \Delta = 40\text{ms}$ in gradient direction $\mathbf{g} = [1, 0, 0]$ with $D^0 = 3 \times 10^{-3}\text{mm}^2/\text{s}$	58
4.2	Parameters estimation results for the domain containing periodic lattice of spherical cells of different sizes shown in Fig. 3.8(a), with different permeabilites.	74
4.3	Relative errors of \mathcal{U} for the domain shown in Fig. 3.8(a) from $N = 100$ samples of Gaussian noises $\mathcal{N}(0, 0.01)$ and $\mathcal{N}(0, 0.03)$, $\kappa = 10^{-5}\text{m/s}$, PGSE sequence with $\delta = \Delta = 30\text{ms}$. R^{mod} : (a,b,c,d,e,f) 0.9%.	77
4.4	Estimated macroscopic model parameters for the domain containing parallel cylinders with thick membrane, $\kappa = 1 \times 10^{-5}\text{m/s}$, PGSE profile with $\delta = \Delta = 80\text{ms}$	80

Bibliography

1. P. T. Callaghan, *Principles of nuclear magnetic resonance microscopy*. Oxford University Press, 1993. (Cited on pages 9, 11 and 16.)
2. W. S. Price, *NMR studies of translational motion: principles and applications*. Cambridge University Press, 2009. (Cited on pages 11 and 16.)
3. D. Grebenkov, “Nmr survey of reflected brownian motion,” *Reviews of Modern Physics*, vol. 79, no. 3, pp. 1077–1137, 2007. (Cited on pages 9, 15, 16, 17 and 53.)
4. D. Le Bihan, J.-F. Mangin, C. Poupon, C. A. Clark, S. Pappata, N. Molko, and H. Chabriat, “Diffusion tensor imaging: concepts and applications,” *Journal of magnetic resonance imaging*, vol. 13, no. 4, pp. 534–546, 2001. (Cited on page 9.)
5. D. G. Norris, “The effects of microscopic tissue parameters on the diffusion weighted magnetic resonance imaging experiment,” *NMR in Biomedicine*, vol. 14, no. 2, pp. 77–93, 2001.
6. D. Le Bihan and H. Johansen-Berg, “Diffusion mri at 25: Exploring brain tissue structure and function,” *NeuroImage*, vol. 61, pp. 324–341, June 2012. (Cited on page 10.)
7. D. S. Tuch, T. G. Reese, M. R. Wiegell, and V. J. Wedeen, “Diffusion mri of complex neural architecture,” *Neuron*, vol. 40, no. 5, pp. 885–895, 2003.
8. Y. Cohen and Y. Assaf, “High b-value q-space analyzed diffusion-weighted mrs and mri in neuronal tissues—a technical review,” *NMR in Biomedicine*, vol. 15, no. 7-8, pp. 516–542, 2002.
9. C. Beaulieu, “The basis of anisotropic water diffusion in the nervous system - a technical review,” *NMR in Biomedicine*, vol. 15, no. 7-8, pp. 435–455, 2002.
10. D. Le Bihan, “Looking into the functional architecture of the brain with diffusion mri,” *Nature Reviews Neuroscience*, vol. 4, no. 6, pp. 469–480, 2003.
11. J. Frahm, P. Dechent, J. Baudewig, and K. Merboldt, “Advances in functional mri of the human brain,” *Progress in Nuclear Magnetic Resonance Spectroscopy*, vol. 44, no. 1, pp. 1–32, 2004.
12. D. LeBihan, “The ‘wet mind’: water and functional neuroimaging.,” *Physics in medicine and biology*, vol. 52, pp. –, Apr. 2007. (Cited on pages 9 and 10.)
13. M. Moseley, J. Kucharczyk, J. Mintorovitch, Y. Cohen, J. Kurhanewicz, N. Derugin, H. Asgari, and D. Norman, “Diffusion-weighted mr imaging

- of acute stroke: correlation with t2- weighted and magnetic susceptibility-enhanced mr imaging in cats,” *AJNR Am J Neuroradiol*, vol. 11, no. 3, pp. 423–429, 1990. (Cited on page 9.)
14. S. Warach, D. Chien, W. Li, M. Ronthal, and R. R. Edelman, “Fast magnetic resonance diffusion-weighted imaging of acute human stroke,” *Neurology*, vol. 42, no. 9, pp. 1717–, 1992. (Cited on page 9.)
 15. D. Schnapauff, M. Zeile, M. B. Niederhagen, B. Fleige, P.-U. Tunn, B. Hamm, and O. Dudeck, “Diffusion-weighted echo-planar magnetic resonance imaging for the assessment of tumor cellularity in patients with soft-tissue sarcomas,” *J. Magn. Reson. Imaging*, vol. 29, no. 6, pp. 1355–1359, 2009. (Cited on page 9.)
 16. T. Sugahara, Y. Korogi, M. Kochi, I. Ikushima, Y. Shigematu, T. Hirai, T. Okuda, L. Liang, Y. Ge, Y. Komohara, Y. Ushio, and M. Takahashi, “Usefulness of diffusion-weighted mri with echo-planar technique in the evaluation of cellularity in gliomas,” *J. Magn. Reson. Imaging*, vol. 9, no. 1, pp. 53–60, 1999.
 17. S. E. Maier, Y. Sun, and R. V. Mulkern, “Diffusion imaging of brain tumors,” *NMR Biomed.*, vol. 23, no. 7, pp. 849–864, 2010.
 18. Y. Tsushima, A. Takahashi-Taketomi, and K. Endo, “Magnetic resonance (mr) differential diagnosis of breast tumors using apparent diffusion coefficient (adc) on 1.5-t,” *J. Magn. Reson. Imaging*, vol. 30, no. 2, pp. 249–255, 2009. (Cited on page 9.)
 19. M. A. Horsfield and D. K. Jones, “Applications of diffusion-weighted and diffusion tensor mri to white matter diseases, a review,” *NMR Biomed.*, vol. 15, no. 7-8, pp. 570–577, 2002. (Cited on page 9.)
 20. M. Lazar, “Mapping brain anatomical connectivity using white matter tractography,” *NMR Biomed.*, vol. 23, no. 7, pp. 821–835, 2010. (Cited on page 9.)
 21. D. LeBihan, C. Poupon, A. Amadon, and F. Lethimonnier, “Artifacts and pitfalls in diffusion mri,” *Journal of Magnetic Resonance Imaging*, vol. 24, no. 3, pp. 478–488, 2006. (Cited on page 9.)
 22. D. L. Buckley, J. D. Bui, M. I. Phillips, and S. J. Blackband, “Mri measurement of cell volume fraction in the perfused rat hippocampal slice,” *Magn. Reson. Med.*, vol. 42, no. 3, pp. 603–607, 1999. (Cited on page 9.)
 23. J. Flint, B. Hansen, P. Vestergaard-Poulsen, and S. J. Blackband, “Diffusion weighted magnetic resonance imaging of neuronal activity in the hippocampal slice model,” *NeuroImage*, vol. 46, pp. 411–418, June 2009. (Cited on page 9.)
 24. R. Andrew and B. Macvicar, “Imaging cell volume changes and neuronal excitation in the hippocampal slice,” *Neuroscience*, vol. 62, pp. 371–383, Sept. 1994. (Cited on page 10.)

Bibliography

25. F. Bloch, "Nuclear induction," *Phys. Rev.*, vol. 70, pp. 460–474, Oct. 1946. (Cited on page 10.)
26. H. Torrey, "Bloch equations with diffusion terms," *Physical Review Online Archive (Prola)*, vol. 104, no. 3, pp. 563–565, 1956. (Cited on pages 11, 14 and 25.)
27. E. O. Stejskal and J. E. Tanner, "Spin diffusion measurements: Spin echoes in the presence of a time-dependent field gradient," *The Journal of Chemical Physics*, vol. 42, no. 1, pp. 288–292, 1965. (Cited on page 11.)
28. M. D. Does, E. C. Parsons, and J. C. Gore, "Oscillating gradient measurements of water diffusion in normal and globally ischemic rat brain," *Magn. Reson. Med.*, vol. 49, no. 2, pp. 206–215, 2003. (Cited on page 12.)
29. D. Le Bihan, E. Breton, D. Lallemand, P. Grenier, E. Cabanis, and M. Laval-Jeantet, "MR imaging of intravoxel incoherent motions: application to diffusion and perfusion in neurologic disorders.," *Radiology*, vol. 161, no. 2, pp. 401–407, 1986. (Cited on page 14.)
30. V. Kenkre, E. Fukushima, and D. Sheltraw, "Simple solutions of the torrey–bloch equations in the nmr study of molecular diffusion," *Journal of Magnetic Resonance*, vol. 128, no. 1, pp. 62–69, 1997. (Cited on pages 14 and 29.)
31. D. Rohmer and G. T. Gullberg, *A Bloch-Torrey Equation for Diffusion in a Deforming Media*. Ernest Orlando Lawrence Berkeley National Laboratory, Berkeley, CA (US), Dec 2006. (Cited on page 15.)
32. T. Niendorf, R. M. Dijkhuizen, D. G. Norris, M. van Lookeren Campagne, and K. Nicolay, "Biexponential diffusion attenuation in various states of brain tissue: Implications for diffusion-weighted imaging," *Magn. Reson. Med.*, vol. 36, no. 6, pp. 847–857, 1996. (Cited on page 16.)
33. R. V. Mulkern, H. Gudbjartsson, C.-F. Westin, H. P. Zengingonul, W. Gartner, C. R. Guttmann, R. L. Robertson, W. Kyriakos, R. Schwartz, D. Holtzman, *et al.*, "Multi-component apparent diffusion coefficients in human brain²," *NMR Biomed*, vol. 12, pp. 51–62, 1999.
34. C. A. Clark and D. Le Bihan, "Water diffusion compartmentation and anisotropy at high b values in the human brain," *Magn. Reson. Med.*, vol. 44, no. 6, pp. 852–859, 2000.
35. S. E. Maier, P. Bogner, G. Bajzik, H. Mamata, Y. Mamata, I. Repa, F. A. Jolesz, and R. V. Mulkern, "Normal brain and brain tumor: Multicomponent apparent diffusion coefficient line scan imaging¹," *Radiology*, vol. 219, no. 3, pp. 842–849, 2001. (Cited on page 16.)
36. S. Chabert, N. Molko, Y. Cointepas, P. Le Roux, and D. Le Bihan, "Diffusion tensor imaging of the human optic nerve using a non-CPMG fast spin echo sequence," *J. Magn. Reson. Imaging*, vol. 22, no. 2, pp. 307–310, 2005. (Cited on pages 16 and 19.)

37. J. H. Jensen, J. A. Helpert, A. Ramani, H. Lu, and K. Kaczynski, "Diffusional kurtosis imaging: The quantification of non-Gaussian water diffusion by means of magnetic resonance imaging," *Magnetic Resonance in Medicine*, vol. 53, no. 6, pp. 1432–1440, 2005. (Cited on pages 16, 17 and 19.)
38. R. L. Magin, O. Abdullah, D. Baleanu, and X. J. Zhou, "Anomalous diffusion expressed through fractional order differential operators in the bloch-torrey equation," *Journal of Magnetic Resonance*, vol. 190, no. 2, pp. 255 – 270, 2008. (Cited on page 16.)
39. B. Robertson, "Spin-echo decay of spins diffusing in a bounded region," *Physical Review*, vol. 151, no. 1, p. 273, 1966. (Cited on page 16.)
40. C. Neuman, "Spin echo of spins diffusing in a bounded medium," *The Journal of Chemical Physics*, vol. 60, p. 4508, 1974. (Cited on page 16.)
41. J. Tanner and E. O. Stejskal, "Restricted self-diffusion of protons in colloidal systems by the pulsed-gradient, spin-echo method," *The Journal of Chemical Physics*, vol. 49, p. 1768, 1968. (Cited on page 16.)
42. B. Balinov, B. Jonsson, P. Linse, and O. Soderman, "The nmr self-diffusion method applied to restricted diffusion. simulation of echo attenuation from molecules in spheres and between planes," *Journal of Magnetic Resonance, Series A*, vol. 104, no. 1, pp. 17–25, 1993. (Cited on pages 16 and 18.)
43. M. H. Blees, "The effect of finite duration of gradient pulses on the pulsed-field-gradient nmr method for studying restricted diffusion," *Journal of Magnetic Resonance, Series A*, vol. 109, no. 2, pp. 203–209, 1994. (Cited on page 18.)
44. A. Coy and P. T. Callaghan, "Pulsed gradient spin echo nuclear magnetic resonance for molecules diffusing between partially reflecting rectangular barriers," *The Journal of chemical physics*, vol. 101, p. 4599, 1994. (Cited on page 18.)
45. P. Linse and O. Soderman, "The validity of the short-gradient-pulse approximation in nmr studies of restricted diffusion. simulations of molecules diffusing between planes, in cylinders and spheres," *Journal of Magnetic Resonance, Series A*, vol. 116, no. 1, pp. 77–86, 1995. (Cited on pages 16 and 18.)
46. J. Kärger, "Nmr self-diffusion studies in heterogeneous systems," *Advances in Colloid and Interface Science*, vol. 23, pp. 129–148, 1985. (Cited on page 16.)
47. J. Kärger, H. Pfeifer, and W. Heinik, "Principles and application of self-diffusion measurements by nuclear magnetic resonance," *Advances in magnetic resonance*, vol. 12, pp. 1–89, 1988. (Cited on pages 16, 23 and 27.)
48. P. P. Mitra, P. N. Sen, L. M. Schwartz, and P. Le Doussal, "Diffusion propagator as a probe of the structure of porous media," *Physical review letters*, vol. 68, no. 24, pp. 3555–3558, 1992. (Cited on page 17.)

Bibliography

49. P. P. Mitra and P. N. Sen, "Effects of microgeometry and surface relaxation on nmr pulsed-field-gradient experiments: Simple pore geometries," *Physical Review B*, vol. 45, no. 1, p. 143, 1992.
50. L. L. Latour, P. P. Mitra, R. L. Kleinberg, and C. H. Sotak, "Time-dependent diffusion coefficient of fluids in porous media as a probe of surface-to-volume ratio," *Journal of Magnetic Resonance, Series A*, vol. 101, no. 3, pp. 342–346, 1993.
51. M. Hurlimann, K. G. Helmer, L. Latour, and C. H. Sotak, "Restricted diffusion in sedimentary rocks. determination of surface-area-to-volume ratio and surface relaxivity," *Journal of Magnetic Resonance, Series A*, vol. 111, no. 2, pp. 169–178, 1994. (Cited on page 17.)
52. L. L. Latour, K. Svoboda, P. P. Mitra, and C. H. Sotak, "Time-dependent diffusion of water in a biological model system.," *Proceedings of the National Academy of Sciences*, vol. 91, no. 4, pp. 1229–1233, 1994. (Cited on pages 17 and 22.)
53. L. Latour, R. L. Kleinberg, P. P. Mitra, and C. H. Sotak, "Pore-size distributions and tortuosity in heterogeneous porous media," *Journal of Magnetic Resonance, Series A*, vol. 112, no. 1, pp. 83–91, 1995. (Cited on page 17.)
54. P. T. Callaghan, A. Coy, D. Macgowan, K. J. Packer, and F. O. Zelaya, "Diffraction-like effects in NMR diffusion studies of fluids in porous solids," *Nature*, vol. 351, pp. 467–469, 1991. (Cited on page 17.)
55. S. D. Stoller, W. Happer, and F. J. Dyson, "Transverse spin relaxation in inhomogeneous magnetic fields," *Phys. Rev. A*, vol. 44, pp. 7459–7477, Dec. 1991. (Cited on page 17.)
56. T. M. de Swiet and P. N. Sen, "Decay of nuclear magnetization by bounded diffusion in a constant field gradient," *The Journal of chemical physics*, vol. 100, p. 5597, 1994. (Cited on page 17.)
57. S. Axelrod and P. N. Sen, "Nuclear magnetic resonance spin echoes for restricted diffusion in an inhomogeneous field: Methods and asymptotic regimes," *The Journal of Chemical Physics*, vol. 114, p. 6878, 2001. (Cited on page 17.)
58. M. Hurlimann, K. Helmer, T. Deswiet, and P. Sen, "Spin echoes in a constant gradient and in the presence of simple restriction," *Journal of Magnetic Resonance, Series A*, vol. 113, no. 2, pp. 260–264, 1995. (Cited on page 17.)
59. A. Barzykin, K. Hayamizu, W. Price, and M. Tachiyu, "Pulsed-field-gradient nmr of diffusive transport through a spherical interface into an external medium containing a relaxation agent," *Journal of Magnetic Resonance, Series A*, vol. 114, no. 1, pp. 39–46, 1995. (Cited on page 17.)

60. W. S. Price, A. V. Barzykin, K. Hayamizu, and M. Tachiya, "A model for diffusive transport through a spherical interface probed by pulsed-field gradient NMR," *Biophysical Journal*, vol. 74, pp. 2259–2271, May 1998. (Cited on pages 17, 22 and 25.)
61. A. Caprihan, "A multiple-narrow-pulse approximation for restricted diffusion in a time-varying field gradient," *Journal of Magnetic Resonance, Series A*, vol. 118, pp. 94–102, Jan. 1996. (Cited on page 17.)
62. P. Callaghan, "A simple matrix formalism for spin echo analysis of restricted diffusion under generalized gradient waveforms," *Journal of Magnetic Resonance*, vol. 129, pp. 74–84, Nov. 1997.
63. A. V. Barzykin, "Exact solution of the torrey-bloch equation for a spin echo in restricted geometries," *Physical Review B*, vol. 58, no. 21, p. 14171, 1998.
64. A. V. Barzykin, "Theory of spin echo in restricted geometries under a step-wise gradient pulse sequence," *Journal of Magnetic Resonance*, vol. 139, no. 2, pp. 342–353, 1999.
65. D. Grebenkov, "Laplacian eigenfunctions in nmr. i. a numerical tool," *Concepts in Magnetic Resonance Part A*, vol. 32A, no. 4, pp. 277–301, 2008. (Cited on page 17.)
66. D. S. Grebenkov, "Laplacian eigenfunctions in nmr. ii. theoretical advances," *Concepts Magn. Reson.*, vol. 34A, no. 5, pp. 264–296, 2009. (Cited on page 17.)
67. D. S. Grebenkov, "Pulsed-gradient spin-echo monitoring of restricted diffusion in multilayered structures," *Journal of Magnetic Resonance*, vol. 205, pp. 181–195, Aug. 2010. (Cited on pages 17, 22 and 26.)
68. A. F. Frøhlich, L. Østergaard, and V. G. Kiselev, "Effect of impermeable boundaries on diffusion-attenuated mr signal," *Journal of Magnetic Resonance*, vol. 179, no. 2, pp. 223–233, 2006. (Cited on page 17.)
69. V. G. Kiselev, V., "The cumulant expansion: an overarching mathematical framework for understanding diffusion nmr," *Diffusion MRI: Theory, Methods, and Applications: Theory, Methods, and Applications*, p. 152, 2010. (Cited on page 17.)
70. D. S. Novikov and V. G. Kiselev, "Effective medium theory of a diffusion-weighted signal," *NMR in Biomedicine*, vol. 23, no. 7, pp. 682–697, 2010. (Cited on pages 17 and 51.)
71. D. S. Novikov, E. Fieremans, J. H. Jensen, and J. A. Helpert, "Random walks with barriers," *Nat Phys*, vol. 7, pp. 508–514, June 2011. (Cited on pages 17 and 22.)

Bibliography

72. J. Powles, M. Mallett, G. Rickayzen, and W. Evans, “Exact analytic solutions for diffusion impeded by an infinite array of partially permeable barriers,” *Proceedings of the Royal Society of London. Series A: Mathematical and Physical Sciences*, vol. 436, no. 1897, pp. 391–403, 1992. (Cited on page 17.)
73. C. Meier, W. Dreher, and D. Leibfritz, “Diffusion in compartmental systems. i. a comparison of an analytical model with simulations,” *Magnetic Resonance in Medicine*, vol. 50, no. 3, pp. 500–509, 2003. (Cited on pages 18 and 23.)
74. D. Grebenkov, G. Guillot, and B. Sapoval, “Restricted diffusion in a model acinar labyrinth by nmr: theoretical and numerical results,” *Journal of Magnetic Resonance*, vol. 184, no. 1, pp. 143–156, 2007.
75. M. D. Budde and J. A. Frank, “Neurite beading is sufficient to decrease the apparent diffusion coefficient after ischemic stroke,” *Proceedings of the National Academy of Sciences*, vol. 107, no. 32, pp. 14472–14477, 2010. (Cited on page 22.)
76. E. Fieremans, D. S. Novikov, J. H. Jensen, and J. A. Helpert, “Monte carlo study of a two-compartment exchange model of diffusion,” *NMR in Biomedicine*, vol. 23, no. 7, pp. 711–724, 2010. (Cited on pages 23, 24, 27 and 33.)
77. D. Grebenkov, “A fast random walk algorithm for computing the pulsed-gradient spin-echo signal in multiscale porous media,” *Journal of Magnetic Resonance*, vol. 208, no. 2, pp. 243 – 255, 2011.
78. D. S. Grebenkov, H. T. Nguyen, and J.-R. Li, “A fast random walk algorithm for computing diffusion-weighted nmr signals in multi-scale porous media: a feasibility study for a menger sponge,” *Microporous and Mesoporous Materials*, vol. 178, pp. 56–59, 2013.
79. C.-H. Yeh, B. Schmitt, D. Le Bihan, J.-R. Li-Schlittgen, C.-P. Lin, and C. Poupon, “Diffusion microscopist simulator: A general monte carlo simulation system for diffusion magnetic resonance imaging,” *PloS one*, vol. 8, no. 10, p. e76626, 2013. (Cited on page 18.)
80. J. C. Ford and D. B. Hackney, “Numerical model for calculation of apparent diffusion coefficients (adc) in permeable cylinders—comparison with measured adc in spinal cord white matter,” *Magnetic resonance in medicine*, vol. 37, no. 3, pp. 387–394, 1997. (Cited on pages 18 and 21.)
81. C.-L. Chin, F. W. Wehrli, S. N. Hwang, M. Takahashi, and D. B. Hackney, “Biexponential diffusion attenuation in the rat spinal cord: computer simulations based on anatomic images of axonal architecture,” *Magnetic resonance in medicine*, vol. 47, no. 3, pp. 455–460, 2002.
82. S. N. Hwang, C.-L. Chin, F. W. Wehrli, and D. B. Hackney, “An image-based finite difference model for simulating restricted diffusion,” *Magnetic Resonance in Medicine*, vol. 50, no. 2, pp. 373–382, 2003. (Cited on page 21.)

-
83. J. Xu, M. Does, and J. Gore, "Numerical study of water diffusion in biological tissues using an improved finite difference method.," *Physics in medicine and biology*, vol. 52, Apr. 2007. (Cited on page 26.)
84. D. V. Nguyen, D. Grebenkov, and J.-R. Li, "An efficient finite-elements code to simulate diffusion mri signals in complex tissue geometries." Submitted. See <http://www.cmap.polytechnique.fr/~jingrebecali/preprints.html>, 2013. (Cited on pages 18 and 35.)
85. B. Hellwig, "A quantitative analysis of the local connectivity between pyramidal neurons in layers 2/3 of the rat visual cortex," *Biological Cybernetics*, vol. 82, no. 2, pp. 111–121, 2000. (Cited on page 19.)
86. A. Szafer, J. Zhong, and J. C. Gore, "Theoretical model for water diffusion in tissues," *Magn. Reson. Med.*, vol. 33, no. 5, pp. 697–712, 1995. (Cited on page 21.)
87. S. Grant, D. Buckley, S. Gibbs, A. Webb, and S. Blackband, "Mr microscopy of multicomponent diffusion in single neurons," *Magn. Reson. Med.*, vol. 46, pp. 1107–1112, Dec. 2001. (Cited on page 21.)
88. C. A. Clark, M. Hedehus, and M. E. Moseley, "Diffusion time dependence of the apparent diffusion tensor in healthy human brain and white matter disease," *Magnetic resonance in medicine*, vol. 45, no. 6, pp. 1126–1129, 2001. (Cited on page 21.)
89. Y. Assaf, R. Z. Freidlin, G. K. Rohde, and P. J. Basser, "New modeling and experimental framework to characterize hindered and restricted water diffusion in brain white matter," *Magnetic Resonance in Medicine*, vol. 52, no. 5, pp. 965–978, 2004. (Cited on page 21.)
90. D. C. Alexander, "A general framework for experiment design in diffusion mri and its application in measuring direct tissue-microstructure features," *Magnetic Resonance in Medicine*, vol. 60, no. 2, pp. 439–448, 2008. (Cited on page 21.)
91. J. Xu, M. D. Does, and J. C. Gore, "Quantitative characterization of tissue microstructure with temporal diffusion spectroscopy," *Journal of Magnetic Resonance*, vol. 200, pp. 189–197, Oct. 2009. (Cited on page 21.)
92. C. D. Kroenke, J. J. Ackerman, and D. A. Yablonskiy, "On the nature of the naa diffusion attenuated mr signal in the central nervous system," *Magnetic resonance in medicine*, vol. 52, no. 5, pp. 1052–1059, 2004. (Cited on page 21.)
93. P. N. Sen and P. J. Basser, "A model for diffusion in white matter in the brain," *Biophys J*, vol. 89, pp. 2927–2938, Nov. 2005. (Cited on pages 21, 23 and 24.)
94. D. A. Yablonskiy, A. L. Sukstanskii, J. C. Leawoods, D. S. Gierada, G. L. Bretthorst, S. S. Lefrak, J. D. Cooper, and M. S. Conradi, "Quantitative in

Bibliography

- vivo assessment of lung microstructure at the alveolar level with hyperpolarized ^3He diffusion mri,” *Proceedings of the National Academy of Sciences*, vol. 99, no. 5, pp. 3111–3116, 2002. (Cited on page 22.)
95. S. N. Jespersen, C. D. Kroenke, L. Åstergaard, J. J. Ackerman, and D. A. Yablonskiy, “Modeling dendrite density from magnetic resonance diffusion measurements,” *NeuroImage*, vol. 34, pp. 1473–1486, Feb. 2007. (Cited on pages 22 and 23.)
96. N. Buhl and S. Jespersen, “A simulation framework for diffusion weighted mri in digitalized neurons: Extracting cytoarchitectural parameters using a new theoretical model for diffusion,” in *Proc. Intl. Soc. Mag. Reson. Med*, vol. 15, p. 1540, 2007. (Cited on page 22.)
97. S. N. Jespersen, C. R. Bjarkam, J. R. Nyengaard, M. M. Chakravarty, B. Hansen, T. Vosegaard, L. Astergaard, D. Yablonskiy, N. C. Nielsen, and P. Vestergaard-Poulsen, “Neurite density from magnetic resonance diffusion measurements at ultrahigh field: Comparison with light microscopy and electron microscopy,” *NeuroImage*, vol. 49, pp. 205–216, Jan. 2010. (Cited on pages 22 and 24.)
98. S. Jespersen, L. Leigland, A. Cornea, and C. Kroenke, “Determination of axonal and dendritic orientation distributions within the developing cerebral cortex by diffusion tensor imaging,” *Medical Imaging, IEEE Transactions on*, vol. 31, no. 1, pp. 16–32, 2012. (Cited on page 22.)
99. D. A. Yablonskiy and A. L. Sukstanskii, “Theoretical models of the diffusion weighted mr signal,” *NMR Biomed.*, vol. 23, no. 7, pp. 661–681, 2010. (Cited on page 22.)
100. D. Hasselman and L. F. Johnson, “Effective thermal conductivity of composites with interfacial thermal barrier resistance,” *Journal of Composite Materials*, vol. 21, pp. 508–515, June 1987. (Cited on page 22.)
101. S. Torquato and M. D. Rintoul, “Effect of the interface on the properties of composite media,” *Phys. Rev. Lett.*, vol. 75, pp. 4067–, Nov. 1995. (Cited on page 22.)
102. H. Cheng and S. Torquato, “Effective conductivity of periodic arrays of spheres with interfacial resistance,” *Proceedings: Mathematical, Physical and Engineering Sciences*, vol. 453, pp. 145–161, Jan. 1997. (Cited on page 22.)
103. Y. Assaf, T. Blumenfeld-Katzir, Y. Yovel, and P. J. Basser, “Axcaliber: A method for measuring axon diameter distribution from diffusion mri,” *Magn. Reson. Med.*, vol. 59, no. 6, pp. 1347–1354, 2008. (Cited on pages 23 and 24.)
104. M. Nilsson, E. Alerstam, R. Wirestam, S. Brockstedt, J. Lätt, *et al.*, “Evaluating the accuracy and precision of a two-compartment karger model using monte carlo simulations,” *Journal of Magnetic Resonance*, vol. 206, no. 1, pp. 59–67, 2010. (Cited on page 23.)

-
105. A. Waldeck, P. W. Kuchel, A. J. Lennon, and B. E. Chapman, “Nmr diffusion measurements to characterise membrane transport and solute binding,” *Progress in Nuclear Magnetic Resonance Spectroscopy*, vol. 30, pp. 39–68, Mar. 1997. (Cited on page 23.)
 106. G. J. Stanisiz, G. A. Wright, R. M. Henkelman, and A. Szafer, “An analytical model of restricted diffusion in bovine optic nerve,” *Magn. Reson. Med.*, vol. 37, no. 1, pp. 103–111, 1997.
 107. J. Pfeuffer, U. Flogel, W. Dreher, and D. Leibfritz, “Restricted diffusion and exchange of intracellular water: theoretical modelling and diffusion time dependence of ^1H NMR measurements on perfused glial cells,” *NMR in Biomedicine*, vol. 11, no. 1, pp. 19–31, 1998.
 108. J.-H. Lee and C. S. Springer, “Effects of equilibrium exchange on diffusion-weighted nmr signals: The diffusigraphic shutter-speed?,” *Magn. Reson. Med.*, vol. 49, no. 3, pp. 450–458, 2003.
 109. J. D. Quirk, G. L. Bretthorst, T. Q. Duong, A. Z. Snyder, C. S. Springer, J. J. Ackerman, and J. J. Neil, “Equilibrium water exchange between the intra- and extracellular spaces of mammalian brain,” *Magn. Reson. Med.*, vol. 50, no. 3, pp. 493–499, 2003.
 110. Y. Roth, A. Ocherashvili, D. Daniels, J. Ruizcabello, S. Maier, A. Orenstein, and Y. Mardor, “Quantification of water compartmentation in cell suspensions by diffusion-weighted and t_2 -weighted mri,” *Magnetic Resonance Imaging*, vol. 26, pp. 88–102, Jan. 2008.
 111. I. Aslund, A. Nowacka, M. Nilsson, and D. Topgaard, “Filter-exchange pgse nmr determination of cell membrane permeability,” *Journal of Magnetic Resonance*, vol. 200, no. 2, pp. 291 – 295, 2009.
 112. M. Nilsson, J. Lätt, E. Nordh, R. Wirestam, F. Ståhlberg, and S. Brockstedt, “On the effects of a varied diffusion time in vivo: is the diffusion in white matter restricted?,” *Magnetic resonance imaging*, vol. 27, no. 2, pp. 176–187, 2009. (Cited on page 23.)
 113. J. Coatléven, H. Haddar, and J.-R. Li, “A new macroscopic model including membrane exchange for diffusion mri.” Accepted. See <http://www.cmap.polytechnique.fr/~jingrebecali/preprints.html>, 2014. (Cited on pages 23, 24, 28, 29, 32 and 51.)
 114. A. Bensoussan, J.-L. Lions, and G. Papanicolaou, *Asymptotic analysis for periodic structures*, vol. 5 of *Studies in Mathematics and its Applications*. Amsterdam: North-Holland Publishing Co., 1978. (Cited on page 23.)
 115. T. Arbogast, “Gravitational forces in dual-porosity systems: Ii. computational validation of the homogenized model,” *Transport in Porous Media*, vol. 13, no. 2, pp. 205–220, 1993. (Cited on page 29.)

Bibliography

116. T. Arbogast, “Gravitational forces in dual-porosity systems: I. model derivation by homogenization,” *Transport in Porous Media*, vol. 13, no. 2, pp. 179–203, 1993. (Cited on page 29.)